SCALE-RESOLVING SIMULATION OF THE FLOW IN NEXT GENERATION NUCLEAR POWER PLANT HELICAL COIL STEAM GENERATOR

A Dissertation

by

MUSTAFA ALPER YILDIZ

Submitted to the Office of Graduate and Professional Studies of
Texas A&M University
in partial fulfillment of the requirements for the degree of

DOCTOR OF PHILOSOPHY

Chair of Committee,	Yassin A. Hassan
Committee Members,	William H. Marlow
	Victor Ugaz
	Rodolfo Vaghetto
	Elia Merzari
Head of Department,	Michael Nastasi

December 2020

Major Subject: Nuclear Engineering

“If one day, my words are against science, choose science”

Mustafa Kemal Atatürk

ABSTRACT

The helical coil steam generator (HCSG) is a specific type of shell-and-tube heat exchanger known for having a higher heat transfer coefficient than similar straight tube designs. Because of its compactness and higher heat transfer coefficient than many other designs, they are considered in a small modular reactor (SMR) and high-temperature reactor designs. Another advantage of HCSGs is that the helical coil bundle design has a high resistance to flow-induced vibrations (FIV), which is the important driver of tube ruptures. Investigation of flow behavior in HCSGs is essential for a safe nuclear reactor design.

The present study focuses on the analysis of the flow in the shell side of a 24-degree cut helical coil steam generator (HCSG) with large eddy simulation (LES). In the study, the open-source, high-order spectral element CFD code Nek5000 was employed for numerical simulation. LES was performed at a Reynolds number of 9000 based on the inlet velocity and tube diameter. Spectral analysis was carried out along the tube bundle to investigate the vortex shedding and to reveal shedding frequencies in HCSGs. Wavelet analysis was carried out to determine the time-frequency information of the fluctuating velocities in the domain. The flow was decomposed into modes with proper orthogonal decomposition, which revealed the most energetic coherent structures in the flow and evolution of the modes in time. Multi-resolution dynamic mode decomposition (mrDMD) was employed for the wavelet-inspired analysis of the coherent structures in the domain.

For the validation of Nek5000 in complex geometries, results from the numerical simulation were compared with experiments conducted at Texas A&M University.

DEDICATION

To Burcu

ACKNOWLEDGEMENTS

Above all, I would like to thank my wife Burcu for her support and great patience at all times. It wouldn't have been possible to finish this doctoral thesis without her help.

I would like to express my deep and sincere gratitude to my advisor, Dr. Yassin Hassan, for his support and invaluable guidance throughout this research. It was a privilege to work and study under his guidance. I would also like to thank him for his friendship, for which I am extremely grateful. I would like to thank my committee member Dr. Elia Merzari. I am grateful for his support, guidance, and friendship throughout the course of this research. Thanks to my committee members Dr. William H. Marlow, Dr. Rodolfo Vaghetto, and Dr. Victor Ugaz for their guidance and suggestions.

Thanks also go to my friends, colleagues, and the department faculty for making my time at Texas A&M University a great experience.

Finally, thanks to my parents and sibling for their support in my education and career goals throughout my life.

CONTRIBUTORS AND FUNDING SOURCES

Contributors

This work was supervised by a dissertation committee consisting of Professor Yassin A. Hassan (advisor), Professor William H. Marlow and Dr. Rodolfo Vaghetto of the Department of Nuclear Engineering, Professor Victor Ugaz of the Department of Chemical Engineering and Dr. Elia Merzari of Argonne National Laboratory.

Experimental data was supplied by Texas A&M University Thermal Hydraulics Research Laboratory.

All other work conducted for the dissertation was completed by the student independently.

Funding Sources

Graduate study was supported by a research assistantship from Professor Yassin A. Hassan, Department of Nuclear Engineering Texas A&M University. Partial financial support was provided by the Turkish Ministry of National Education.

NOMENCLATURE

CAD	Computer Aided Design
CFD	Computational Fluid Dynamics
CU	Convective Units
DMD	Dynamic Mode Decomposition
DNS	Direct Numerical Simulation
FFT	Fast Fourier Transform
FIV	Flow Induced Vibration
GLL	Gauss-Lobatto-Legendre
HCSG	Helical Coil Steam Generator
LES	Large Eddy Simulation
MBP	Moving Boundary Projection
mrDMD	multi-resolution Dynamic Mode Decomposition
NSSS	Nuclear Steam Supply System
PIV	Particle Image Velocimetry
POD	Proper Orthogonal Decomposition
PSD	Power Spectrum Density
PWR	Pressurized Water Reactor
RANS	Reynolds Averaged Navier-Stokes
SEM	Spectral Element Method
SFI	Secondary Flow Intensity

SG	Steam Generator
SVD	Singular Value Decomposition
TKE	Turbulent Kinetic Energy

TABLE OF CONTENTS

Page

LIST OF FIGURES

Page

LIST OF TABLES

Page

1. INTRODUCTION

1.1. Background

Heat exchangers are devices that are used to transfer thermal energy between fluids at different temperatures. They are used in a wide variety of engineering applications such as power production, chemical and food industries, air conditioning and refrigeration. In nuclear reactors, the coolant in the primary side flows through the reactor and takes the heat from the core. Then flows through the steam generator, where the heat transfer between primary and secondary side occurs. In this process, a steam generator (SG) functions as a heat sink in a nuclear steam supply system (NSSS) and produces high-quality steam.

1.1.1. Steam generators

Steam generators are nuclear power plant components where the steam is produced for driving the turbines to produce electricity. They are eventually heat exchangers where the heat produced in reactor core is transferred to the secondary side of the nuclear power plant. Heat exchangers are devices that are used to transfer thermal energy between fluids at different temperatures. They are used in a wide variety of engineering applications such as power production, chemical and food industries, air conditioning and refrigeration. Heat exchangers may be classified according to the following main criteria [1]:

- Recuperators/regenerators
- Transfer process
- Geometry of construction

- Heat transfer mechanism
- Flow arrangements

According to transfer process, heat exchangers are classified as direct contact type and indirect contact type. In direct contact type heat exchangers, heat from the hot fluid is transferred to the cold fluid by direct contact of the fluids. In indirect contact type heat exchangers, there is a surface (separating wall) through which the heat is transferred from hot fluid to cold fluid. Helical coil steam generator can be classified as indirect contact type heat exchanger, since the helical tubes separate the hot fluid from the cold fluid and the heat is transferred through the helical tubes.

According to geometry of construction, heat exchangers are classified as [1]:

- Tubular heat exchangers
- Plate heat exchangers
- Extended surface heat exchangers

Tubular heat exchangers are built of circular tubes where one fluid flows inside the tubes and the other flows on the outside of the tubes. Plate heat exchangers are built of thin plates where the fluid streams are separated by flat plates. Extended surface heat exchangers are devices with fins on the heat transfer surface to increase the heat transfer surface. Extended surface heat exchangers are widely used in gas-to-gas and gas-to-liquid heat exchangers. According to geometry of construction HCSGs can be classified as tubular heat exchangers.

According to heat transfer mechanism, heat exchangers can be classified as [1]:

- Single-phase convection on both sides

- Single-phase convection on one side, two-phase convection other
- Two-phase convection on both sides

In thermal power plants and pressurized water reactors (PWR) has phase change on one of the sides in heat exchangers. Helical coil steam generators can be classified as single-phase convection on one side and two-phase convection on other. In HCSGs phase change occurs inside the tubes where the steam is produced. Outside of the tubes (shell side) fluid is cooled down without phase change.

According to the flow arrangements, heat exchangers are classified as [1]:

- Parallel-flow
- Counter-flow
- Cross-flow

In parallel-flow heat exchangers, the two fluid streams enter together at one end, flow through in the same direction, and leave together at the other end. In counter-flow heat exchangers, two-fluid streams flow in opposite directions. In a cross-flow heat exchanger, one fluid flows through the heat transfer surface at right angles to the flow path of the other fluid. HCSGs can be considered as cross-flow heat exchangers.

Figure 1.1 shows the heat exchanger classification chart for helical coil steam generators.

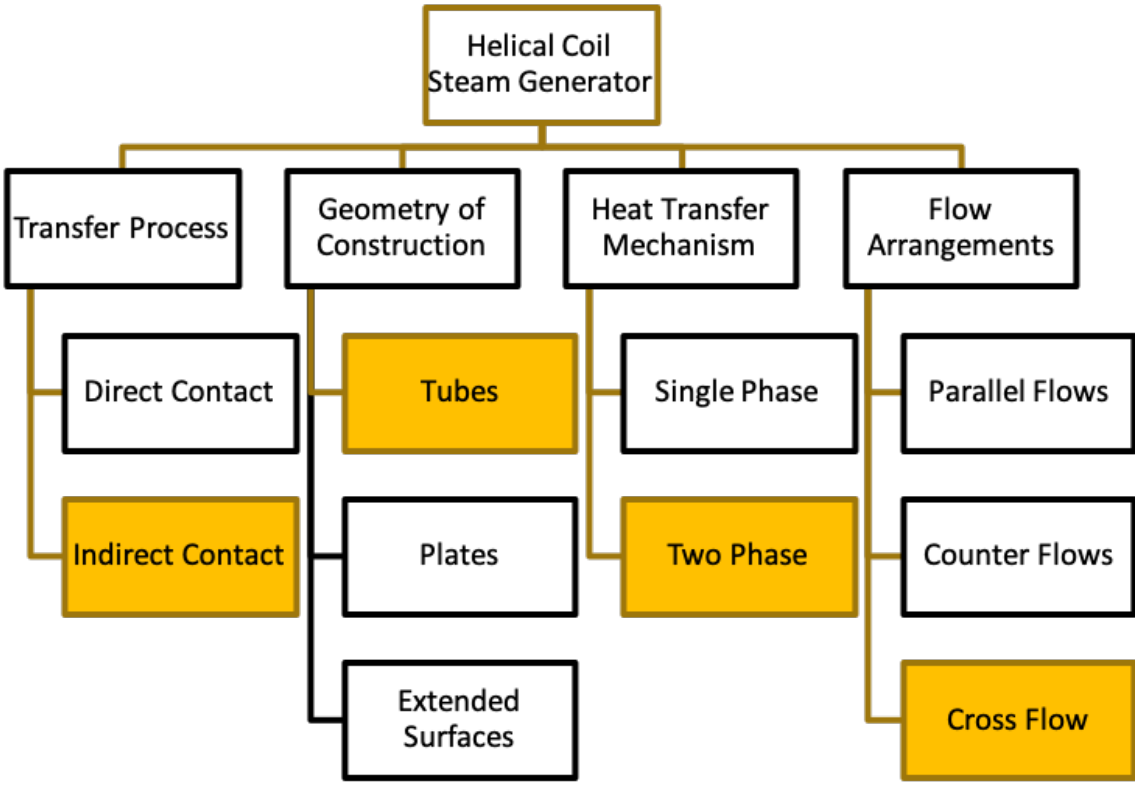

Figure 1 Helical coil steam generator classification chart

1.2. Literature Review

Flow in tube bundles has been the subject of many studies [2]. The main reason behind the interest has been the use of tube bundles in cross-flow heat exchangers, which are used to transfer thermal energy between fluids at different temperatures. Heat exchangers are employed in a wide variety of engineering applications such as power production, chemical and food industries, air conditioning, and refrigeration.

Helical coil steam generator (HCSG) is a specific type of shell-and-tube heat exchangers. The advantage of HCSGs over other types of steam generators is that they

can be used to pack a big surface area in a small volume. Previous studies have demonstrated that HCSGs can increase the heat transfer coefficient compared with similarly dimensioned straight tube heat exchangers [3]. Helically banked steam generators have a number of obvious advantages in terms of cost effectiveness. They do not require sharp tube bends, which increase the pressure loss on the steam/water side of the tubes and may also impose potential manufacturing problems [4]. They have been considered in the design of small modular reactors, sodium fast-cooled reactors, and high-temperature reactors for their compactness and high heat transfer coefficient [5–7].

One of the major concerns in the design of heat exchangers is flow-induced vibrations (FIV). An extensive review of the state of knowledge of FIV was given by previous researchers [2,8,9]. Weaver and Fitzpatrick, in their review [2], identified the excitation mechanisms of FIV and classified them in four categories: turbulent buffeting, Strouhal periodicity (also known as vortex shedding), fluid-elastic instability, and acoustic resonance.

In early experimental studies considerable efforts focused on the investigation of FIV in tube bundles. Polak and Weaver [10] conducted experiments to study vortex shedding in normal triangular tube arrays over a pitch-to-diameter ratio of 1.14-2.67 and a Reynolds number of 7600-49000. They reported Strouhal numbers for the range of pitch ratios and showed that Strouhal numbers depend on pitch ratio, Reynolds number, and locations in the bundle. Konstantinidis et.al. [11] conducted experiments to study vortex shedding in a staggered tube array with streamwise and transverse pitch-to-diameter ratios of 2.1 and 3.6, respectively. In their study, they showed that vortex shedding occurs in two

distinct frequencies at the front and inner rows and that shedding occurs at smaller frequency closer to the end of tube bundle. Recently an experimental study was conducted to visualize the flow in a simplified HCSG model different from the straight tube bundles [12]. In this study, the test section was a single channel between helically wound tubes, with a varying lateral pitch ratio and constant transverse pitch ratio of 2.98.

Improvements in computational power made computational fluid dynamics (CFD) more attractive for researchers. Li et al. [13] simulated a two-dimensional in-line tube array with an unsteady Reynolds-averaged Navier-Stokes (URANS) formulation, where they showed wall effects on the flow behavior and extensive mixing in the middle of the tube bundle. Wang et al. [14] numerically investigated the thermodynamic performance for inclined tubes using a steady-state Reynolds-averaged Navier-Stokes (RANS) formulation. Their study indicated that the inclination degree of the tubes does not have much effect on the characteristics of flow and heat transfer for fluid flowing across tube banks. Joh [15] used a RANS formulation to study the cross-flow in HCSGs; his results showed a larger pressure drop than predicted by current correlations. Cross-flow over tube bundles was also studied with high-fidelity simulations. Hassan and Barsamian [16] conducted numerical analysis of the flow through staggered tube bundle with large eddy simulation (LES), where results showed good agreement with experimental data. Liang and Papadakis [17] studied vortex shedding characteristics inside a staggered tube array with LES; their reported Strouhal numbers agree with experimental measurements. Yuan et al. [18] studied FIV in HCSGs by coupling a CFD code with a structural analysis code. In their study, they generated transient pressure data from the LES, which they used in the

structural analysis code for response analysis of structural vibrations. Lai et al. [19] conducted LES for a simplified HCSG test section using Nek5000; the results were in good agreement with particle image velocimetry (PIV) data.

These numerical studies show that the RANS formulation for turbulence modeling does not provide accurate results for simulating cross-flow in tube bundles; in contrast, higher-fidelity simulations show better results.

Most of the cited studies on flow over tube bundles consider cases with constant pitch-to-diameter ratios. The aim of this study is to provide a better understanding of the flow behavior in novel steam generator designs. Comparisons of the first- and second-order statistics with experimental data were presented in [20]. In the present study, we analyzed flow in the shell side of HCSGs with oppositely coiled adjacent tubes. To the best of our knowledge, no studies have been conducted on HCSGs with oppositely slanted adjacent coils at this scale. Results of our numerical analysis from the LES calculations are compared with available experimental data for validation purposes.

1.3. Objectives of the Study

The objectives of the study is to model turbulent flow in the shell side of a helical coil steam generator with a large eddy simulation (LES) approach using the spectral element method, which will provide a database of high fidelity statistically time-invariant data to be used for low fidelity approaches. The study aims to capture and quantify complex flow phenomena and turbulence characteristics that are present in helical coil steam generators. Specifically, objectives of the study can be listed as follows:

- Development of the hexahedral meshing strategy for complex geometries and application in helical coil steam generator.
- Generating a high-fidelity database of time-invariant flow data for the first- and second-order turbulence statistics.
- Quantification of the flow excitation mechanisms due to vortex shedding in a helical coil steam generator.
- Quantification of the turbulence characteristics in helical coil steam generator geometry.
- Investigation and quantification of flow dynamics in helical coil steam generators.
- Validation of the simulation results with the experimental data.

1.4. Structure of the dissertation

The structure of the dissertation can be summarized section-wise below:

1. Section 1: Introduction, including background in steam generators, literature review and objectives of the study.
2. Section 2: Theory. Brief discussion of the mathematical theory that is relevant to all the subsequent sections.
3. Section 3: Methodology.
4. Section 4: Results.
5. Section 5: Conclusion.

2. THEORY

2.1. Navier-Stokes equations

The first partial differential equation for fluid dynamics was formulated Euler in 1752 when he considered only for inviscid fluids. After adopting the Newton's definition of friction due to the velocity gradient and fluid viscosity, Navier and Stokes could independently include the viscous forces into the equation.

The Navier-Stokes equations are the fundamental equations for governing fluid motion and dynamics. The derivation of the Navier-Stokes equations is presented in many well-known textbooks. Following the derivation in [21], the constant property, incompressible, dimensional Navier-Stokes equations are as follows:

$$\frac{\partial U}{\partial t} + \nabla \cdot (\rho U) = 0 \tag{1}$$

$$\rho\left(\frac{\partial U}{\partial t} + U \cdot \nabla U\right) = -\nabla P + \nabla \cdot \tau + \rho f \tag{2}$$

where

$$\tau = \mu(\nabla U + \nabla U^T). \tag{3}$$

In constant property flows, the continuity equation 2 reduces to divergence free condition

$$\nabla \cdot U = 0. \tag{4}$$

If the fluid density is constant in the entire domain, the viscous stress tensor Eq. 3 can be contracted and have the form

$$\nabla \cdot \tau = \mu \Delta U. \tag{5}$$

2.1.1. Non-dimensional Navier-Stokes Equation

The dimensional Navier-Stokes equations can be non-dimensionalized with appropriate characteristic parameters. The non-dimensional parameters are as follows

$$x^* = \frac{x}{L_c}, u^* = \frac{U}{U_c}, t^* = \frac{t}{L_c / U_c} \tag{6}$$

where L_c is the characteristic length and U_c is the characteristic velocity. Pressure can be non-dimensionalized based on the physics of the flow. In high velocity flows, where the convective effects are dominant, pressure can be non-dimensionalized as follows

$$p^* = \frac{P}{\rho U_c^2}. \tag{7}$$

Using the non-dimensionalization method given in equations 6 and 7, the Navier-Stokes equation can be non-dimensionalized in the following form

$$\nabla \cdot u^* = 0 \tag{8}$$

$$\frac{\partial u^*}{\partial t^*} + u^* \cdot \nabla u^* = -\nabla p^* + \frac{1}{Re}\nabla \cdot \tau^* + \frac{1}{Fr}\frac{f}{g} \tag{9}$$

where

$$\tau^* = (\nabla u^* + \nabla u^{*T}) \tag{10}$$

2.2. Computational Fluid Dynamics

Computational fluid dynamics (CFD) is the analysis of systems involving fluid flow, heat transfer and associated phenomena such as chemical reactions by means of computer-based simulation [22]. Today, use of CFD spans in wide range of industrial and nonindustrial application areas, such as aerospace, turbomachinery, biomedical engineering, meteorology, and power plants.

There are several unique advantages of CFD over experiment-based approaches to fluid system design:

- Relative costs of CFD codes with respect to experimental setup.
- Reduction of lead times and costs of new designs.
- Ability to study systems where controlled experiments are difficult or impossible to perform.
- Very high level of detail of results.

2.3. Turbulence

Theoretical analysis and prediction of turbulence has been, and still is the fundamental problem of fluid dynamics. The major difficulty arises from the random and chaotic nature of turbulence phenomena. Turbulence is the manifestation of the spatio-temporal behavior of fluid flows at large values of a parameter, for instance Reynolds number. It entails the dynamics of a strongly nonlinear dissipative system with an extremely large number of degrees of freedom, whose evolution is governed by the Navier-Stokes equations.

2.3.1. Nature of Turbulence

In spite of over a century of research, the phenomenon of turbulence has been described as the "final unsolved problem in classical physics". The attributes that make turbulence such a formidable challenge can be enunciated as three features, which are non-locality, nonlinearity, and non-integrability [21].

2.3.1.1. Non-locality

Turbulent processes are non-local in space and time. Turbulence has a long memory, and its behavior at a point can be strongly influenced by the flow remote from that point. The non-local nature of turbulence arises due to the pressure gradient term in the Navier-Stokes equations. The pressure experienced by a fluid particle is due to the collective effect of all the other fluid particles in the entire domain. Such an interaction

between points that may be separated by arbitrary distances leads to the long-range forces due to pressure.

In the Navier-Stokes equations, the non-locality arises due to the pressure term, as the evolution of pressure is governed by a Poisson equation:

$$\nabla^2 p = -\rho \frac{\partial U_i}{\partial x_j} \frac{\partial U_j}{\partial x_i} \tag{11}$$

Laplacian is an elliptic operator; thus, this equation has no real characteristic directions. The solution of this equation at any point $\overrightarrow{x_o}$ is given by

$$p(\overrightarrow{x_o}) = -\frac{\rho}{4\pi} \iiint_V \frac{\partial U_i}{\partial x_j} \frac{\partial U_j}{\partial x_i} \frac{1}{|\vec{x} - \overrightarrow{x_o}|} d\vec{x} \tag{12}$$

From this solution, it is evident that the pressure at any arbitrary single point is defined by the velocity gradients at all the other points in the entire flow field. This makes the Navier-Stokes equations essentially integro-differential and leads to the non-local nature of turbulence.

2.3.1.2. Non-linearity

The non-linear nature of turbulence arises due to the convective derivative term in the Navier-Stokes equations. In physical terms, non-linearity allows a system to have a self-feedback mechanism. Any small change in the system's conditions causes a direct corresponding change in the system's behavior. However, due to non-linearity, this change in itself can lead to an- other shift in the dynamics of the system. This feedback process continues, ad infinitum, leading to complex behavior.

2.3.1.3. Non-integrability

Integrable systems have many features that are desirable from the point of view of their analysis. These include the presence of many conserved quantities, the existence of an algebraic geometry and the transformation into a Lax pair form, besides others. As a mathematical property, Integrability is separate from non-linearity and non-locality. There are many complicated systems like the Riccati equation, the Boussinesq equations, the Burger's equations, in addition to the Schrodinger equation and the KdV equations that have seemingly complicated structure but are completely integrable. On the other hand, there are seemingly simple systems that are completely non- integrable, such as the classical Three-body problem. The final problematic feature of turbulence is that the Navier-Stokes equations are non-integrable.

These three characteristics of the turbulence phenomenon are inherent to its nature and act as a demarcation from similar phenomena observed in chaotic systems or stochastic systems.

3. METHODOLOGY*

3.1. Flow Configuration

The present study was validated with time-resolved PIV measurements in 5-rod HCSG geometry. The test facility is a 24-degree section of a full rotation. Figure 2 shows the full five-layer helical coils and the section that is used to create the test section.

The shell-and-tube heat exchangers are defined as inline or staggered based on the locations of the adjacent tube centers relative to each other. Consequently, the streamwise and transverse pitch-to-diameter ratios of the defined heat exchangers are different and are defined respectively as follows:

$$a = \frac{S_L}{d_R}$$

$$b = \frac{S_T}{d_R}$$

where S_L is the streamwise pitch, S_T is the transverse pitch, and d_R is the rod diameter. Figure 3 shows the two tube configurations.

* Part of this chapter is reprinted with permission from "Spectral element applications in complex nuclear reactor geometries: Tet-to-hex meshing" by Haomin Yuan, Mustafa Alper Yildiz et al., 2020, Nuclear Engineering and Design, 357, 110422. Copyright by Elsevier B.V.

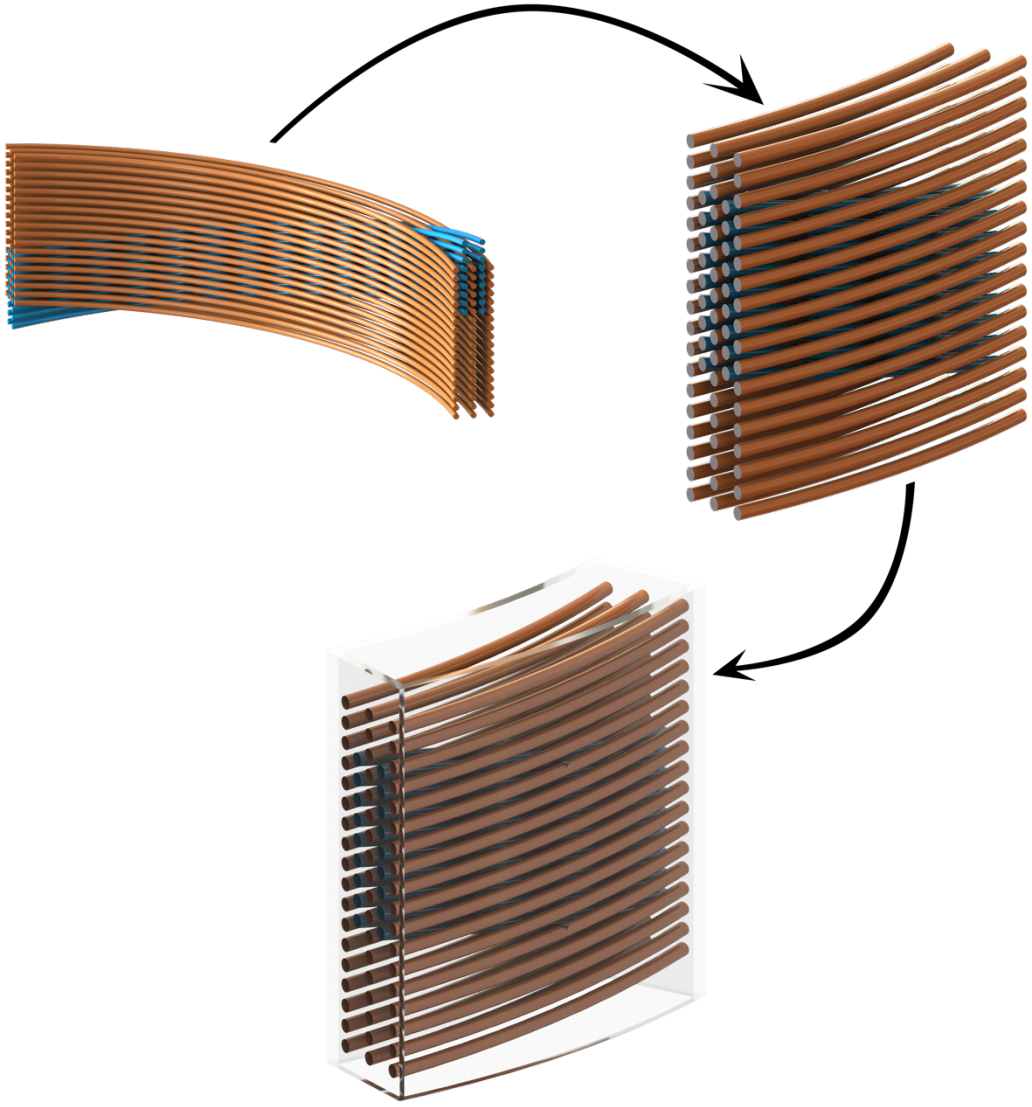

Figure 2: Experimental Facility (reprinted) [23]

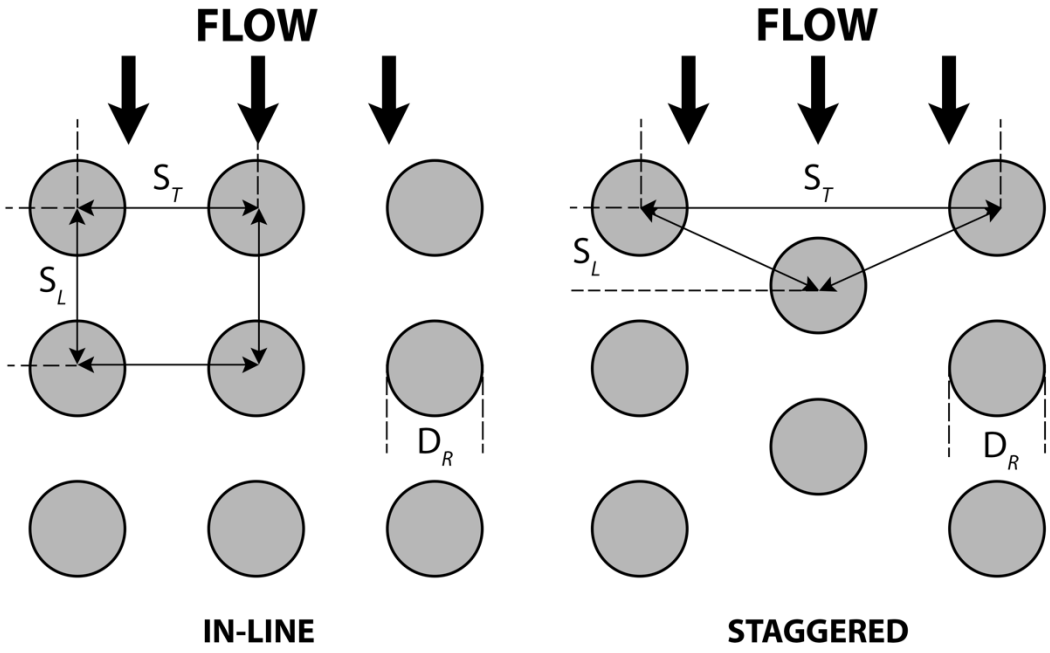

Figure 3: Tube configurations in shell-and-tube heat exchangers

Most commonly, the research conducted on shell-and-tube heat exchangers (specifically HCSGs) a single helical pitch have constant pitch-to-diameter ratios, making it easy to identify the arrangement of the tubes if they are inline or staggered. However, the examined HCSG geometry has neither an inline nor a staggered tube arrangement since adjacent tube bundles have different helical pitch and are slanted in opposite directions, causing the streamwise pitch-to-diameter ratio to change in the azimuthal direction. The two outer coils and central coil have 18 rods each with a helix pitch of 0.427 m. The two inner coils have 9 rods each with helix pitch of 1 m.

The aim of the experimental study is to investigate the flow outside the rods, on the shell side of the steam generator; therefore, the helical coils are made of solid rods.

The diameter of the rod in the test facility is 15.875 mm. The helix diameter of the central rod is 1.905 m. The transverse pitch-to-diameter ratio is 2.96.

The test section of the HCSG was built from acrylic. It was connected to a once-through closed loop. The facility incorporated a centrifugal pump connected to a tank. Working fluid is pumped vertically to the T-junction where the flow is divided before coming to the upper plenum. In the upper plenum the flow is mixed and conditioned with honeycombs and screens. P-cymene was utilized as a working fluid in the test section. Tests were conducted in isothermal conditions at room temperature (21±1°C) at which p-cymene and acrylic have similar refraction indices. For more details of the experimental facility and experimental procedure, readers are referred to [24].

3.2. Computational Domain

In order to have a better representation of the experimental facility, it was scanned across seven vertical planes, and the CAD model of the test section was regenerated from the scanned planes. Center points of the tubes were extracted from each scanned plane, which were used to obtain centerline of each tube by curve fitting. The CAD model of the test section was regenerated by extruding cylinders around the centerlines. The flow domain, a 24-degree section of a full rotation, then was extracted from the CAD model; see Figure 4.

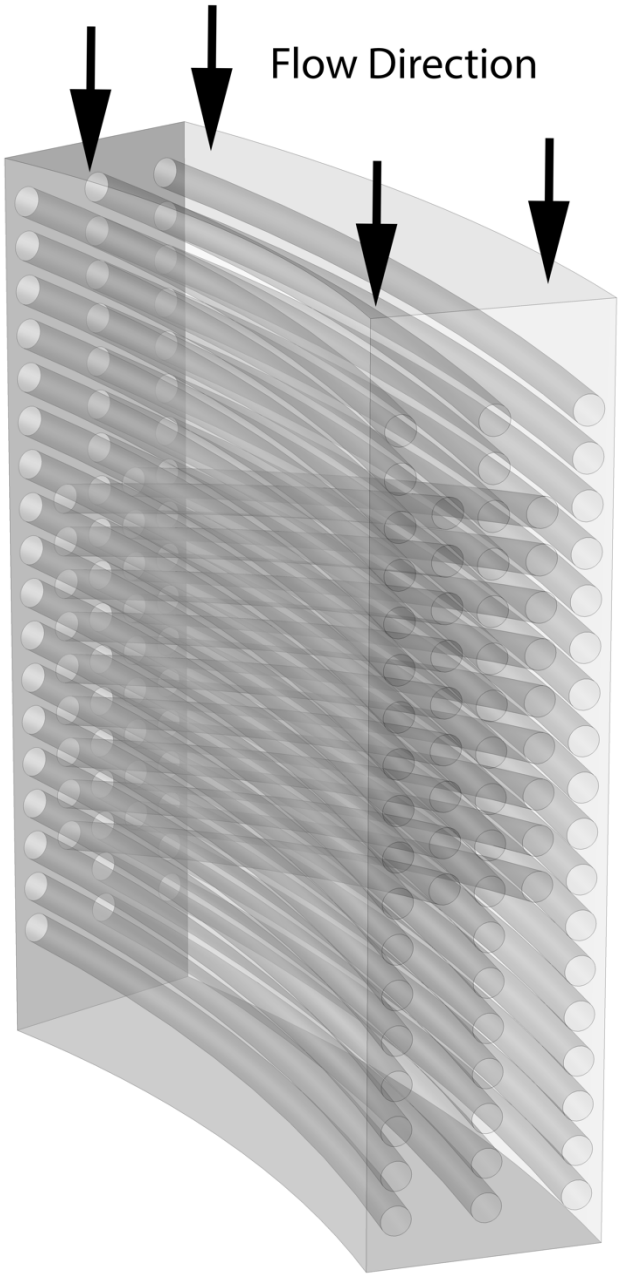

Figure 4: Flow domain (reprinted) [23]

3.3. Spectral Element Method CFD Code Nek5000

Nek5000 is an open source fluid/thermal simulation code based on the spectral element method (SEM), which is a high-order weighted residual technique that combines the geometric flexibility of finite elements with the rapid convergence and tensor-product efficiencies of global spectral elements [25].

In the present study, the constant property Navier-Stokes equations were solved in Nek5000. In addition to its higher-order foundation, Nek5000 has further advantages that make it suitable for large-scale simulations. To speed up the time to solution, it can use the method of characteristics to relax the Courant-Friedrichs-Lewy restriction or use orthogonal projections of the solution to reduce the iteration count of the algebraic solver [26].

In LES, large-scale turbulent structures are resolved while the smaller scales are modeled. The contribution of the smaller scales to the energy cascade in the present case is modeled through a local, element-based explicit cut-off filter in wave-number space. The energy is removed from the smallest scales (high wave numbers), thus mimicking the effect of smaller eddies. This allows for a coarser grid and therefore lower computational cost.

3.4. Meshing Strategy

Nek5000 supports only hexahedral elements and meshing therefore can be complicated and time consuming for complex geometries. For our study, creating a blocked hexahedral mesh with an acceptable number of elements presented two challenges. First, the rod bundles are not evenly spaced in transverse direction in the experimental facility, which prevents having specific pattern to follow in a blocked meshing strategy. Second, different helix pitches and oppositely slanted adjacent coils cause highly skewed elements in the region between the tubes.

We therefore employed a different meshing strategy to overcome these two problems for the present geometry. We call this strategy tet-to-hex meshing. The tet-to-hex meshing method can utilize the high flexibility of a pure tetrahedral mesh to conform to the geometry, but still maintain the higher-order accuracy of Nek5000. Moreover, in complex geometries, it can do so at a computational cost and accuracy comparable to the block-structured mesh when available.

A pure tetrahedral mesh can be generated automatically by using many available commercial or open-source meshing codes. In this research, ANSYS meshing was utilized to generate the pure tetrahedral mesh, and ANSYS ICEM or exo2nek (meshing conversion tool in Nek5000) to perform the tet-to-hex conversion. Fig. 5 shows how one tetrahedral element is converted to four hexahedral elements.

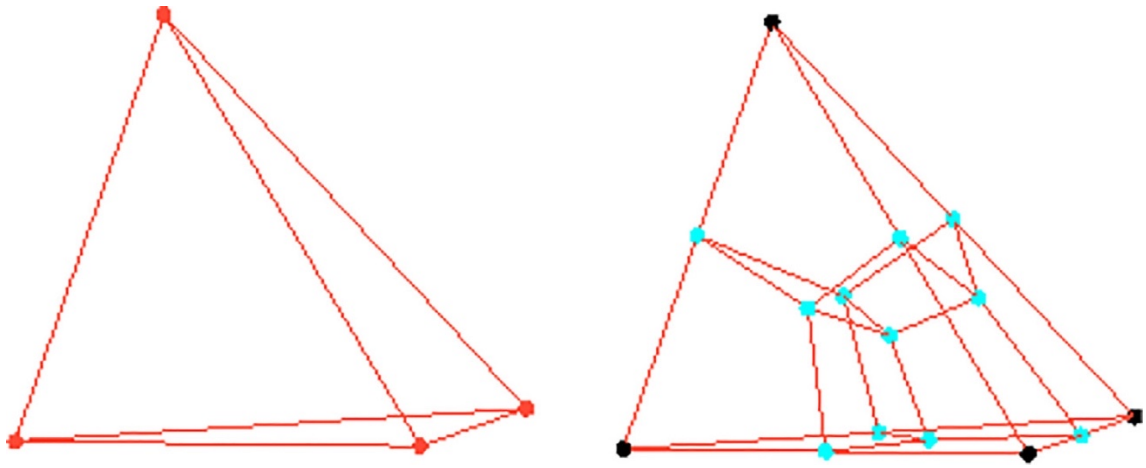

Figure 5: One tetrahedral element converted to four hexahedral elements

Boundary layer generation could be performed in several ways. The first option is to use the inflation feature in ANSYS meshing to generate boundary layers. Then elements in boundary layers are of wedge type. Wedge type elements combined with tetrahedral elements can all be converted into hexahedral elements in exo2nek conversion. The second option is to use the extrusion feature in ANSYS ICEM. In ANSYS ICEM, surface quad elements can be extruded in normal direction to form proper boundary layers. There are other options available, but that discussion is out of the scope of this paper.

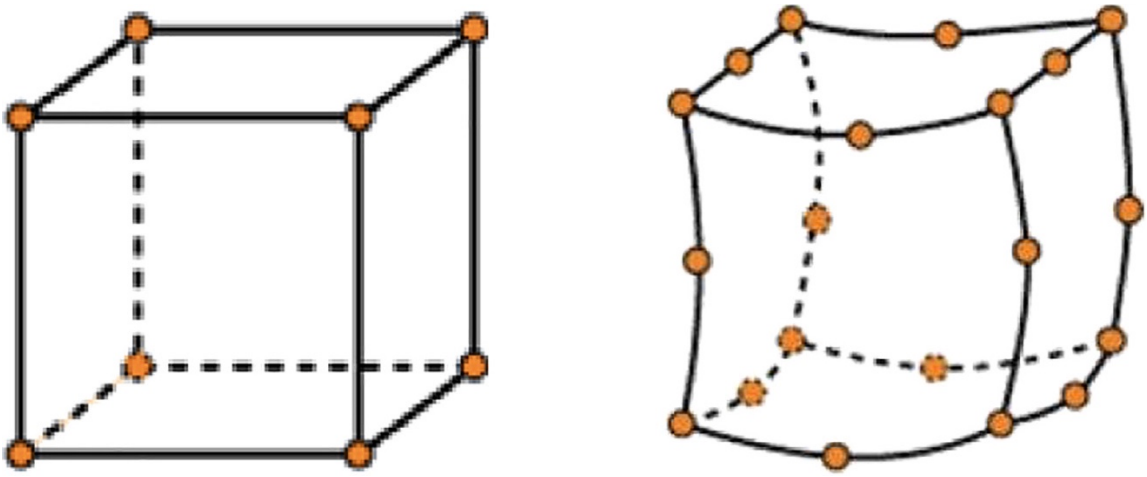

Figure 6: HEX-8 (left) and HEX-20 (right) elements

Nek5000 utilizes second-order elements to maintain a precise description of geometry with curvature. All hexahedral elements with 8 nodes description (hex8) can be converted to hexahedral elements with 20 nodes description (hex20) as shown in Fig. 2, which means mid-edge points are added later to describe curvature if there is any. Functions within each element are expanded as Nth-order polynomials cast in tensor-product form, which means there are (N+1)3 Gauss-Lobatto-Legendre (GLL) grid points distributed in each element [27]. Hence, in order to reduce the computational cost, a relatively coarse mesh, in terms of elements rather than grid points, must be developed. Specifically, second-order elements are needed in order to have a precise description of the geometry, which is hex20 for hexahedral elements. The converted hex20 elements then can be projected to fully describe the geometry curvature. The projection can be done in many ways, through ANSYS ICEM or through moving boundary projection (MBP) in Nek5000.

The MBP projection technique starts with a linear mesh without curvature, which does not fit the geometry surface. Next, for each GLL point on a moving boundary, it finds the projected points on the real geometry. A moving mesh velocity then is applied on this GLL point, and a Poisson solve is performed to determine the interior mesh velocity. The mesh is then deformed accordingly. The process is performed typically in several steps to avoid having the mesh become invalid (e.g., negative Jacobians to appear). The MBP technique in Nek5000 also brings significant benefits in meshing: we can greatly reduce the element number but still maintain a good geometry description and boundary layer strategy.

3.4.1. Example Case: Pipe Flow

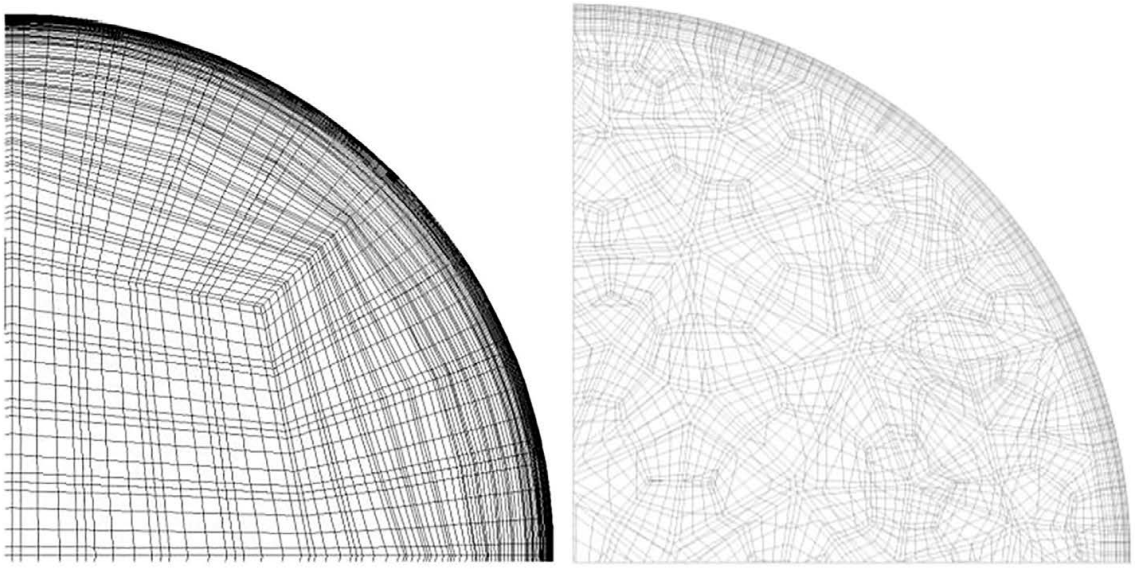

Figure 7: Pipe cross-section mesh from structural (left) and tet-to-hex mesh (right) (reprinted) [28]

Pipe flow is a canonical flow case for CFD. Here two sets of meshes, one a structural mesh and the other a tet-to-hex mesh is prepared; see Fig. 7. The length over diameter (L/D) is 5 for this pipe with a periodic inlet/outlet. Both meshes have approximately 60,000 elements; with N=5, the computational domain has around 13 million GLL points, with y^+ less than 1 when the bulk Reynolds number is 5310. The mesh resolution was judged sufficient to reach accuracy and it follows guidelines establish for wall-resolved LES with the spectral-element method. Fig. 8 shows the average stream-wise velocity in non- dimensional units, and Fig. 9 shows the rms velocity in all directions. Under this bulk Re, the viscous Re is 180 as shown Fig. 8. Results match between the two meshes and are consistent with DNS data obtained from reference [29].

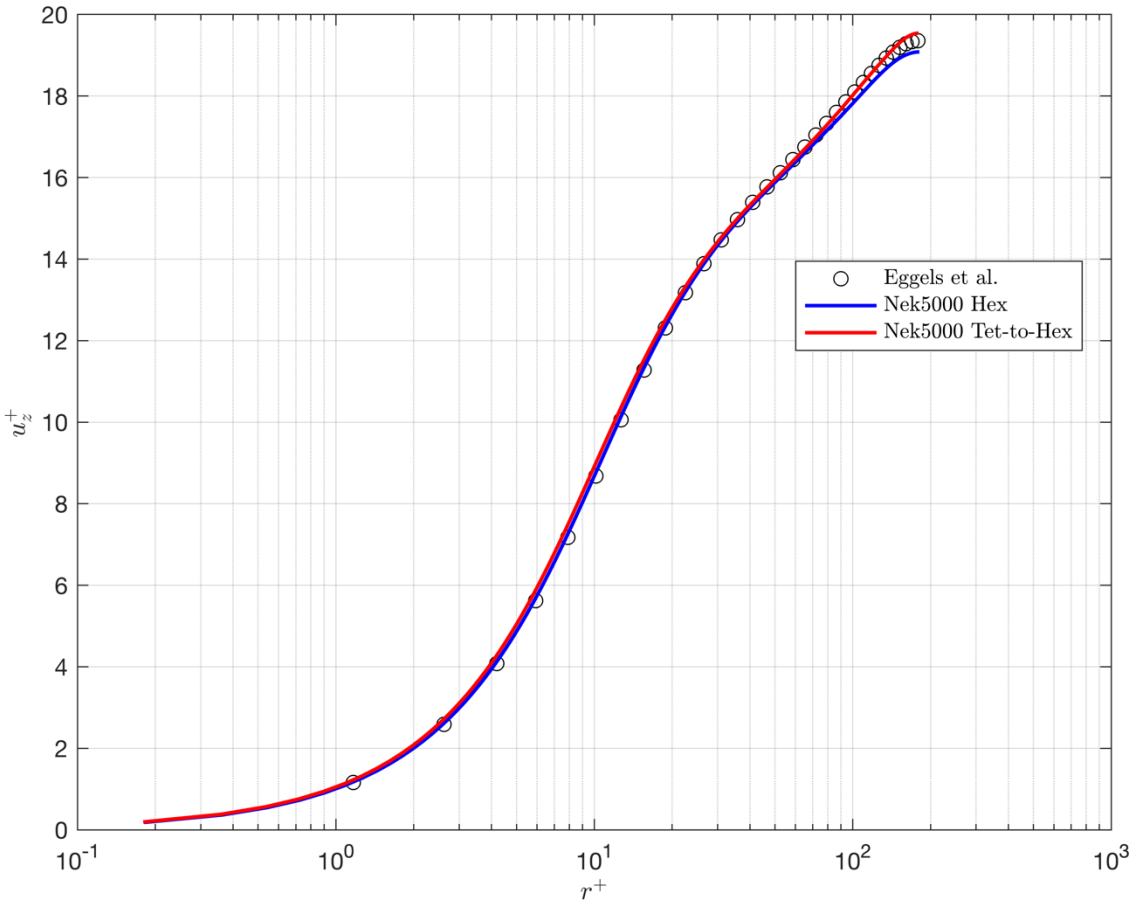

Figure 8: Average streamwise velocity (reprinted) [28]

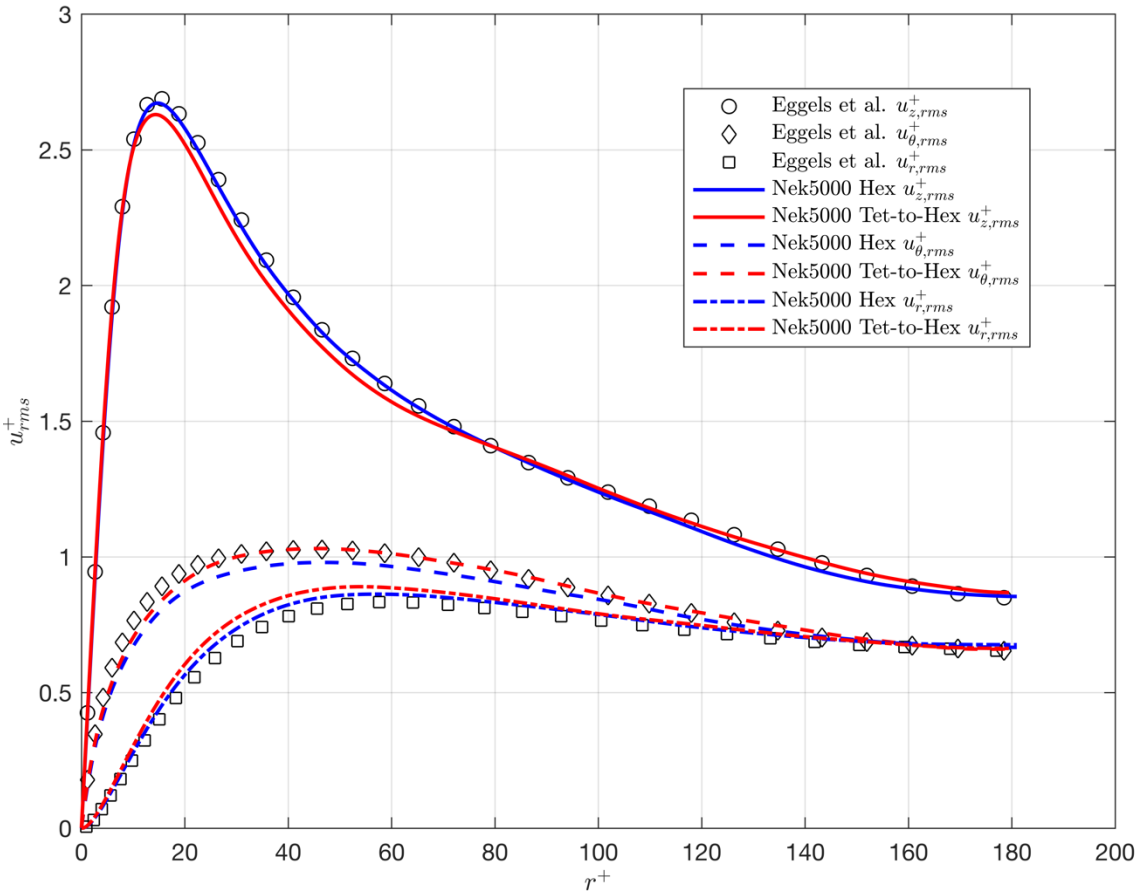

Figure 9: Average velocity rms values (reprinted) [28]

3.5. Helical coil steam generator mesh

In early studies, the blocking method was used for HCSG with tubes rotating in the same direction, as described in [18]. In this problem, however, different columns of tubes are rotating in opposite directions, as shown in Fig. 2. If we still use the blocking method, there will be transition layers with highly skewed elements, as noted in [30]. For some circumstances, this blocking method may work. For this case, however, we were unable to produce an adequate block-structured mesh. As a result, the tet-to-hex method becomes the essential approach for generating a high-quality mesh for this problem.

The moving boundary projection (MBP) technique in Nek5000 was used reduce the higher-element number and maintain a good boundary layer layout. Fig. 10 presents a zoomed-in view of the mesh around the tubes before and after projection at polynomial order N=2, as well as the moving mesh velocity distributed by the Nek5000 solver (Fisher et al., 2008). Using this technique, we could greatly reduce the elements needed for complex geometries, while maintaining a good geometry description.

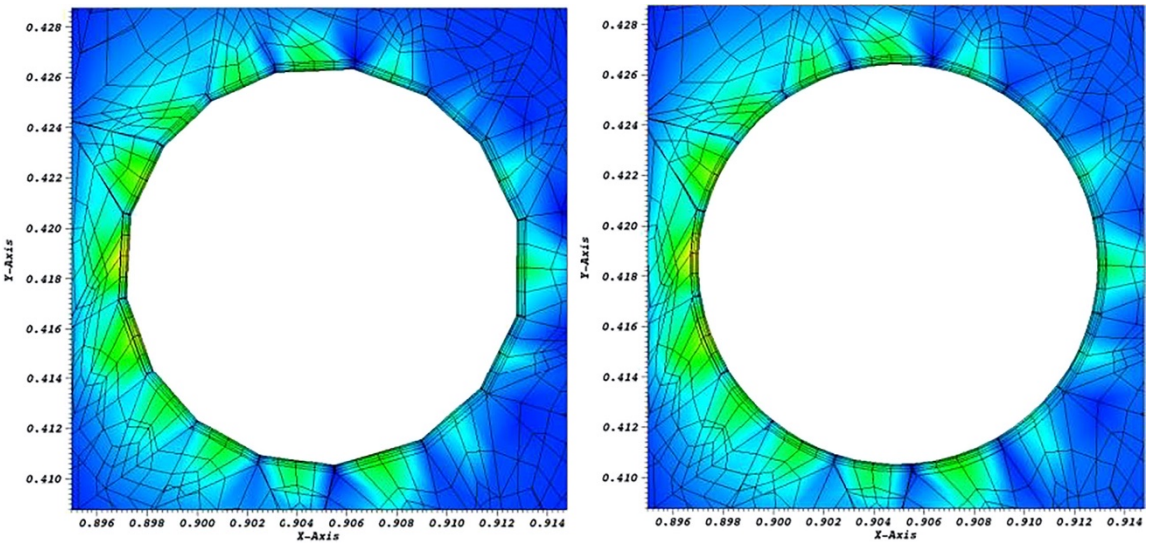

Figure 10: Zoomed-in view of mesh near tube before projection (left) and after projection (right) with distributed mesh velocity (reprinted) [28]

Fig. 11 shows the planar section of the final mesh around the tubes. Fig. 12 shows a zoomed-in view of the mesh, which involves approximately 4.1 million hexahedral elements. For an Nth polynomial expansion, each element in Nek5000 is represented by (N+1) grid points in each direction. Therefore, the number of grid points in the third, fifth,

seventh, and ninth polynomial orders is approximately 262×10^6, 885×10^6, 2100×10^6, and 4100×10^6 (4.1 billion grid points), respectively.

The boundary layer thickness for the mesh was extruded such that in the fifth polynomial expansion 65%, in the seventh polynomial expansion 90%, and in the ninth polynomial expansion 99% of near-wall grid points have a y^+ value below 1.

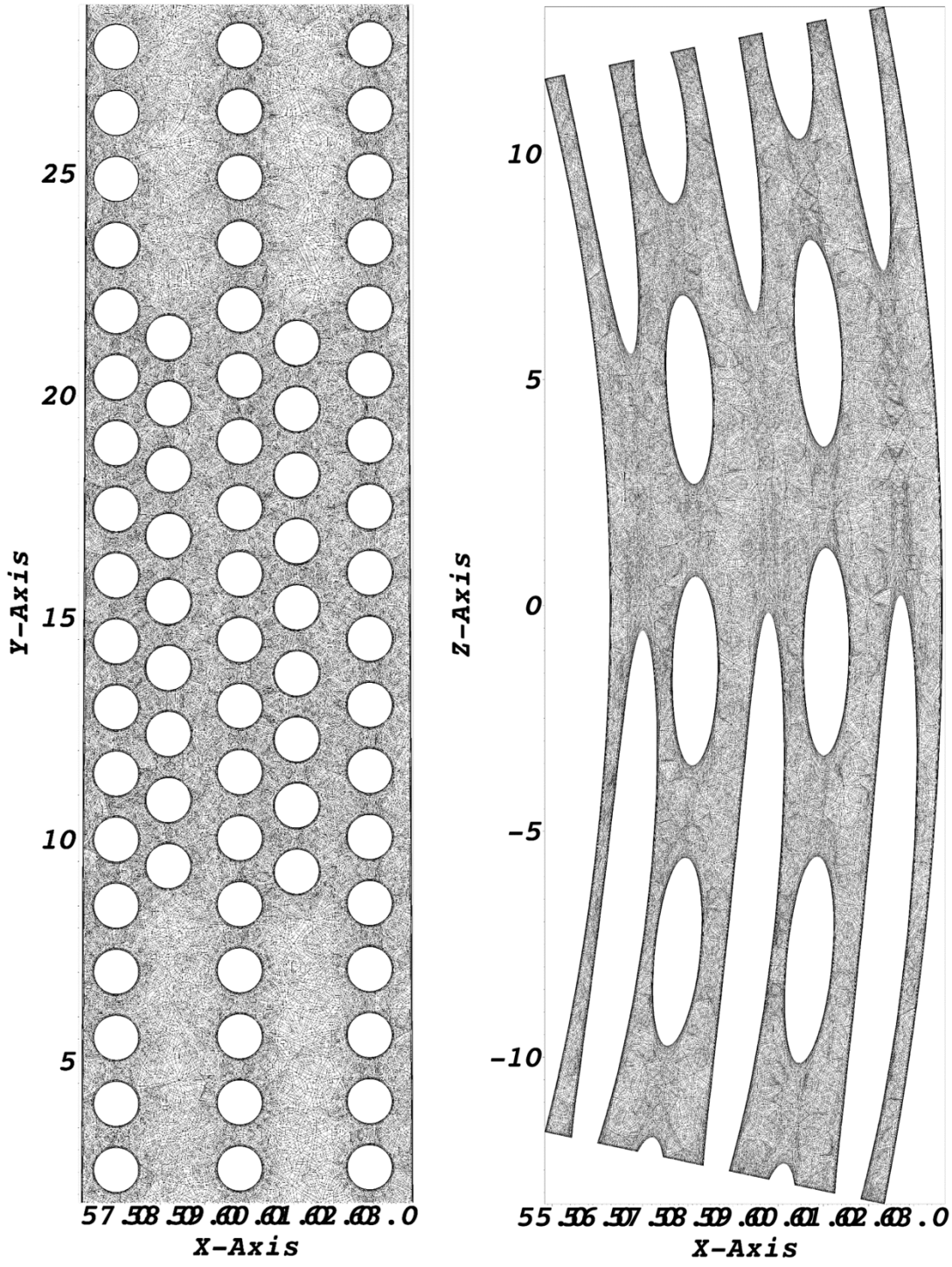

Figure 11: Helical coil steam generator mesh from side view (left) and top view (right)

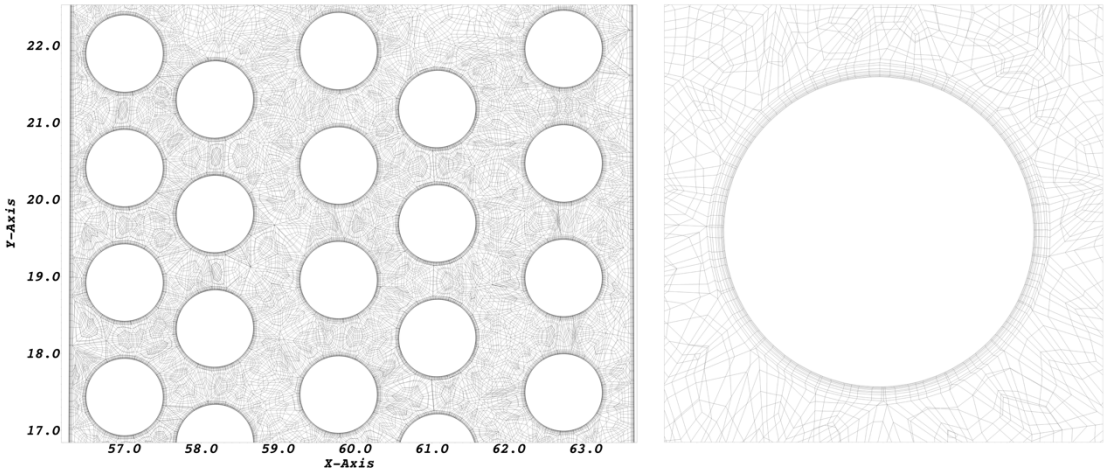

Figure 12: Mesh zoomed-in view

Table 1: Mesh details

Polynomial order	Number of GLL Points
3	262×10^6
5	885×10^6
7	2100×10^6
9	4100×10^6

3.6. Boundary conditions

In the present study, flow is going downward as presented in Fig. 4, with a uniform inlet on top, turbulent outflow boundary at the bottom, and no-slip boundaries at the walls. The inlet and outlet of the flow domain were extruded for 25 tube diameters (d_R).

4. RESULTS[*†]

In this section we present results of our analysis. In the first part of the results section, we shortly present comparisons of the first- and second-order statistics with available experimental data. Second part presents auto- and two-point correlation results. In the third part, we presented results of the spectral analysis and in the fourth part we expanded it with wavelet analysis. Results of the proper orthogonal decomposition analysis for simulation and experimental data are presented in the fifth part. Finally, in the last part we presented visualization of the coherent structures in the flow domain.

[*] Part of this chapter is reprinted with permission from "Numerical Simulation of Isothermal Flow Across Slant Five-Tube Bundle with Spectral Element Method Code Nek5000" by Mustafa Alper Yildiz, Haomin Yuan, Elia Merzari & Yassin Hassan, 2019, Nuclear Technology, 206:2, 296-306. Copyright 2019 by Taylor & Francis.

[†] Part of this chapter is reprinted with permission from "Spectral and modal analysis of the flow in a helical coil steam generator experiment with large eddy simulation" by Mustafa Alper Yildiz, Elia Merzari, and Yassin Hassan, 2019, 80, 108486. Copyright 2019 by Elsevier B.V.

4.1. Grid Independence

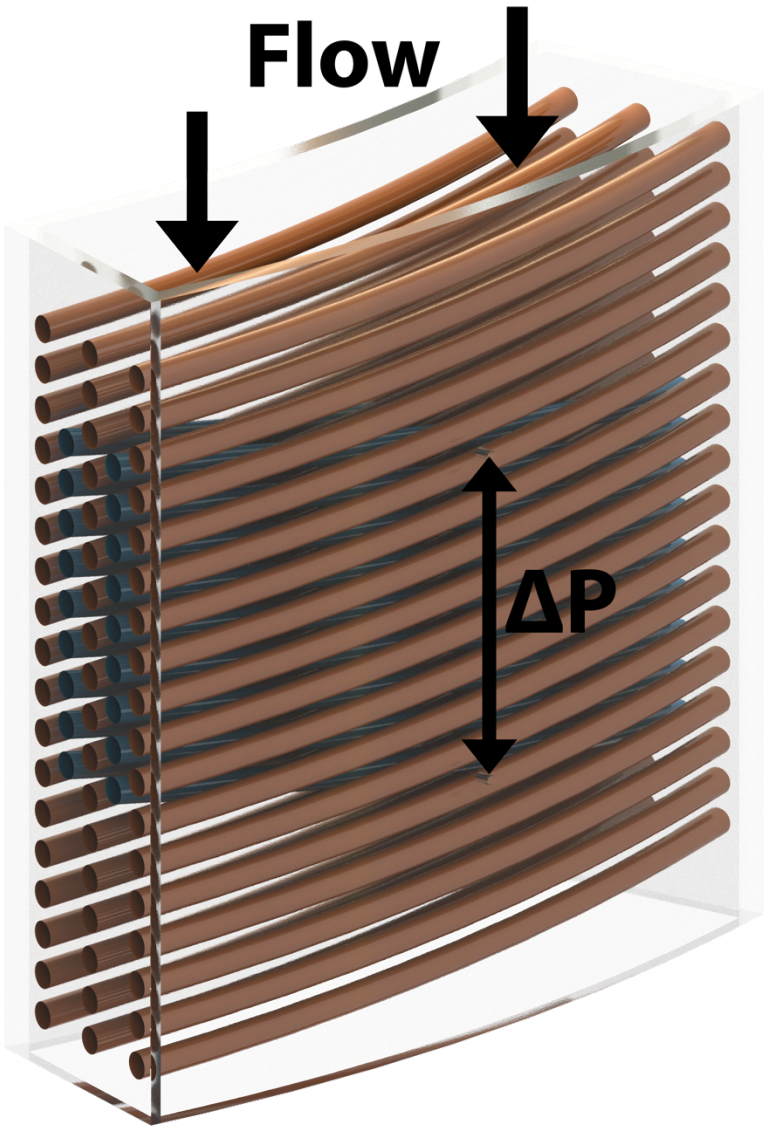

Figure 13: Locations of pressure taps (reprinted) [23]

Grid independence in Nek5000 can be achieved by expanding the mesh in higher polynomial orders. In our study, we considered third, fifth, seventh, and ninth polynomial orders. The number of grid points increases exponentially with an increase in the degree of polynomial order. At the same time, the time step has to be decreased roughly by half

in order to have a stable solution in the finer mesh. To give a general sense of computational cost, 1 second of data requires approximately $1.0x10^6$ core-hours for the third polynomial order, $6.7x10^6$ core-hours for the fifth, $21.5x10^6$ core-hours for the seventh, and $49x10^6$ (49 million) core-hours for the ninth.

Figure 13 shows the locations of the pressure taps where pressure drop was measured in experiments with pressure transducers. Table 1 summarizes the pressure drop at each considered polynomial order with the corresponding error with respect to experimental data. The experimental pressure drop was measured to be 2264±165 Pa. As the table shows, all considered polynomial expansions overestimate the pressure drop. The coarsest mesh has the highest error, whereas the finest mesh has the lowest error compared with the experimental data. This indicates that with increasing polynomial order more energy is captured and numerical dissipation is reduced.

Table 2: Predicted pressure drop and percentage error versus experimental value

Polynomial Order	Pressure Drop (Pa)	Error (%)
3	2666.9	17.79
5	2474.9	9.31
7	2314.3	2.22
9	2305.2	1.82

4.2. Turbulence scales

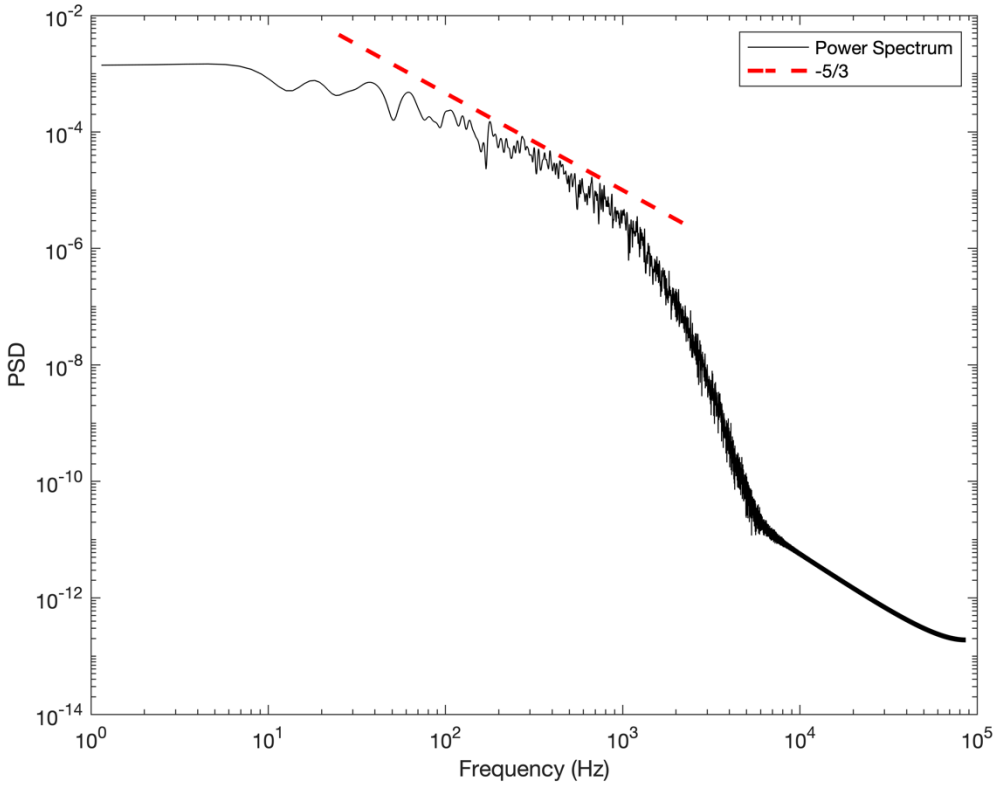

Figure 14: Power spectrum density at a point in the domain

Turbulent scales, which can be thought as eddies, are distributed over a range of scales that extends from the largest scales, which interact with the mean flow, to the smallest scales, where dissipation occurs. The energy spectra exhibiting the energy cascade can be obtained with a two-point correlation of the velocity signal $R_{ij}(r)$ for all r followed by the Fourier transform on $R_{ij}(r)$ [21]. According to Taylor's frozen turbulence hypothesis, spatial correlations can be approximated by temporal correlations [31].

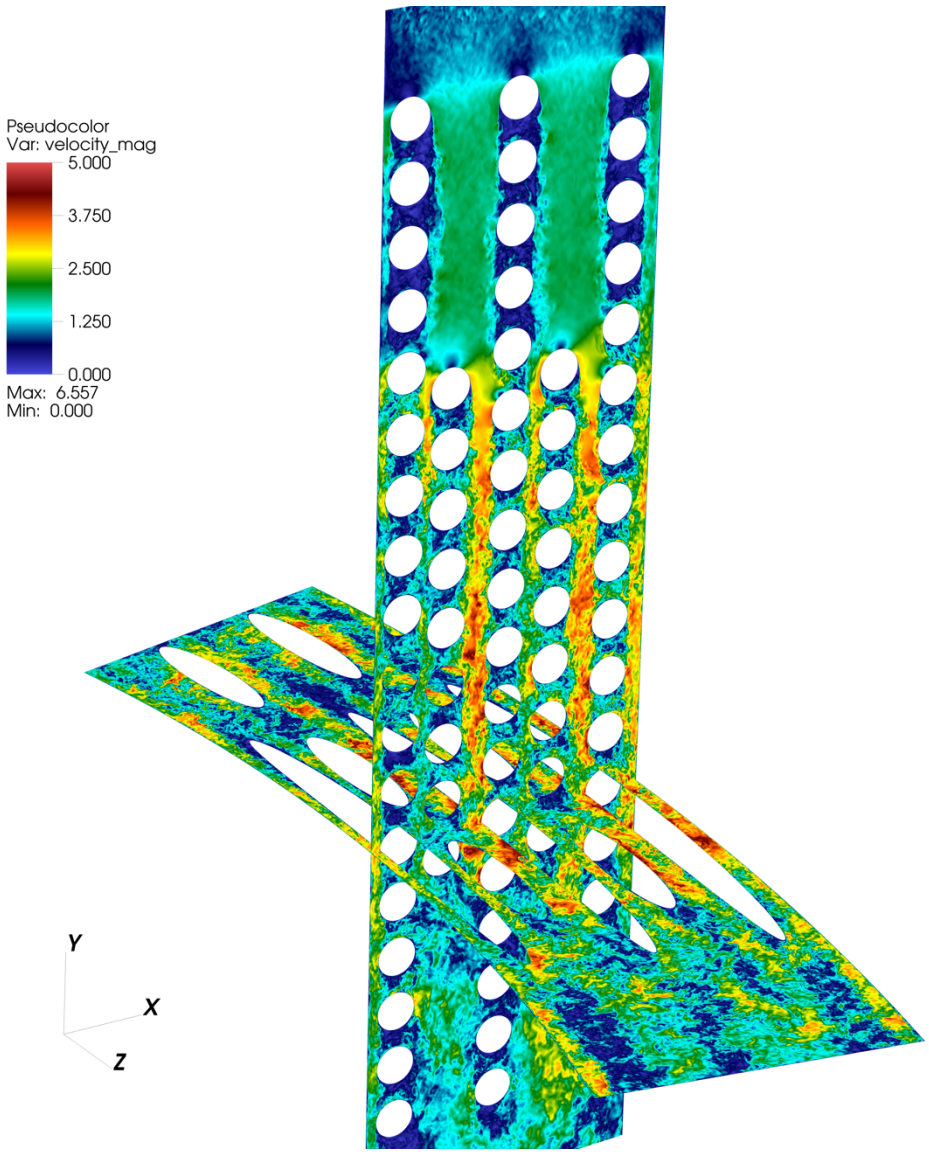

Figure 15: Instantaneous velocity snapshot

According to Kolmogorov's -5/3 law, if the flow is fully turbulent, the energy spectra should exhibit a -5/3 decay in the inertial range [32]. Figure 14 shows the power spectrum in the free stream region between two rods in channel 2. One can clearly see -5/3 slope in the inertial range, which shows that the mesh can capture the scales in the inertial region. Figure 15 shows a snapshot of instantaneous velocity. One can clearly see

a wide variety of flow structures in the flow: big flow structures form at the beginning of the flow channels (between adjacent tube columns), and further downstream they break down into smaller structures. This behavior of the flow will be further discussed in the paper.

As a second test to show that the mesh used in this study is sufficient for LES calculations, mesh sizes from different polynomial expansions were compared with Taylor's microscale. Taylor's microscale is given as follows [21]:

$$\lambda = \sqrt{15\frac{\nu}{\epsilon}}u' , \tag{9}$$

where ν is the kinematic viscosity, ϵ is the dissipation rate, and u' is the root-mean-square of velocity fluctuations. We note that in the present case, while using spectral truncation instead of an eddy viscosity model, it is relatively easier to use classic subgrid-scale viscosity model in the post processing stage.

Taylor microscales were calculated with a realizable $k-\epsilon$ turbulence model in STAR-CCM+. A mesh of 125M elements was constructed with an average y^+ of 0.8 at the near-wall grid points. An all y^+ wall treatment was employed for modeling near-wall turbulence quantities. Statistics were collected for 15 seconds after the flow was fully developed. Convergence of the statistics was checked with point probes at various locations in the domain.

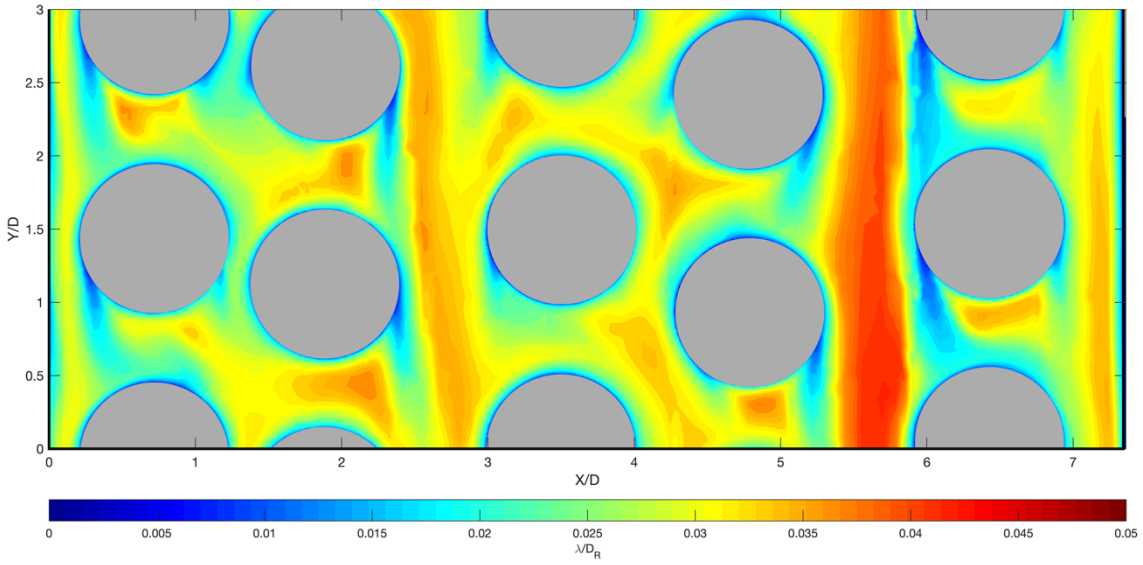

Figure 16: Taylor microscales normalized with rod diameter at PIV window

Figure 16 shows a contour plot of the calculated Taylor microscales at location where PIV snapshots were recorded in the experiments. Taylor microscales are greater at the free stream between the rods and at the wakes behind the tubes and smaller at the walls and where the flow separates from the tubes. The average ratio of mesh size to Taylor's microscales was 0.99, 0.79, and 0.64 for the fifth-, seventh-, and ninth-order expansion, respectively. In the fifth-order expansion, the mesh size is on the order of Taylor's microscales, while in higher polynomial orders the mesh size is smaller than Taylor's microscales. These results show that with the current mesh discretization, some scales at dissipation range can be resolved, and we conclude that the mesh in the seventh polynomial order expansion is fine enough for LES calculations. Since running simulations and storing data in higher polynomial orders (i.e., ninth-order polynomial

expansion) is expensive, we will conduct our analysis with seventh polynomial order expansion.

4.3. Time-averaged results

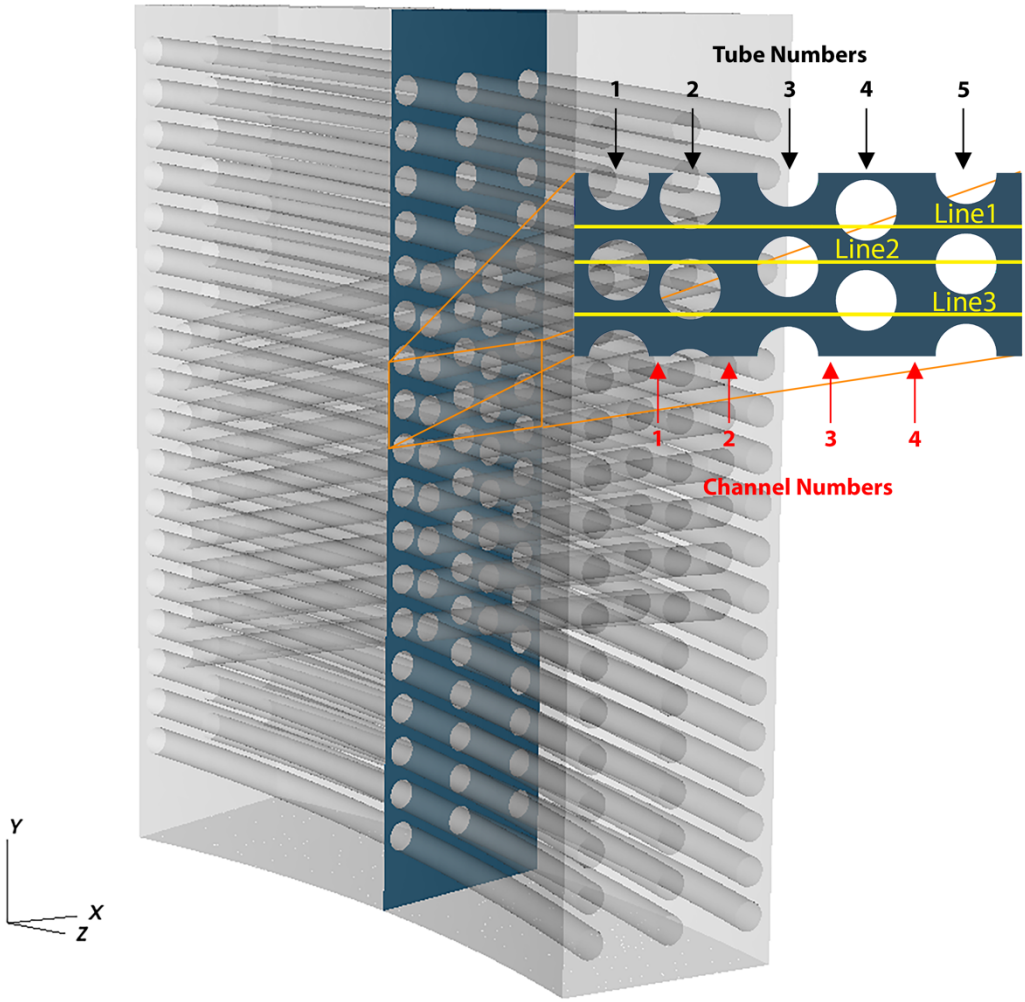

Figure 17: Location of line plot comparisons (reprinted) [20]

In this section, we compare our time-averaged results with available experimental data from PIV measurements. One of the objectives of this study is to validate Nek5000 for novel HCSG designs. Wall-to-wall comparisons were made at three successive rows in the PIV window. The location of the PIV window in the domain and selected lines are shown in Figure 17. Time-averaged quantities were collected for 54 convective units (CUs), where one physical second is equivalent to 34 CUs. For brevity, in this paper we show only streamwise velocity and streamwise normal stress comparisons. For more detailed comparisons of the first- and second-order statistics, the reader is referred to [20].

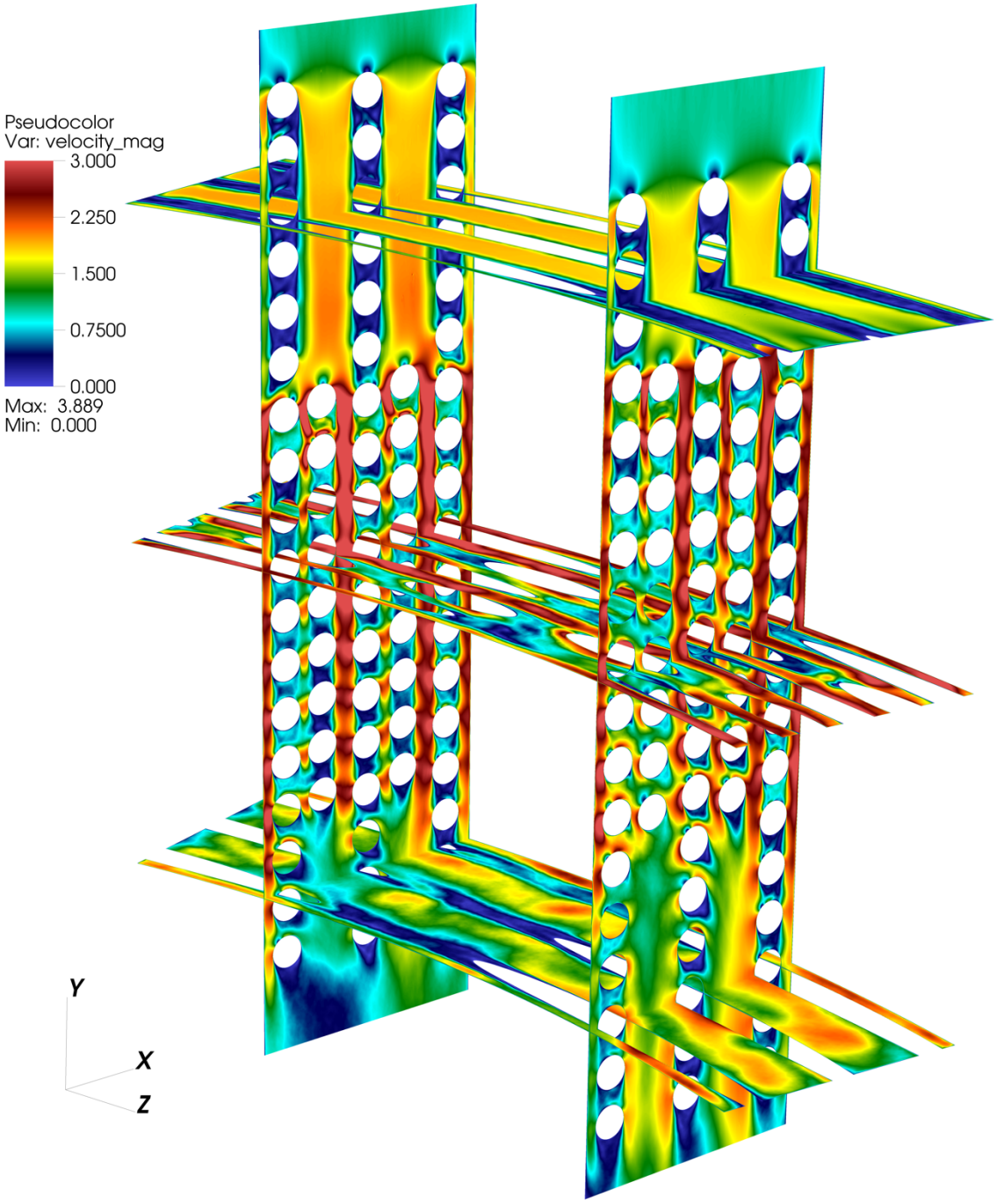

Figure 18: Time-average velocity magnitude contour

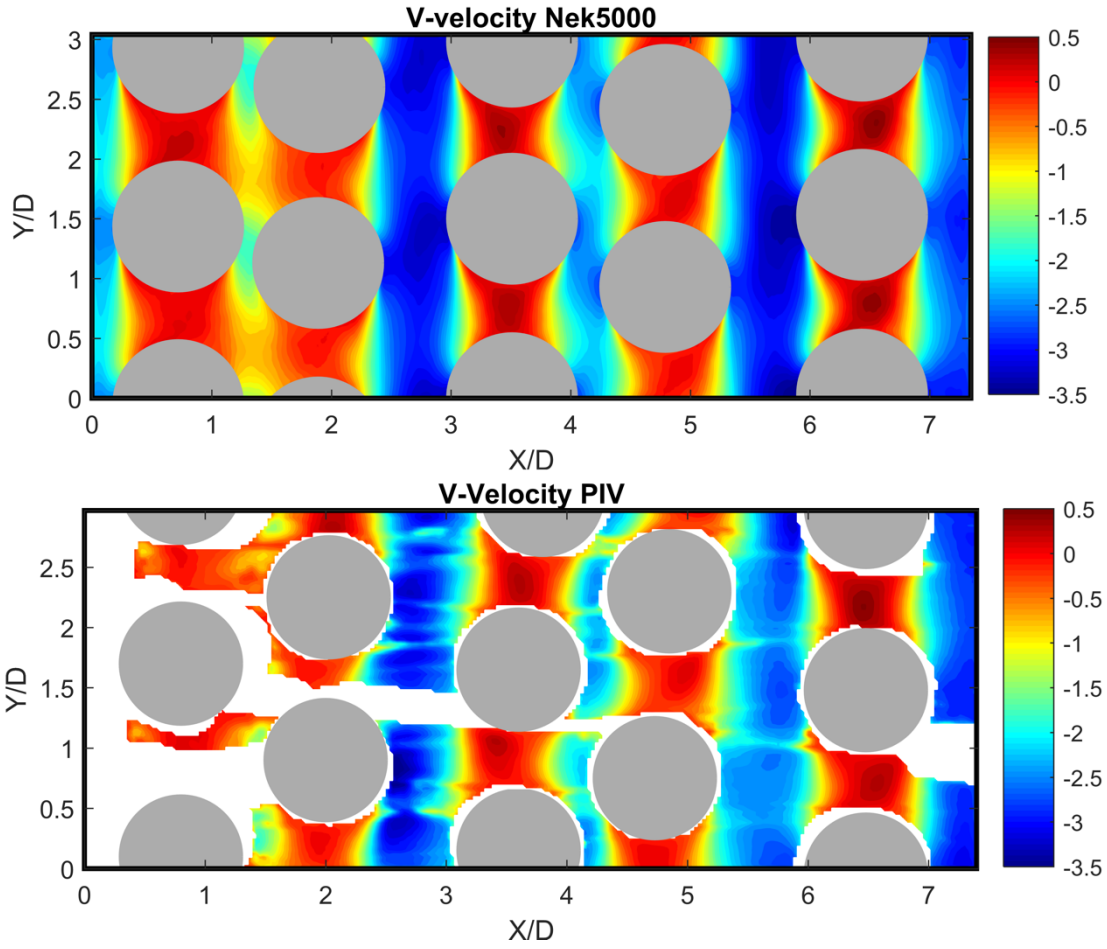

Figure 19: Average streamwise velocity contour LES (top) and PIV (bottom)

Figure 18 shows the time average velocity magnitude contour in the flow domain from the LES calculations. Figure 19 shows contour plots of the average streamwise velocity at the location of the PIV window from LES (top) and from PIV measurements (bottom). Qualitatively, the contour plots of the streamwise average velocity from LES calculations show good agreement with PIV data.

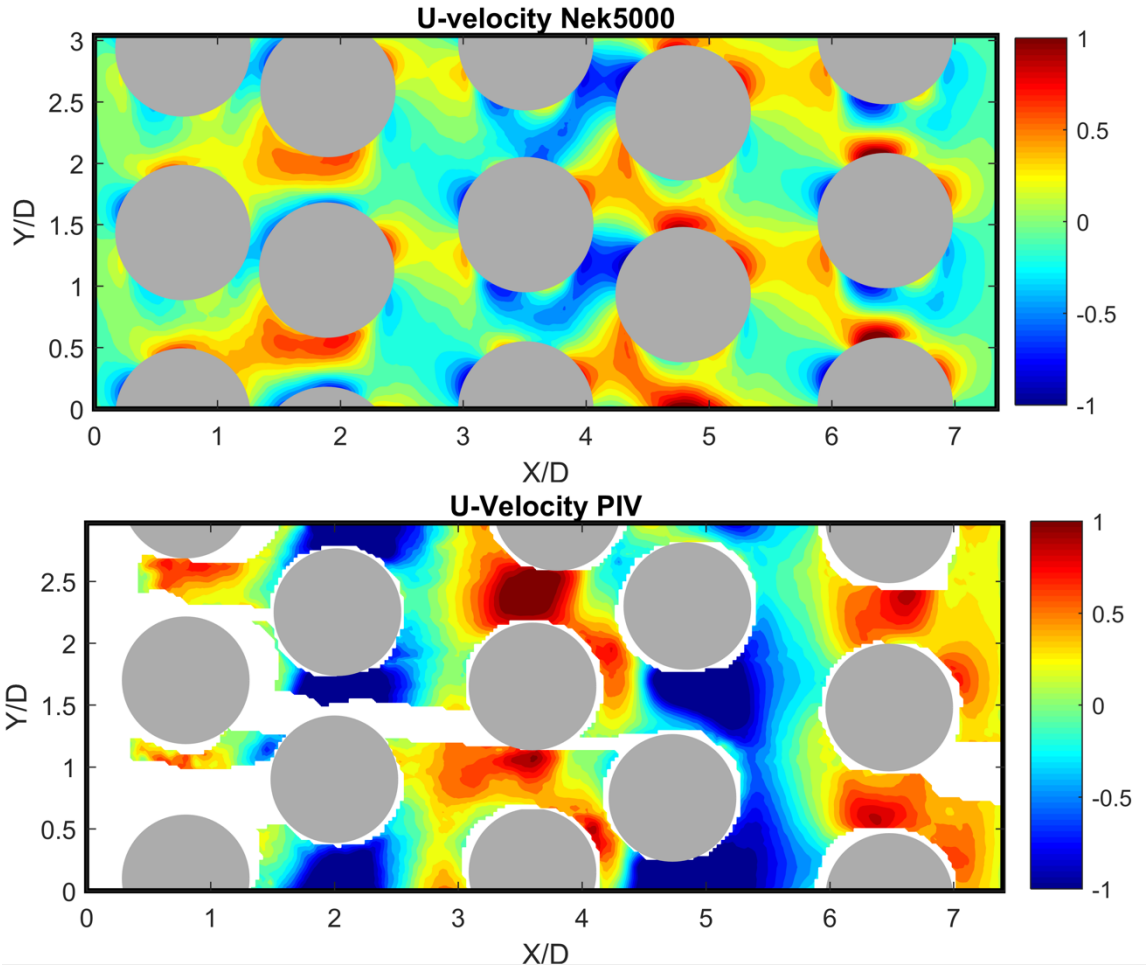

Figure 20: Average spanwise velocity contour LES (top) and PIV (bottom)

Figure 20 shows the normalized average spanwise velocity contour from LES (top) and PIV (bottom). Comparison of two contour plots of the normalized spanwise velocity component show some discrepancy at some locations. One of the possible reasons for discrepancy in spanwise direction could be slight geometrical differences between experimental facility and computational domain, to which the span-wise velocity tends to be sensitive. Such differences have very small impact on pressure drop and streamwise

velocity. We note that we attempted to represent the geometry as accurately as possible but the translation of the real geometry to CAD file has inherent uncertainties. Another possible reason for the discrepancies can be, resolution and frame rate of PIV images could be not enough to capture spanwise velocity component. Since flow is predominantly in streamwise direction (Y-direction), measuring the mean component is less dependent on the sampling ratio. However, since magnitude of the spanwise component is significantly smaller may require higher frame rate and higher resolution to capture velocity in spanwise direction. As a second comparison, our results in spanwise direction were qualitatively compared to PIV results of Lee et. al. [33], which were captured on the same facility at lower Reynolds number, higher frame rate, and higher resolution. In their study they focused only on a wake of a single rod. Qualitative comparison shows that flow around a tube in the wake of a rod in spanwise direction of Lee et. al. shows similar characteristics with our results.

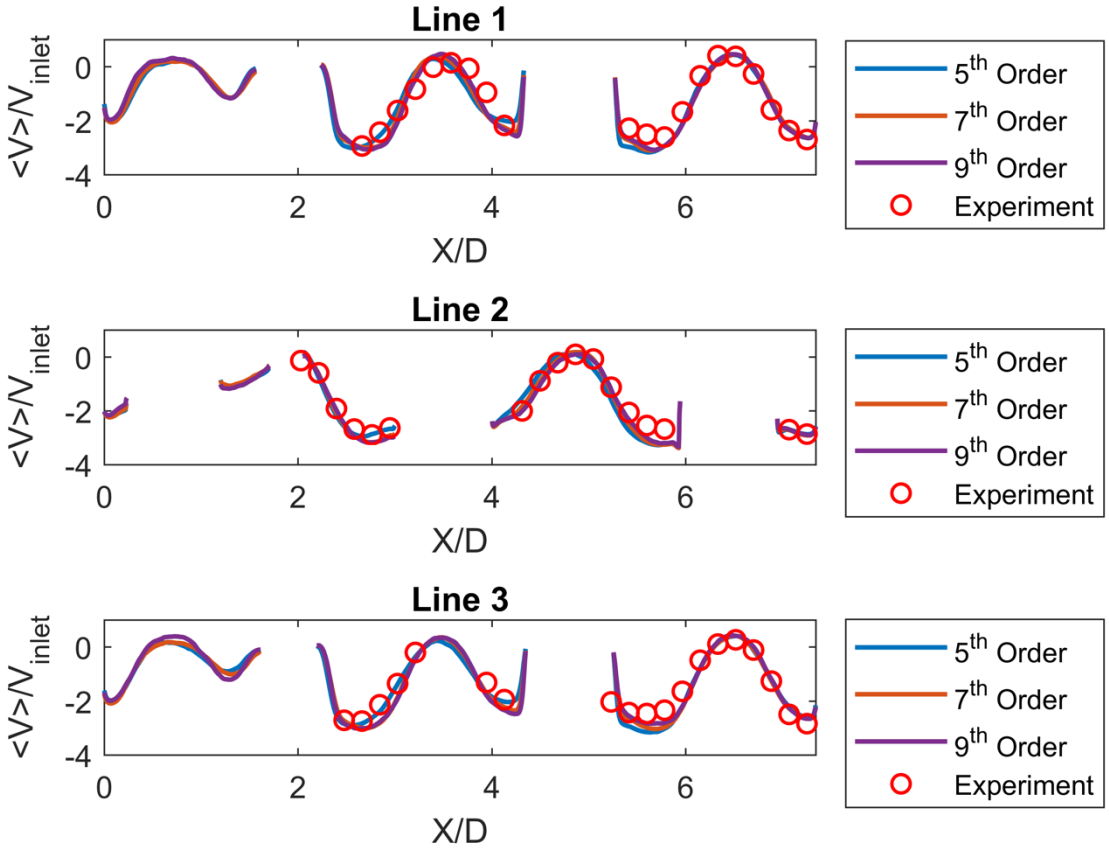

Figure 21: Streamwise time-averaged velocity on selected lines

Figure 20 compares the time-averaged streamwise velocity on three lines for the fifth, seventh, and ninth polynomial expansions with PIV data. The velocity profiles in the seventh and ninth polynomial order expansions are close, whereas the velocity profile in the fifth polynomial order expansion shows slight discrepancies. The streamwise velocity components on the selected lines show good agreement with experimental data.

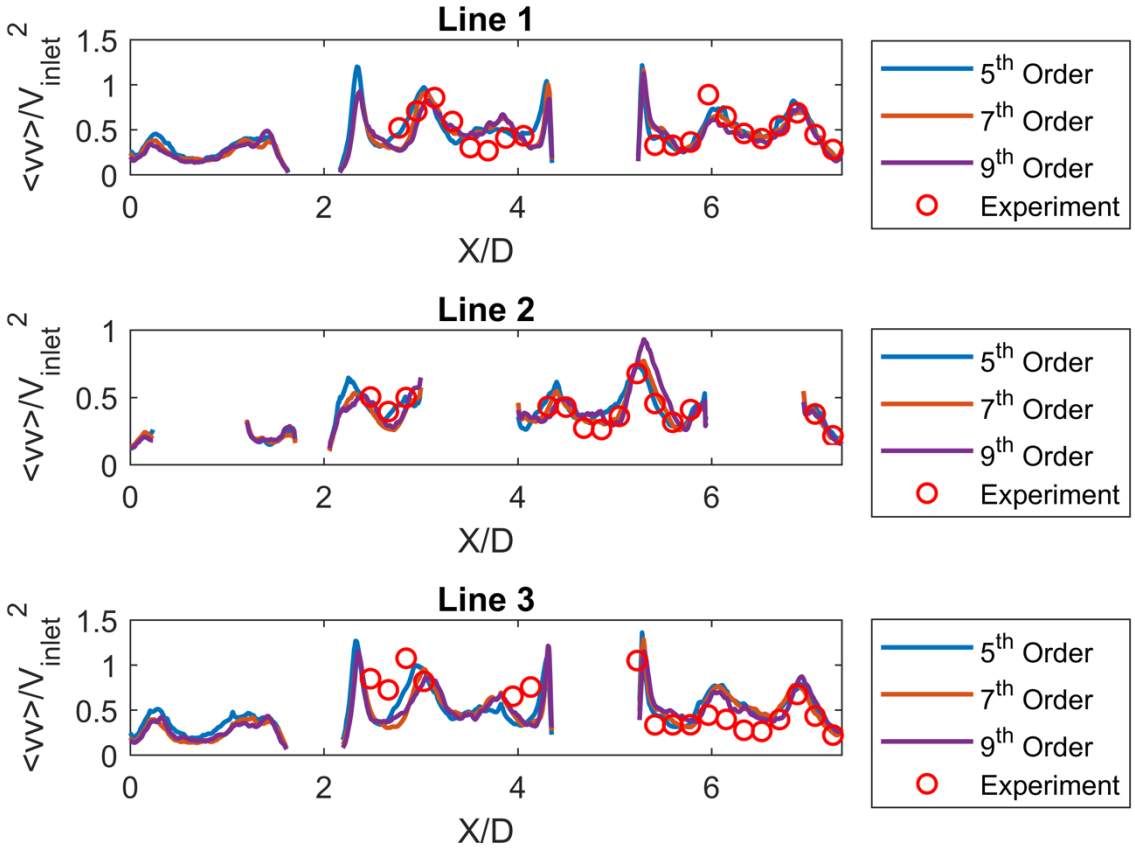

Figure 22: Streamwise normal time-averaged Reynolds stresses

Figure 12 compares the streamwise normal stresses from LES calculations with PIV measurements. The Reynolds stresses are normalized by the square of the inlet velocity. On the first and second lines, the streamwise Reynolds stresses show good correlation with PIV results. Humps at the wakes of the tubes are due to a shear layer between the tube wake and the mainstream in the channels. The streamwise component of Reynolds stresses at the wake of the first tube is smaller than at the rest of the tube wakes. This may be attributed to the nonsymmetrical tube configuration. The gap between tubes 1 and 2 (channel 1 as in Fig. 9) is the narrowest among the gaps between the other tubes. The flow velocity around the first tube is smaller than that of the other tubes.

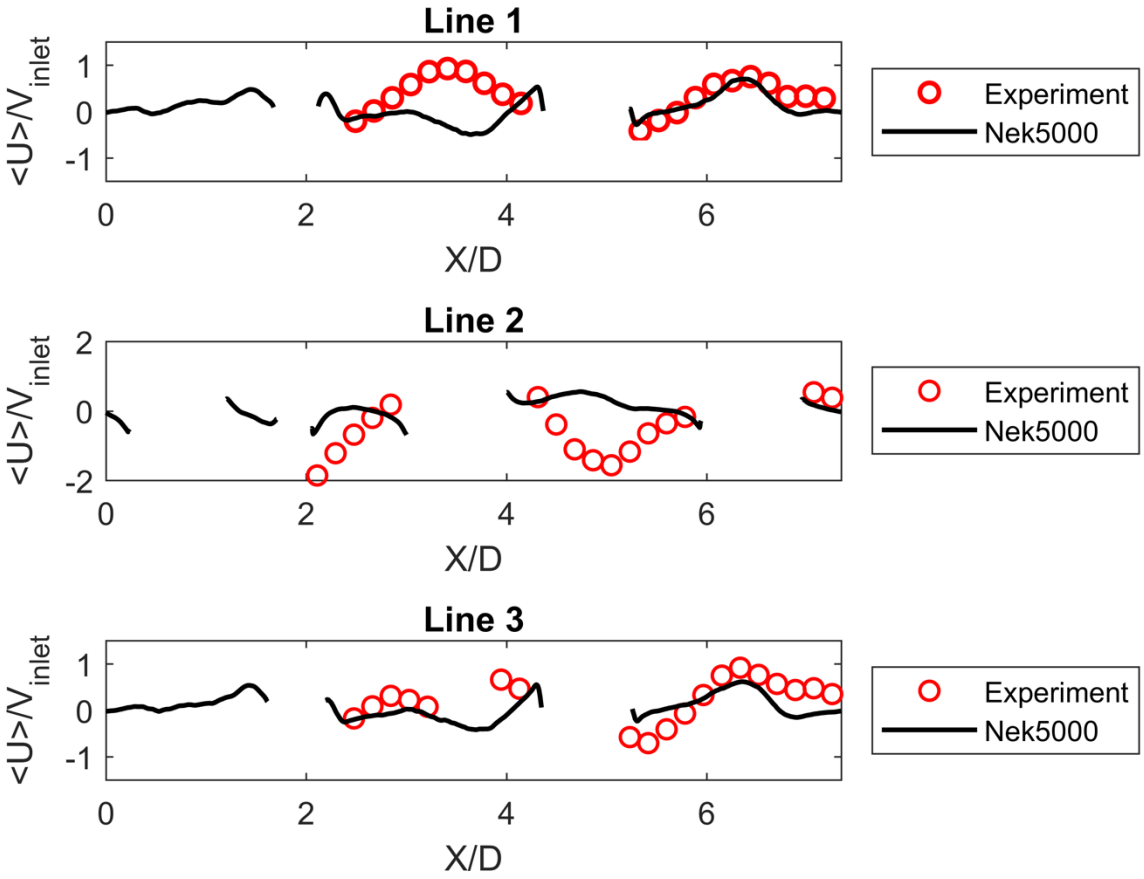

Figure 23: Spanwise time-averaged velocity on selected lines

Line comparison of normalized time-averaged spanwise average velocity from simulation and PIV at selected locations are presented in Fig. 22. Experimental data was compared with seventh polynomial expansion results. Spanwise velocity from simulation (Figure 22) shows good correlation with PIV data in the wake region of the rods close to wall in Line 1 and Line 3. Further at the inner side of the tube bundle, results for spanwise velocity show some discrepancy at some locations. Overall the velocity comparisons show good agreement between numerical simulations and experiments

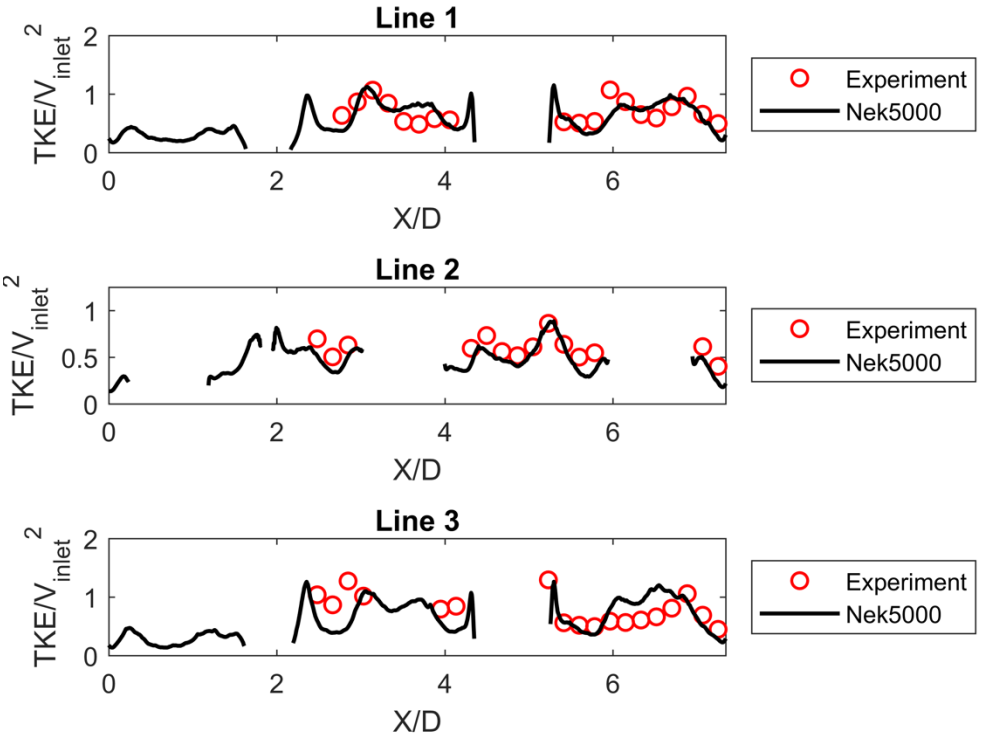

Figure 24: Time-averaged turbulent kinetic energy on selected lines

Line comparison for normalized turbulent kinetic energy on lines 1, 2, and 3 are shown in Fig. 23. It can be seen that on line 1 and 2 TKE shows good correlation with PIV data. Line 3 shows comparable TKE magnitude between experimental data and simulation results. Overall the LES simulation results for the TKE show good agreement with the PIV data given the complex geometry.

Uncertainty of the PIV measurements were reported in [24]. Based on the reported standard deviation, uncertainty of the mean velocity with 95% confidence is 0.1%, and similarly uncertainty of the variance with 95% confidence is 0.016%.

4.4. Flow mixing

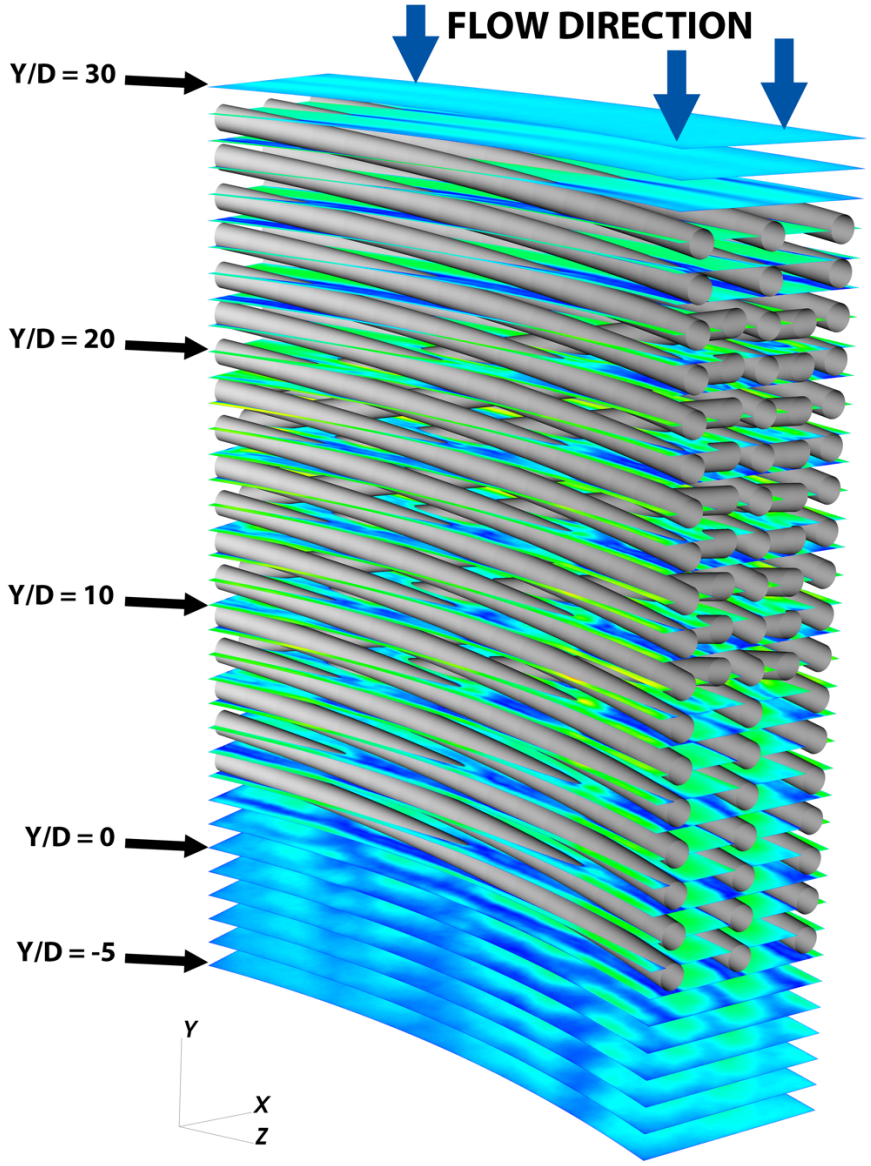

Figure 25: Locations of the horizontal planes in the computational domain (reprinted) [20]

Flow inside the steam generator model is complex and presents time-averaged secondary flow due to curvature of the rods and helix angle of the coil tubes [18]. Flow characteristics were analyzed to quantify the secondary flow intensity due to the complex geometry of the steam generator. Secondary flow can enhance heat transfer but may also bring additional pressure drop. It was identified as a key feature of the helical coil flows in Yuan et al. [18]. Figure 24 shows the locations of horizontal planes where secondary flow intensities (SFI) were evaluated.

Secondary flow intensity was evaluated as an area averaged quantity, which is given by

$$SFI = \frac{\int_A \sqrt{V_x^2 + V_z^2}\, dA}{\int_A V_y\, dA} \tag{3}$$

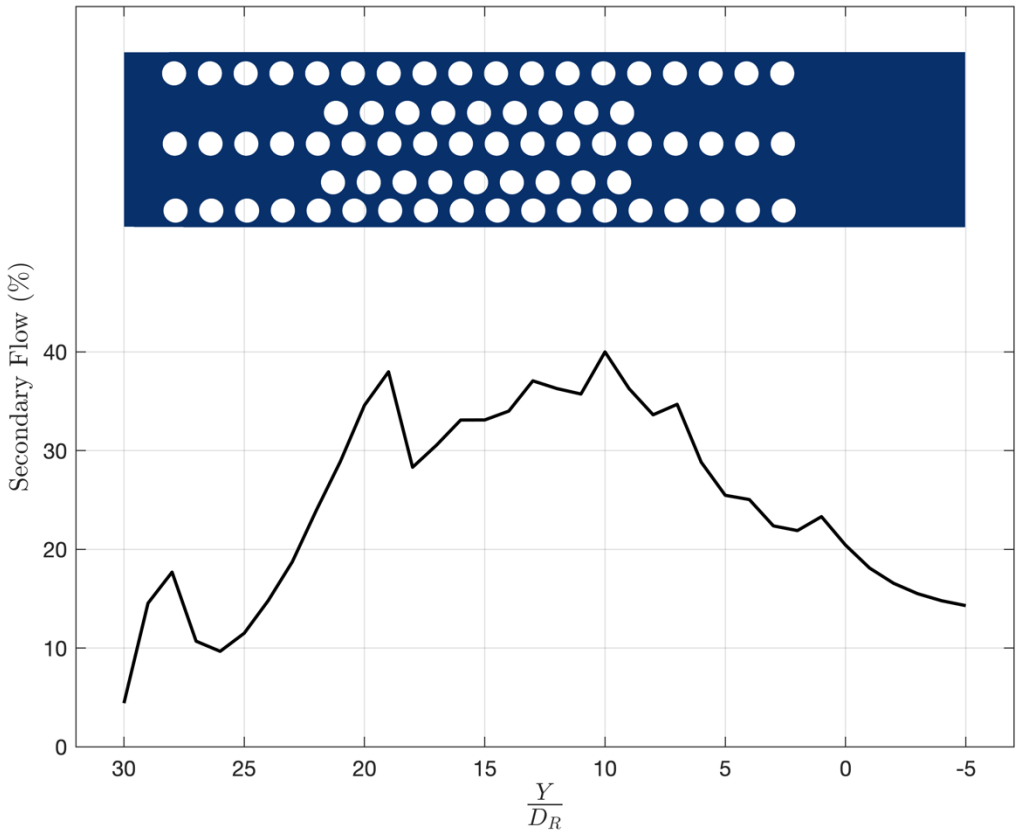

Figure 26: Secondary flow intensity across the helical coil steam generator

Figure 25 shows SFI evaluated at 39 horizontal planes across HCSG. Three distinct peaks appear in the SFI across HCSG. The first peak appears at Y/D=28 where the flow first encounters the outer coil tubes (tubes 1, 3, and 5). The Second peak appears at Y/D=19 where flow encounters inner coil tubes (tubes 2 and 4). The highest magnitude of the secondary flow intensity is at the third peak (Y/D=10), where flow passes inner coil tubes. Further downstream, SFI decays exponentially after flow passes coil tubes (Y/D=1). It can be seen that the helical structure of the tubes with oppositely slant adjacent tubes create secondary flow, which intensity increases up to 40% of primary flow. This non-negligible secondary flow enhances cross flow in steam generator, which could enhance

heat transfer but may also increase pressure drop and tube vibration. Effects of secondary flow in HCSGs should be investigated further with additional experiments and simulations.

Figure 26 shows secondary flow structure across HCSG at different elevations. At Y/D=28, where the flow hits coil tubes, secondary flow shows well-ordered characteristic following the curvature of the tube. The upstream flow is accelerated by tube coils. Further downstream at Y/D=19, secondary flow shows irregular structure. The Flow accelerates when interacting with the tubes and it enhances mixing. At Y/D=10, where the flow passed inner tubes 2 and 4, it can be seen that vortical structures start to form, which can enhance the secondary flow patterns. This can be seen clearly after flow passes all coil tubes (Y/D=1), where small energetic vortical structures form. Counter rotating vortex structures enhance crossflow by accelerating surrounding flow. Moving downstream, formed vortexes stretch and lose their energy.

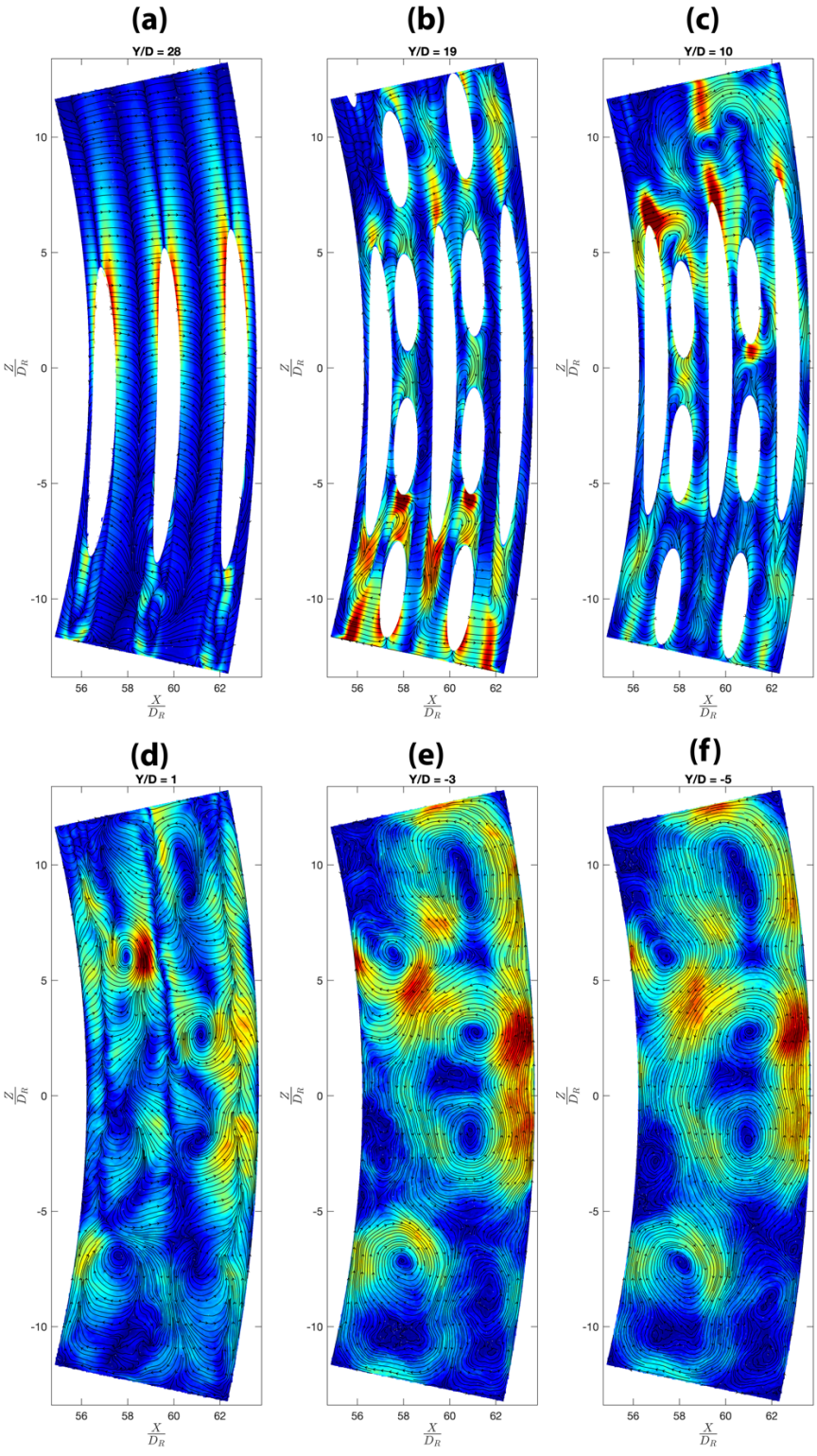

Figure 27: Secondary flow structures across the helical coil steam generator

4.5. Auto- and two-point correlation analysis

In this section, we analyze turbulence time scales and length scales of the flow in HCSGs. We can define time scale and length scale of large energy containing eddies with autocorrelation and two-point correlation, respectively. Autocorrelation is a two-point correlation of a turbulent fluctuation with a separation in time. To evaluate the resolved turbulence time scale, we apply an autocorrelation operator. The normalized autocorrelation is defined as follows:

$$\rho(x,s) = \frac{\langle u'(x,t)u'(x,t+s)\rangle}{\langle u'^2(x)\rangle}\,, \tag{10}$$

where $u'(x,t)$ is the fluctuation at point x and time t and $u'(x,t+s)$ is the fluctuation at the same location in space with lag time s. The integral timescale represents the timescale of large energy-containing eddies and is defined as

$$\tau = \int_0^{t_s} \rho(s)ds\,, \tag{11}$$

where the upper limit of the integral represents the time when the correlation function intercepts zero. Similarly, the normalized two-point correlation is defined as

$$R_{ii}(x,\eta) = \frac{\langle u'(x)u'(x+\eta)\rangle}{u'_{rms}(x)u'_{rms}(x+\eta)}\,, \tag{12}$$

where $u'(x)$ is the velocity fluctuation at the analyzed location and $u'(x+\eta)$ is the velocity fluctuation separated by distance η. From the two-point correlation, the integral length scale represents the length scale of large energy-containing eddies. Similarly, it is defined as

$$L_{int}(x) = \int_0^{\eta_s} R_{ii}(x,\eta)d\eta \ , \tag{13}$$

where again the upper limit of the integral represents the separation distance where the correlation between two points intercepts zero.

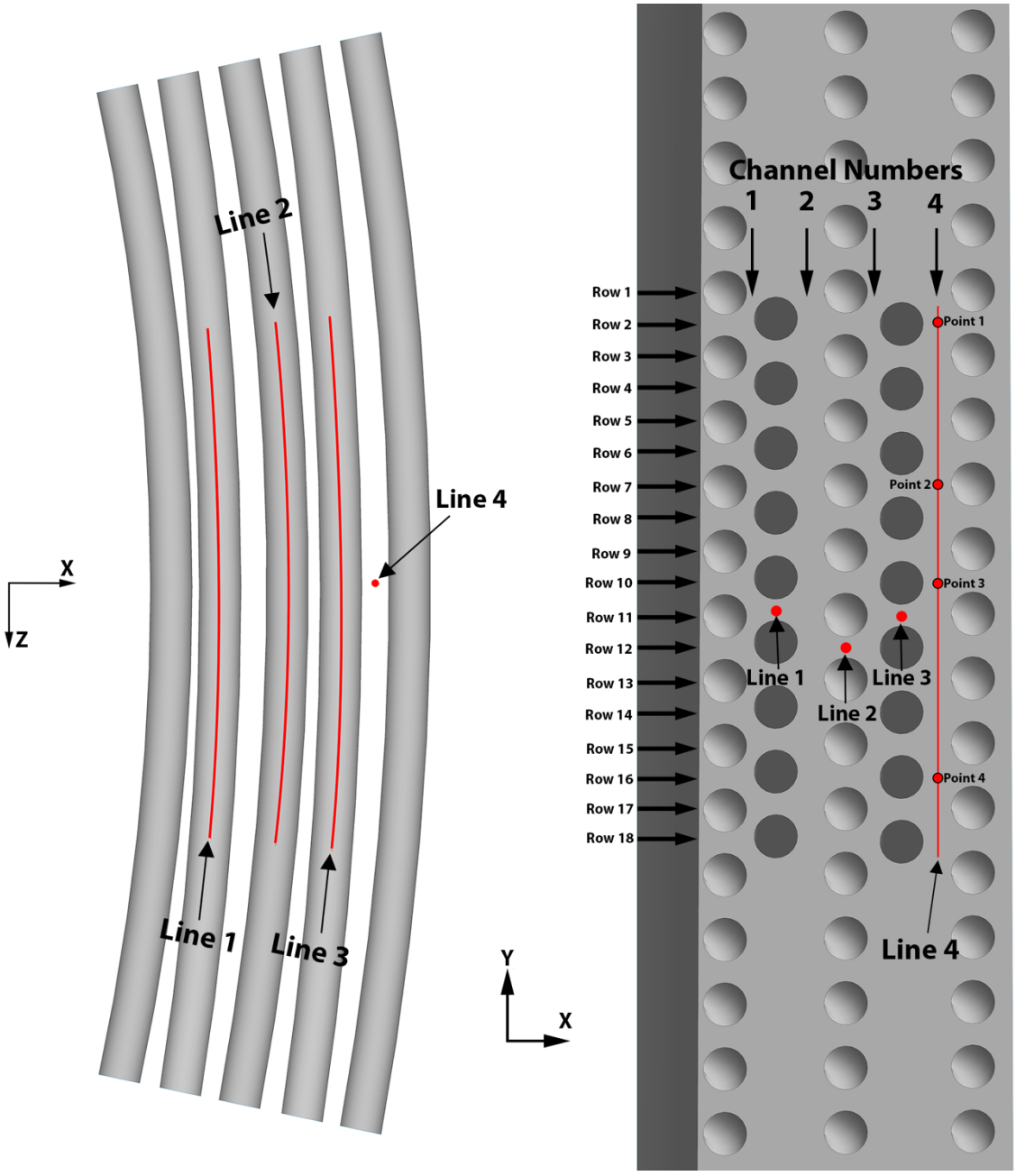

Figure 28: Locations of sampling lines for two-point correlation analysis. Top view (left) and side view (right) (reprinted) [23]

Fluctuating velocity components were recorded at 1,000 sampling points along four lines in the domain, as shown in Figure 27. Two of the sampling lines are at the 11th row extending along the wakes of the second and fourth tubes, and from now on they will be called the first and third sampling lines, respectively. Another line is at the 12th row extending along the wake of the third tube, and from now on it will be called the second sampling line. The last sampling line is at the center of channel 4, and it will be called the fourth sampling line.

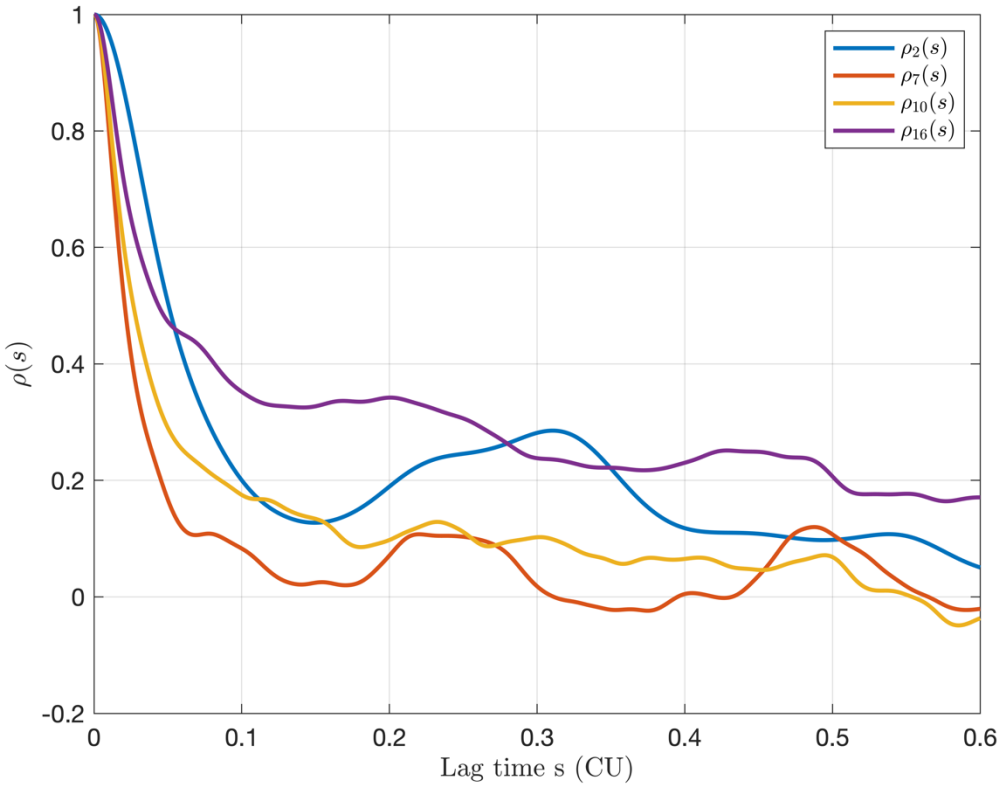

Figure 29: Auto-correlation profile for selected points on sampling line 4

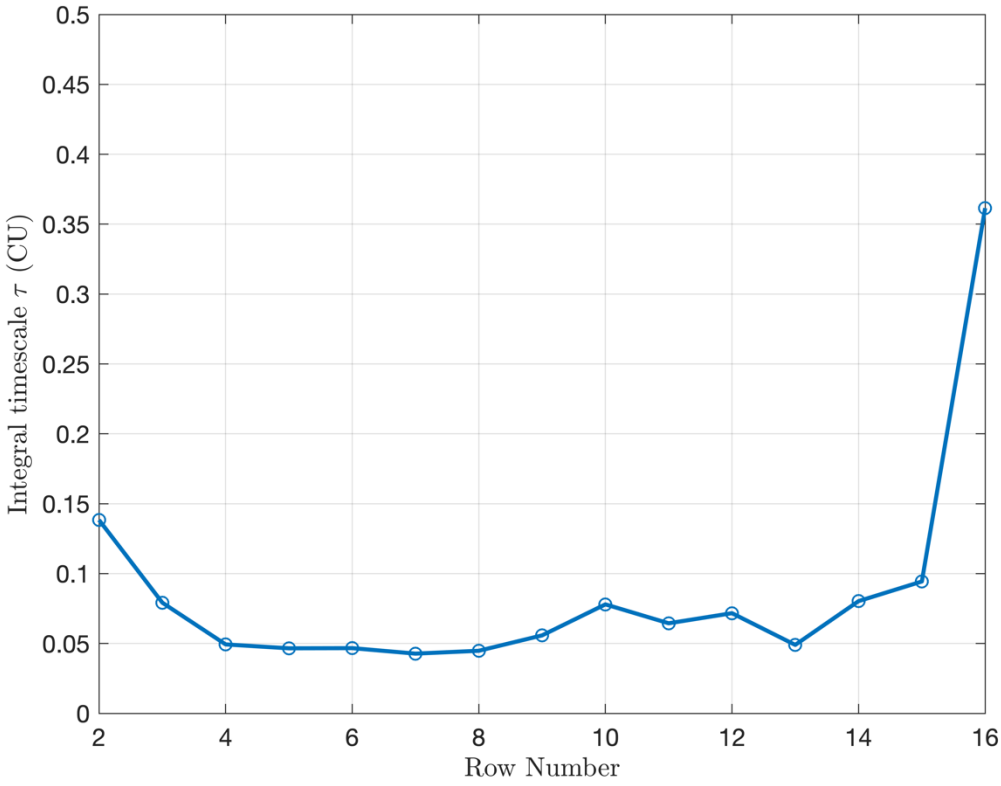

Figure 30: Estimated integral timescale at each row

Figure 28 shows the normalized autocorrelation profiles for selected points on sampling line 4. Figure 29 shows the estimated integral timescales at each row. Selected point locations are shown in Figure 27. The timescales are presented in convective units, which are nondimensional time units. As a general trend in two-point correlation analysis, one expects to see a wider correlation function in low-frequency processes (and hence higher integral quantities) than in high-frequency processes. From Figure 28, one can see that in the second row the autocorrelation function is wider compared with rows downstream at the inner region of the tube bundle. Also, the integral timescale of eddies

is larger in the second row. After the eighth row the integral timescale starts to grow, and at the 16th row it reaches maximum. One can interpret this trend as follows: Beginning from the top row farther downstream, eddies start to break up into smaller structures, and closer to the end of the channel they merge together and form bigger structures. These results are consistent with spectral analysis of velocity fluctuation signals at select points, which will be discussed in the next section.

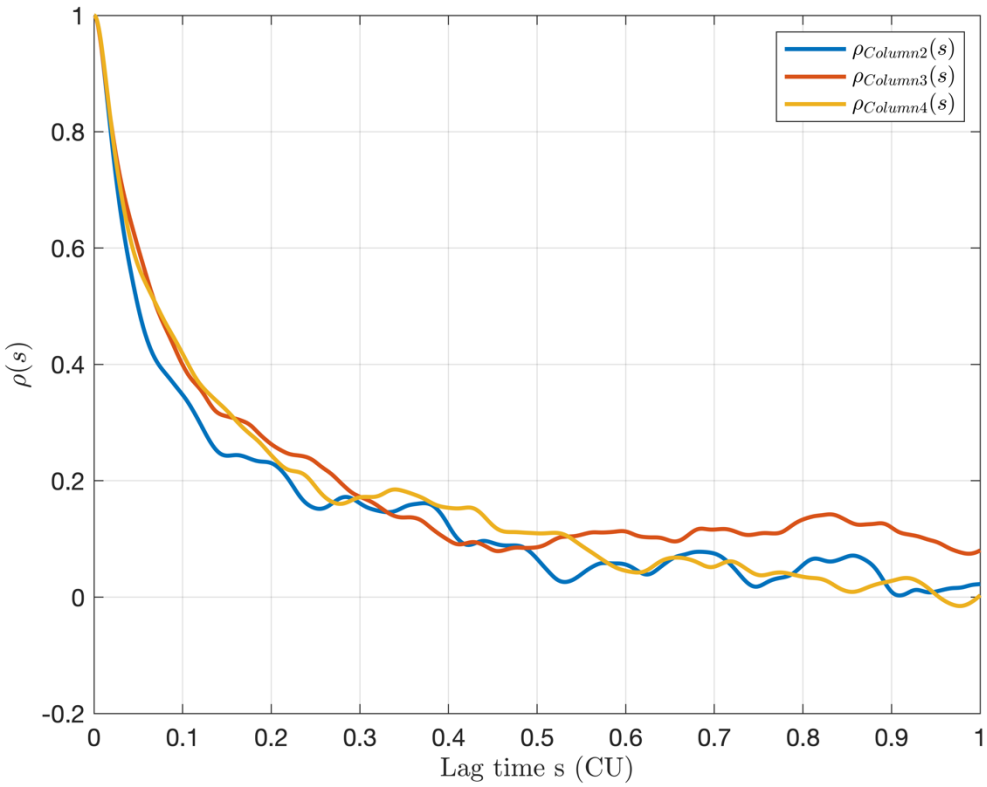

Figure 31: Auto-correlation profile on selected points below the 2nd, 3rd, and 4th tubes

Figure 30 shows the autocorrelation function of selected points estimated on the first, second, and third sampling lines. The analyzed points are located at the center of the sampling lines (at $z = 0$). The autocorrelation functions for all three locations show a similar decay rate. The estimated integral timescales of the first and third sampling lines, which have the same inclination angle, are similar: 0.15 CU and 0.16 CU, respectively. The integral time scale for the second sampling line, is higher, at 0.26 CU; this sampling line has a smaller inclination angle compared with that of the adjacent lines.

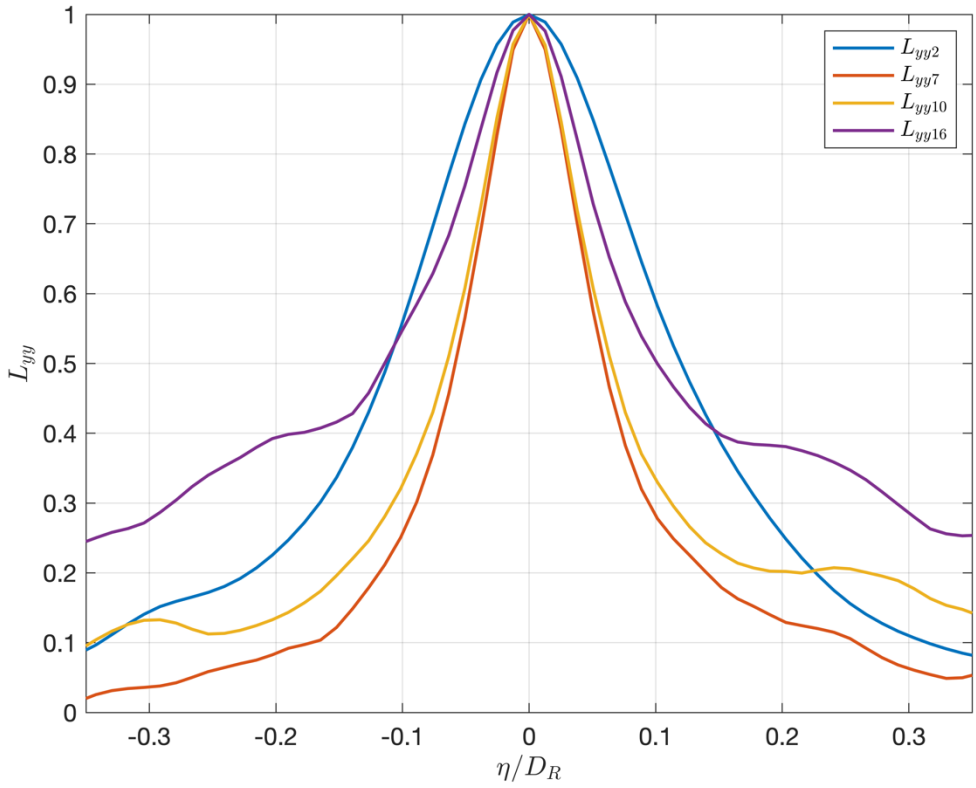

Figure 32: Two-point correlation profile for the same points on sampling line 4

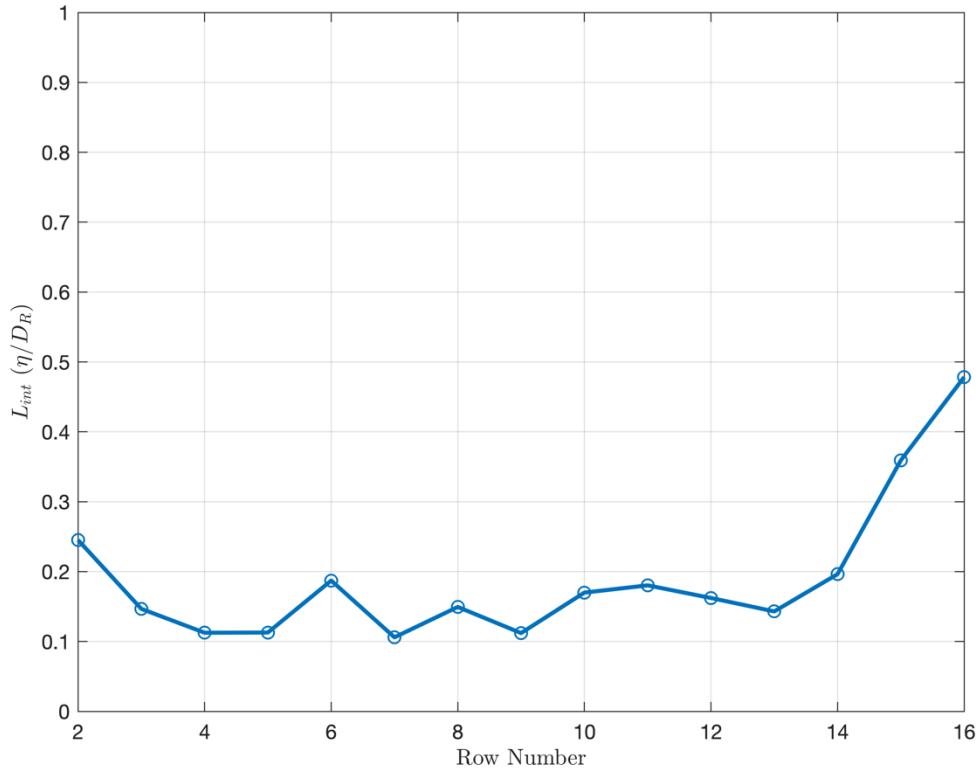

Figure 33: Integral length scales for each row in the channel

Figure 31 shows the normalized two-point correlation profiles of the streamwise fluctuating velocity component for the same points on sampling line 4 along with integral length scales (Figure 32) for each row in the channel. The integral length scales are normalized with the tube diameter. The two-point correlation profiles along with the integral length scales show results similar to the autocorrelation results, which is an expected outcome from Taylor's frozen turbulence hypothesis. The two-point correlation profile at the second row is wider than at locations downstream at the inner region of the tube bundle. In addition, the integral length scales show behavior similar to that of the

integral timescales. From the beginning of the channel, the integral length scales decrease whereas closer to the end of the channel they increase, indicating that the turbulent structures at the beginning of the channel break down into smaller structures whereas closer to the end of the channel they merge to form bigger structures in the streamwise direction.

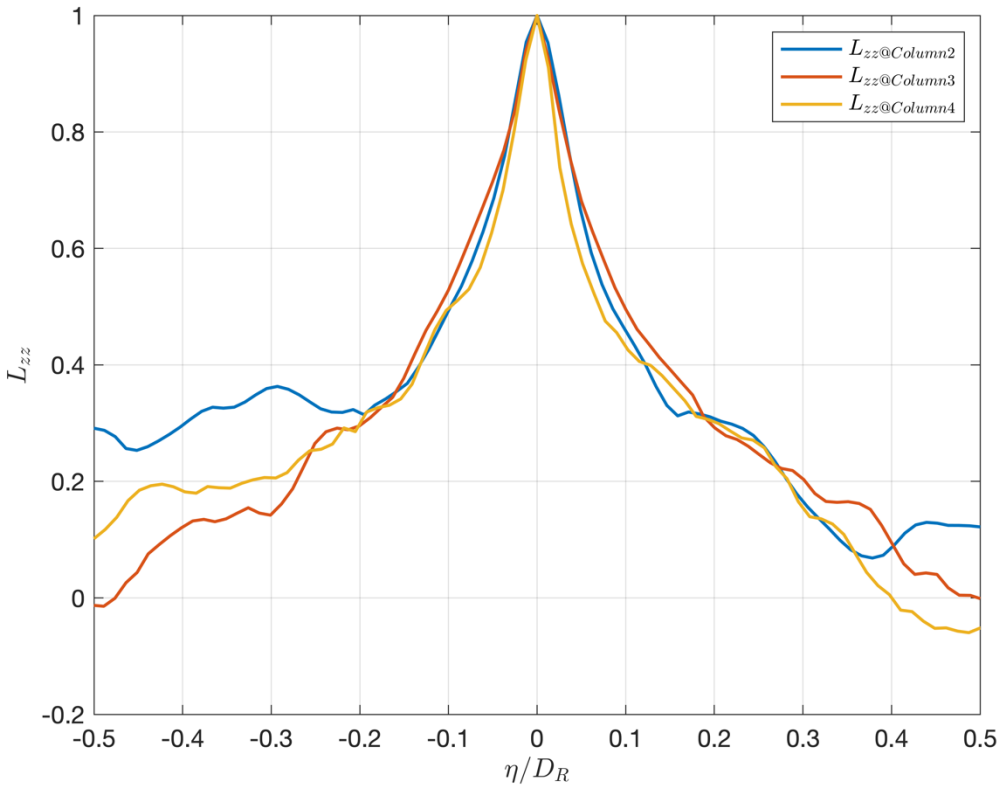

Figure 34: Two-point correlation profiles below the second, third, and fourth tubes at z=0

Two-point correlation was also carried out for selected locations on the first, second, and third sampling lines. Figure 17 shows the two-point correlation profiles at $z = 0$ on each line. One can see that the decay rates of the correlation profiles are close to each other. The integral length scales for the selected points were estimated to be 0.17, 0.16, and 0.13 for points at the first, second, and third sampling lines, respectively. We note that reported integral length scales are normalized with the tube diameter.

4.6. Spectral Analysis

FIV is one of the major concerns in the design of steam generators. Sources of excitation mechanisms of FIV can be classified into four categories: turbulent buffeting, Strouhal periodicity, fluid-elastic instability, and acoustic resonance [9]. The vibration induced by vortex shedding is of practical importance because of its potentially destructive effect on heat exchangers. Many researchers have studied the Strouhal periodicity for symmetric, constant pitch-to-diameter ratio inline and staggered tube banks. To the best of our knowledge, excitation mechanisms of FIV were not studied for variable pitch-to-diameter ratio tube configurations, as we do here.

The most important dimensionless parameter for describing oscillating flow mechanisms is the Strouhal number (St), which links the vortex shedding frequency f with the flow velocity U and with the tube diameter D, as shown here:

$$St = \frac{fD}{U} \ . \tag{14}$$

For relatively simple cases as in flow over a single circular cylinder, the St number is around 0.2 for Reynolds numbers ranging between 500 and 10^5 [34]. However, the vortex-shedding process in tube banks is complex because of the possible tube configurations. Independent variables such as the transverse pitch-to-diameter ratio P_T/D, longitudinal pitch-to-diameter ratio P_L/D, pitch offset P_O/D, and Reynolds number affect the St number. In the present geometry, owing to the oppositely coiled adjacent helical

tubes with fixed transverse spacing, P_T/D is constant whereas P_L/D is varying. This changes the tube configuration in the flow domain along the z-direction.

To obtain the spectral analysis, we utilized a fast Fourier transform (FFT) and the power spectral density (PSD). Applying FFT to a time series leads to a loss of time-dependent information on the signal by providing the representation of the signal in the frequency domain. It is used to identify the dominant frequencies in turbulent flows. In this study, to estimate the power content of a signal at different frequencies, we used Welch's PSD method [35]. Welch's method divides signal into overlapping segments and uses the window function prior to FFT, which reduces the noise in the estimated power spectra.

Figure 34 shows the planes in the HCSG domain and history points on them. To study the flow excitations in the present case, we have history points on three planes separated by 6 degrees, where we record instantaneous velocities at each time step. History points were placed along the main stream in channel 2. The fluctuating part of the transverse velocity was extracted for the FFT analysis. The transverse velocity fluctuation can be associated with the vortex shedding.

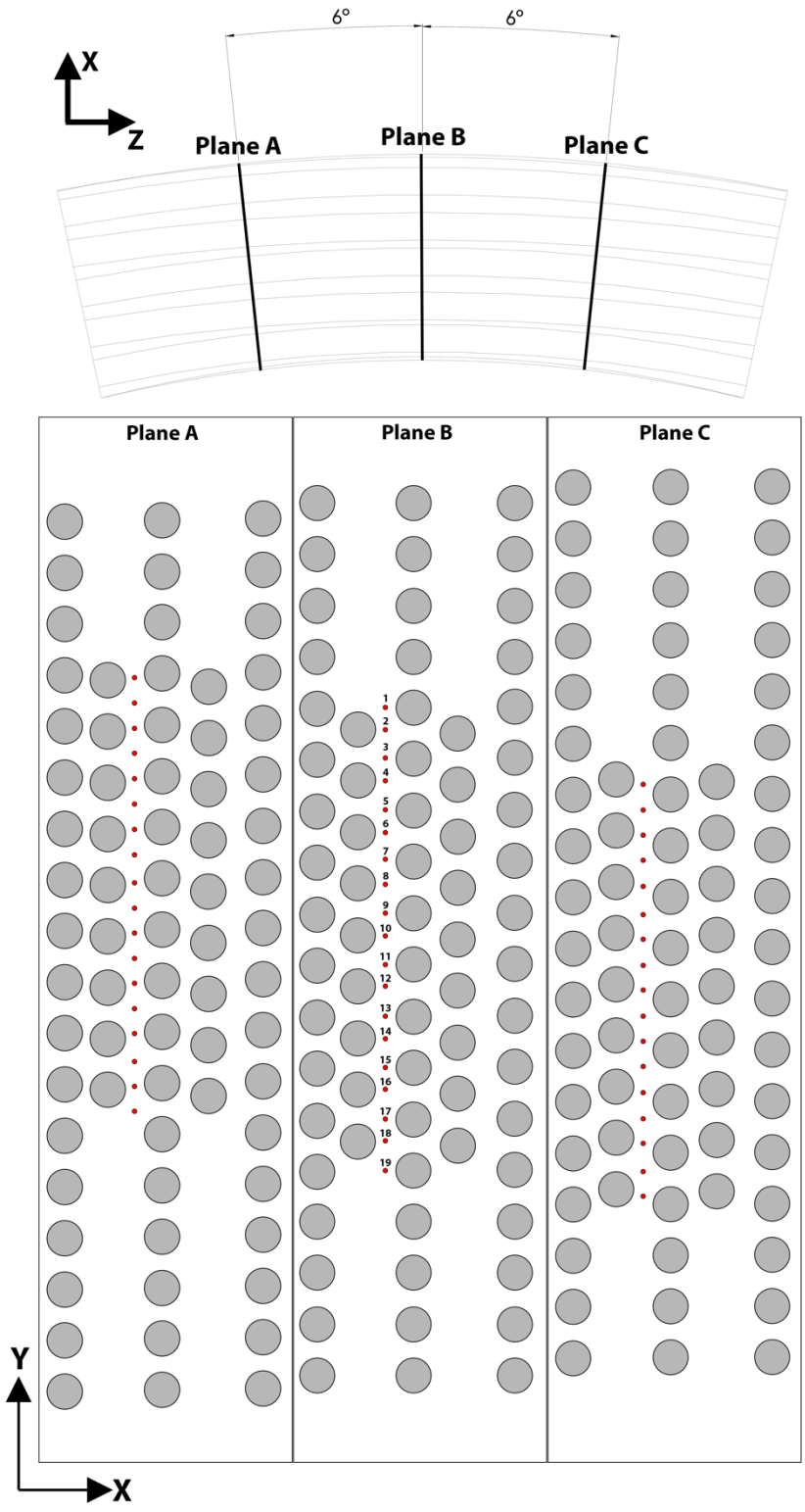

Figure 35: Locations of history points for spectral analysis (reprinted) [23]

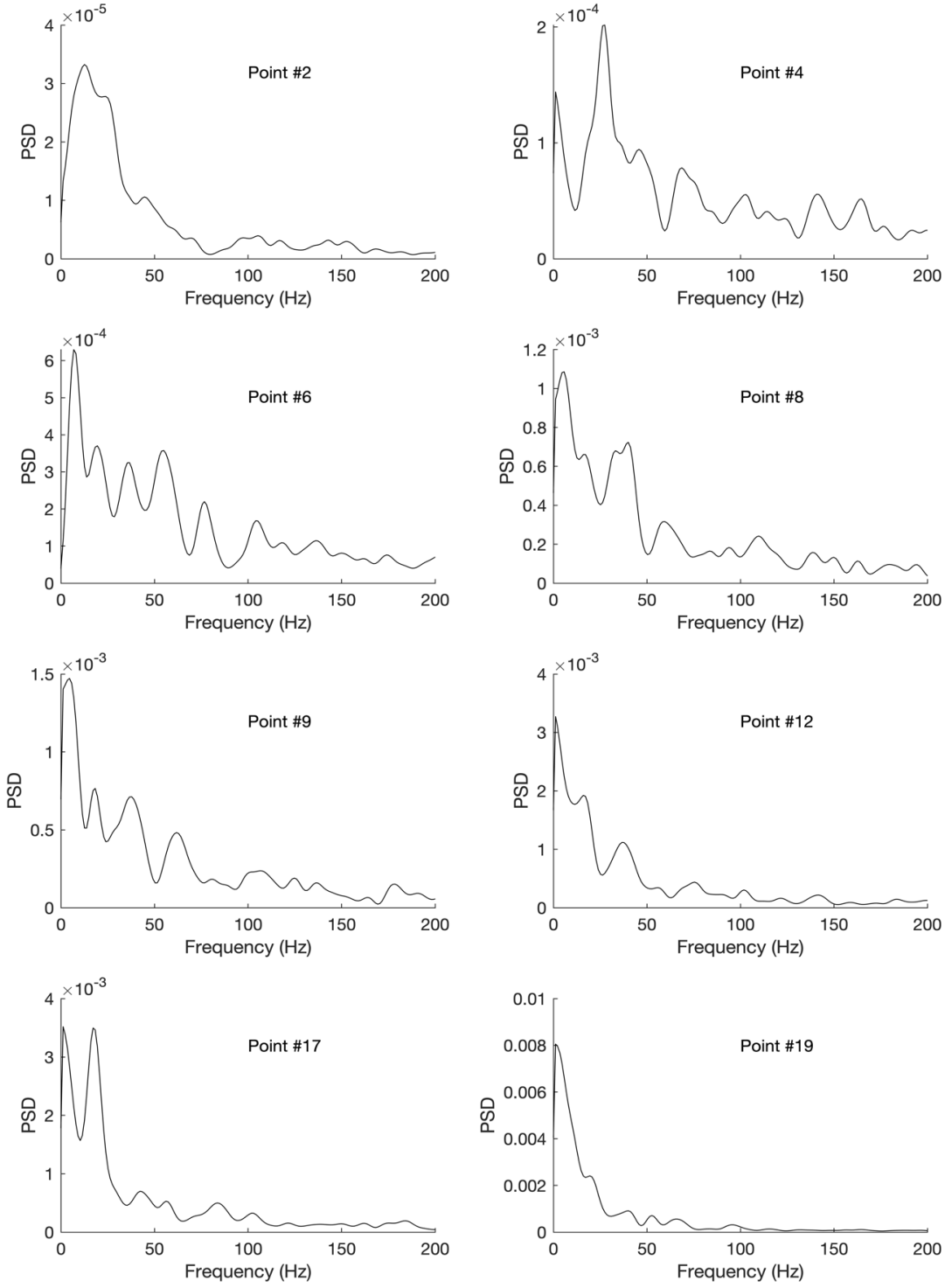

Figure 36: Power spectrum densities along channel 2 at select locations on plane B

In this paper we discuss results obtained from plane B. Figure 35 shows the PSD of the fluctuating velocity components on plane B for select points. Points are labeled on Figure 34. We observe that at the beginning of the channel, fluctuations occur at low frequencies. Farther downstream (in the middle section of the channel) fluctuations occur at a wide range of higher frequencies. Closer to the end of channel, the fluctuation frequency decreases, behavior that can be attributed to collective effect and is consistent with the experimental studies reported in [11,36,37].

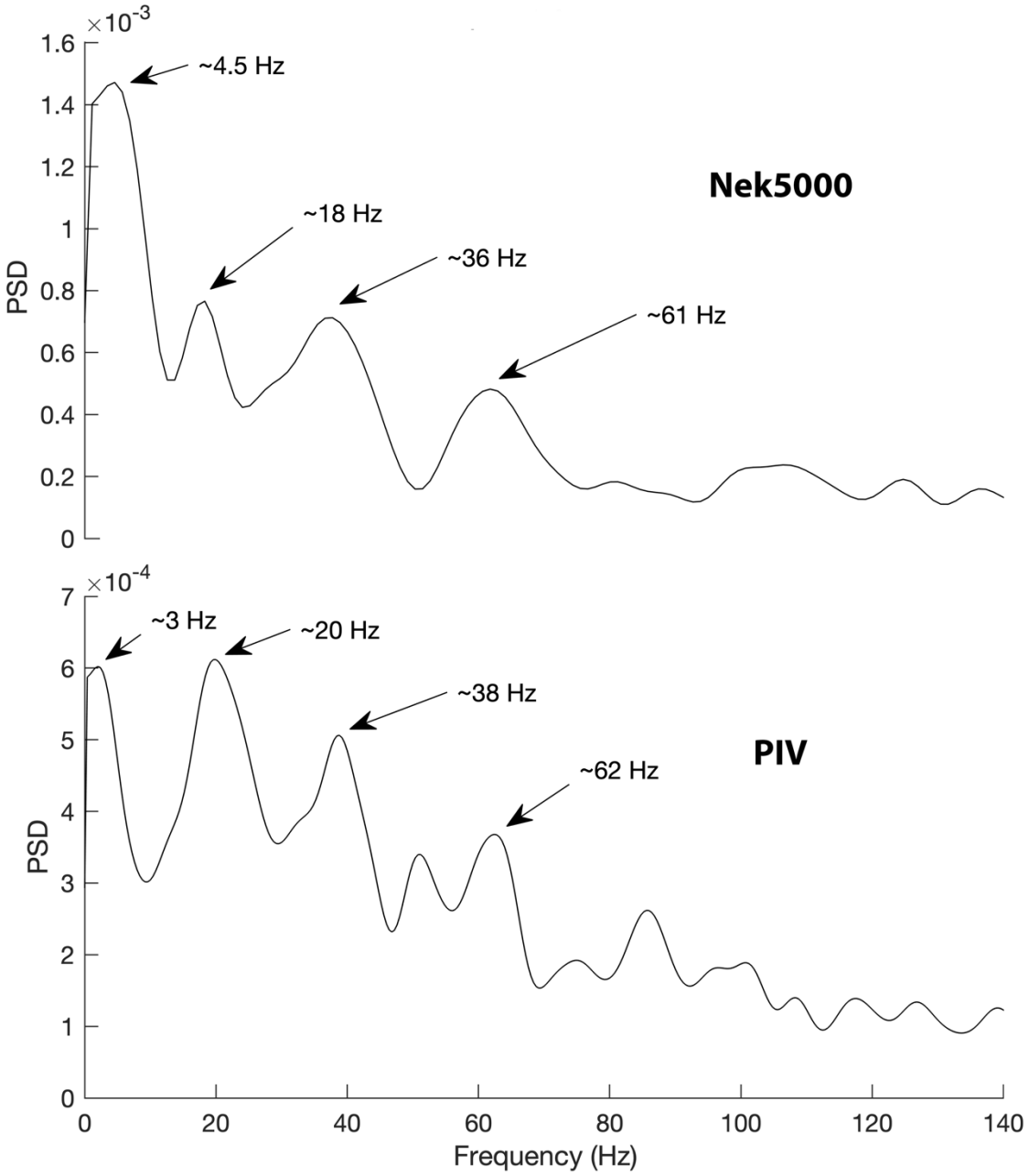

Figure 37: Power spectrum densities at point 9 Nek5000 (top) and PIV (bottom)

In the present study, the power spectrum of fluctuating velocities from the LES calculations was compared with the power spectrum of the PIV data. Instantaneous velocities were extracted from the PIV data at the location corresponding to point 9 shown

in Figure 34. Figure 36 shows the PSDs from the LES (top) and PIV measurements (bottom). The PSD of the LES calculations shows four distinct peaks at ~4.5 Hz, ~18 Hz, ~36 Hz, and ~61 Hz. PIV measurements show five distinct frequency peaks at ~3 Hz, ~20 Hz, ~38 Hz, ~50 Hz, and ~62 Hz. The peak at ~50 Hz in the PIV measurements is due to the centrifugal pump used in the experiments. The other four frequency peaks in the PIV measurements show good correlation with peaks observed in the simulation. The Strouhal numbers were calculated based on these frequencies with gap velocities and upstream inlet velocities. Table 2 summarizes the observed frequencies in both simulation and experiment with corresponding Strouhal numbers. Overall, the observed frequencies from LES and PIV measurements along with corresponding Strouhal numbers are in good agreement.

Table 3: Summary of the observed frequencies in simulation and experiment at corresponding tube row

f_{LES} (Hz)	f_{PIV} (Hz)	$St_{LES,Uinlet}$	$St_{LES,Ugap}$	$St_{PIVUinlet}$	$St_{PIV,Ugap}$
4.5	3	0.13	0.08	0.09	1.17
18	20	0.52	0.34	0.59	0.68
36	38	1.05	0.67	1.06	0.38
61	62	1.78	1.14	1.83	0.06

4.7. Wavelet Analysis

Time signals can be analyzed by applying wavelet transform, which provides accurate time-frequency analysis of the signal. Briefly, wavelet transform can be explained as a combination of Fourier transform and windowed Fourier transform [38].

Two main groups of wavelets are used for the analysis: continuous wavelets and orthogonal wavelets. The choice of the analyzing wavelet is important since it affects the information extracted from the data. Use of orthogonal wavelets is better for synthesis and data compression, whereas continuous wavelets are better for scale analysis [38]. The wavelet transform of the signal is essentially a cross-correlation of the signal with the mother wavelet at different scales. The resultant wavelet coefficients show the degree of correlation between the wavelet and the signal at a certain scale. High wavelet coefficients indicate that the wavelet function and signal show similarities. Extracted signal characteristics is affected by the applied mother wavelet. Hence, selection of the mother wavelet plays important role in wavelet analysis. Two main wavelets are employed in the field of turbulent flows: Mexican hat and Morlet wavelets [39]. In this paper a continuous real-valued Morlet wavelet was utilized for the analysis of the time signal of the fluctuating velocity, which is given by [40]

$$\Psi(t) = e^{-x^2} cos(5x) \tag{15}$$

Wavelet analysis was carried out at the location of point 9 shown in Figure 34. This is the location where the power spectrum of the fluctuating velocity component from

Nek5000 was compared with the power spectrum of the PIV measurements. In the analysis, the length of the time signal from Nek5000 was 150,000 data points with 171 kHz sampling frequency, which corresponds to approximately 0.9 seconds. The length of data from the PIV measurements was 10,800 data points with 4 kHz sampling frequency (frequency of the PIV camera), which corresponds to 2.7 seconds. We presented 0.9 second section of the PIV data spectrogram, which is equal to the length of the simulation data.

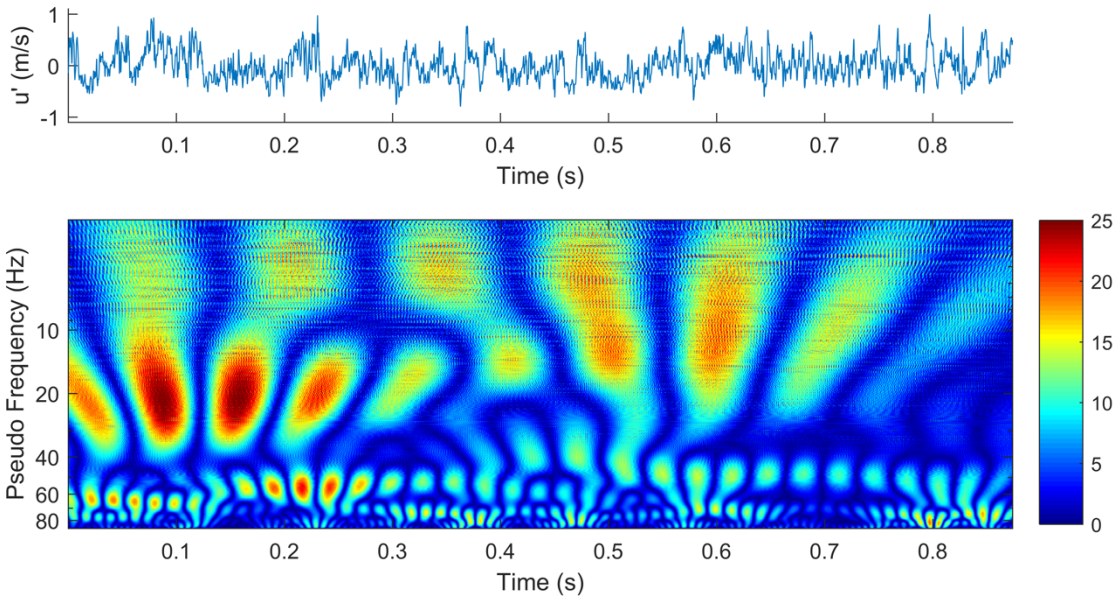

Figure 38: Fluctuating spanwise velocity from LES calculation at point 9 (top) with corresponding wavelet spectrogram (bottom)

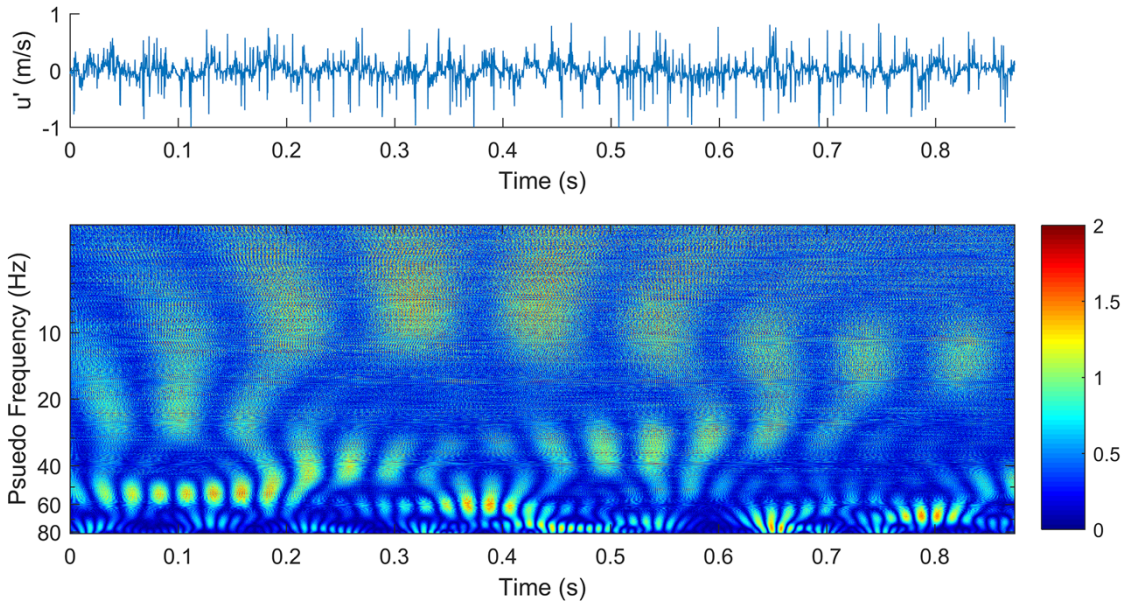

Figure 39: Fluctuating spanwise velocity from PIV measurements near point 9 (top) with corresponding wavelet spectrogram (bottom)

Figure 37 shows the fluctuating velocity component from the LES calculations with the wavelet energy spectrogram in which the frequency range extends from ~3 Hz to 80 Hz. Figure 38 shows the fluctuating velocity component from the PIV measurements with the wavelet energy spectrogram for the same frequency range. In both velocity signals, the frequency range extends to higher values; however, the spectrogram focuses on the range of frequencies where the dominant frequencies were observed in the spectral analysis. The bright color in the spectrogram shows high magnitude of the wavelet energy, whereas the opposite applies for the dark color. Also, the wide spectrogram band along the time axis indicates the presence of large coherent structures [41].

Overall, one can see that the red zones in both spectrograms reveal dominant frequencies similar to those observed in power spectrum densities. The wavelet spectrogram in Figure 37 shows three dominant frequency ranges where coherent structures exist. Large-scale turbulent structures exist in the range between 3 Hz and 7 Hz, medium-scale structures exist between 10 Hz and 40 Hz, and small-scale structures exist in the range between 45 Hz and 70 Hz. The medium-scale and large-scale turbulent structures show higher wavelet energy content compared with the small-scale structures. As the frequency increases, the number of bright and dark streaks increases, and the streaks become narrower. This shows the energy cascade evolution of large-scale turbulent structures breaking down into small-scale structures. The wavelet spectrogram in Figure 38 shows large-scale turbulent structures between 3 Hz and 15 Hz, medium-scale structures between 20 Hz and 40 Hz, and small-scale structures between 45 Hz and 70 Hz. From comparison of two spectrograms one can see that the spectrogram of the LES calculations shows higher wavelet energies compared with the spectrogram from the PIV measurements. This is due to the sampling frequency of the signal, which is four times greater for the LES calculations than for the PIV measurements.

4.8. Proper orthogonal decomposition (POD) analysis

In this section, we discuss flow analysis using proper orthogonal decomposition (POD) of velocity snapshots to extract the dominant flow structures. Velocity snapshots from the LES calculation were recorded at the PIV window, which was shown in Fig. 17.

POD is a powerful and elegant method of data analysis. It was first introduced into the study of turbulent flows by Lumley [21]. In other disciplines, it is known as principal component analysis, singular value decomposition, and Karhunen-Loeve decomposition. Applications of POD can be found in various disciplines other than fluid mechanics. Sirovich extended the work of Lumley and introduced the method of snapshots, which increased the computational efficiency of the POD analysis [42]. The purpose in POD applications is to extract dominant features and trends in experimental data and numerical simulations. In the context of turbulence, these will be patterns in space and time.

In the present study, we use the method of snapshots for calculating POD. A detailed review and analysis of POD methods can be found in [43,44]. Here we give a brief review of the method. The fundamental idea behind the POD is to decompose a given N-dimensional data into a set of spatially orthogonal modes and a set of temporal coefficients to represent it as a finite sum in a variable-separated form as follows:

$$u(x) \cong \sum_{i=1}^{N} a_i^n \phi^i \ , \tag{16}$$

where N is the number of velocity snapshots, a_i are POD temporal coefficients, and $\phi(x)$ are POD basis functions.

As a first step in applying POD to fluid flow, we subtract the temporal mean $\bar{u}(x)$ from the instantaneous velocity field $u(x,t)$:

$$u'(x,t) = u(x,t) - \bar{u}(x)\,. \tag{17}$$

Fluctuating velocity components (u', v') from a single time step are arranged in single column. The solution of the eigenvalue problem is ordered based on the size of the eigenvalues, which ensures that the most energetic modes are the primary modes. POD modes can be reconstructed based on the eigenvectors as follows:

$$\phi^i = \frac{\sum_{n=1}^{N} A_n^i u^n}{\left\| \sum_{n=1}^{N} A_n^i u^n \right\|}, \qquad i = 1, \ldots, N\,. \tag{18}$$

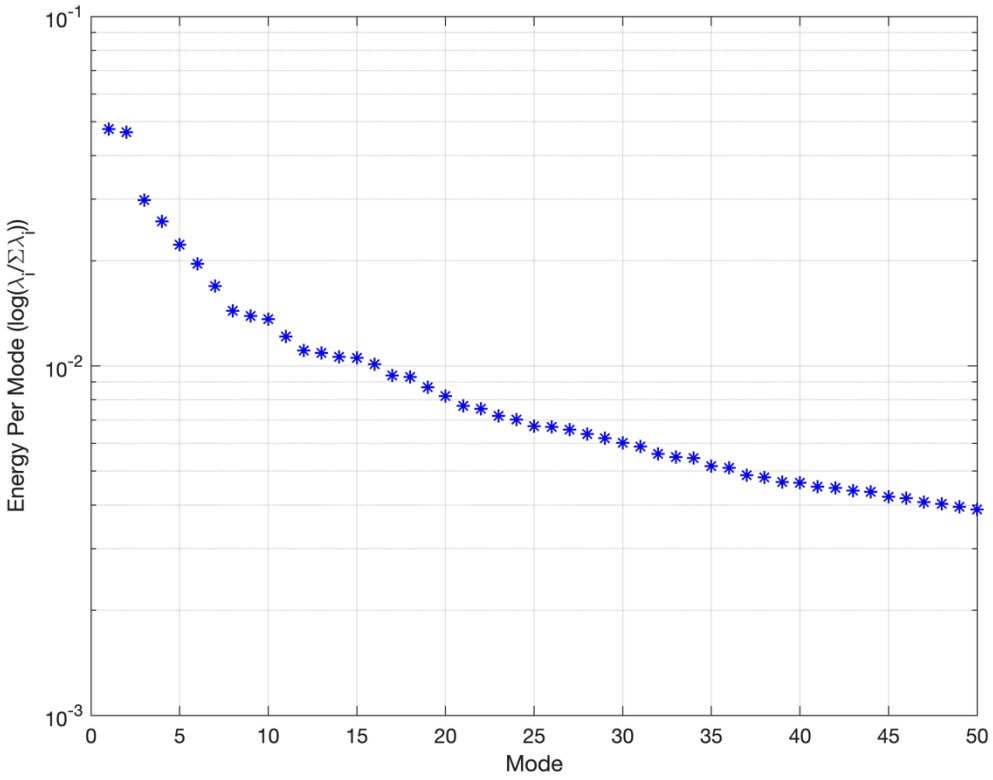

Figure 40: Energy distribution per mode

In the present study, the POD of the LES calculations was carried out with 1,000 snapshots. The snapshot frequency for LES was 1,700 snapshots per second. Figure 39 shows the energy distribution for each mode in the first 50 modes. The first and second modes have a close energy content.

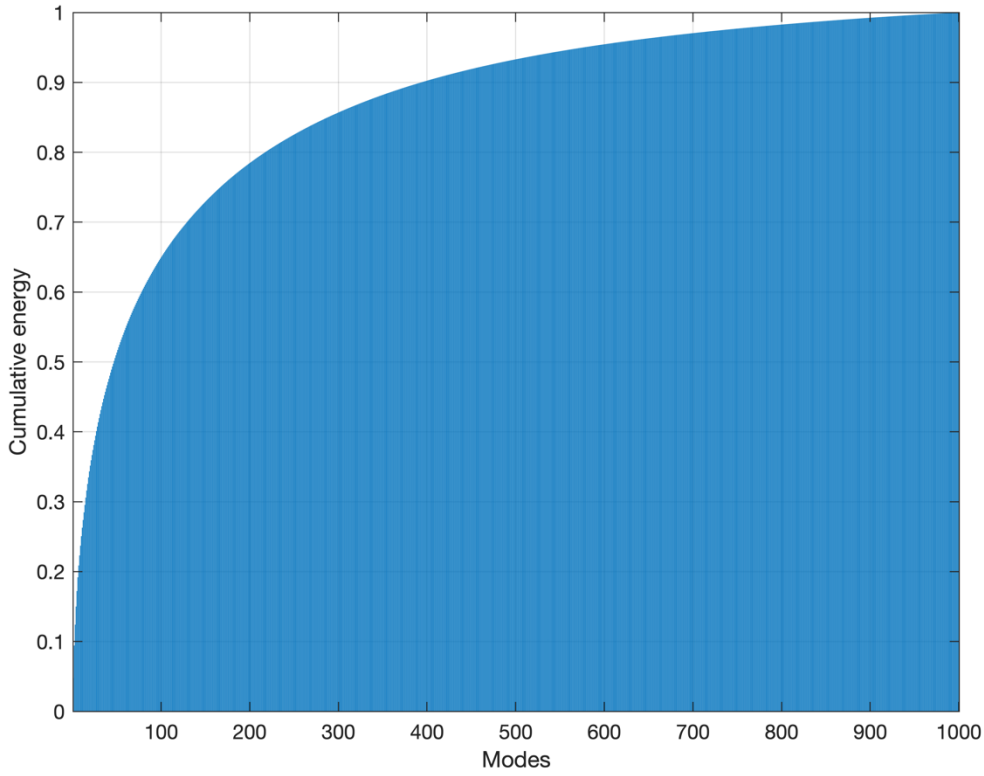

Figure 41: Cumulative energy

Figure 40 shows the cumulative energy. From the cumulative energy, one can see that 50% of the turbulent kinetic energy (TKE) can be captured with the first 46 modes and 90% with the first 400 modes.

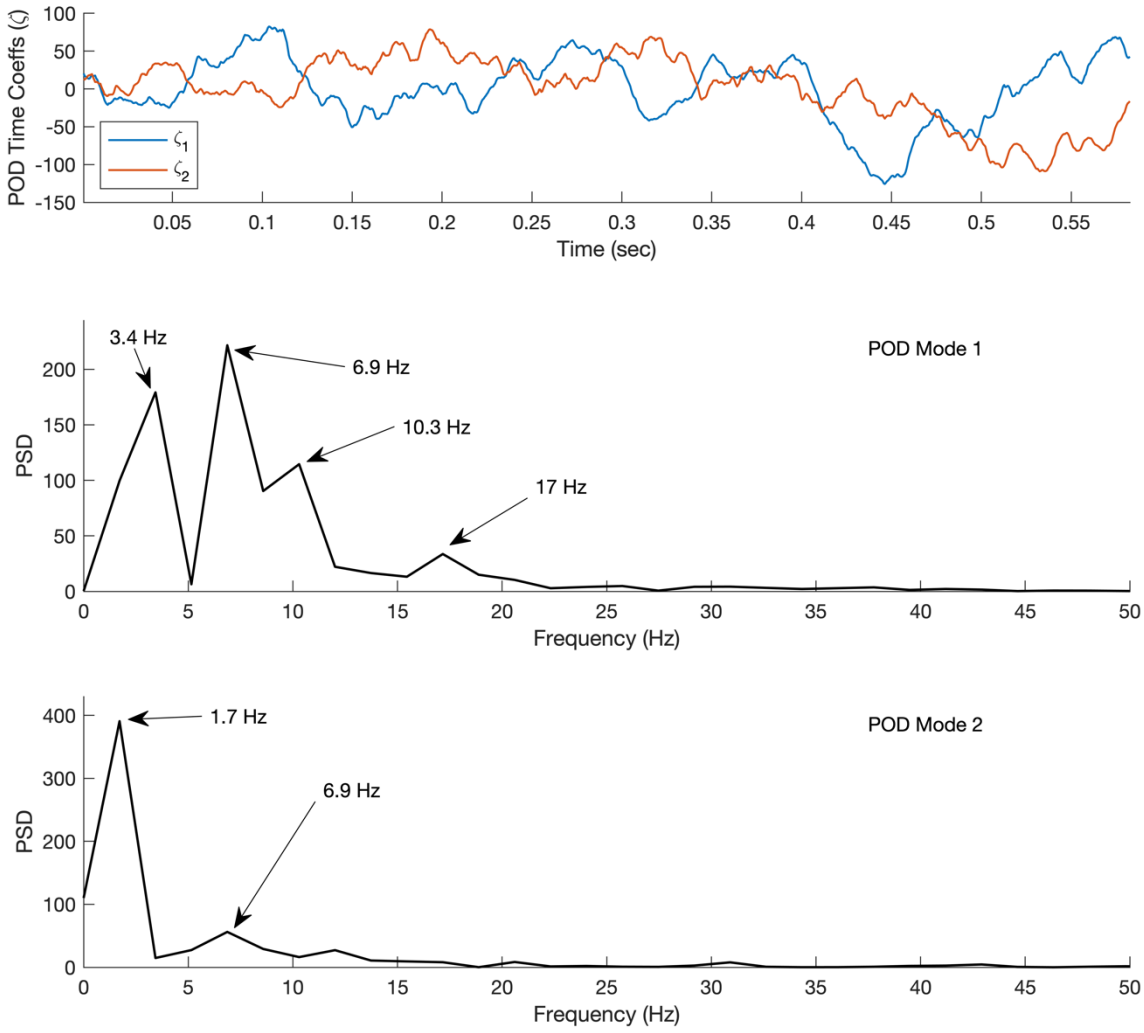

Figure 42: POD temporal coefficients for mode 1 and mode 2 (top), PSD of POD mode 1 temporal coefficients (middle), PSD of POD mode 2 temporal coefficients (bottom)

Figure 41 (top) shows the POD coefficients for the first and second modes. The POD temporal coefficients do not show any distinguishable trend. In order to analyze temporal coefficients and determine the behavior of the POD modes, FFT was applied to the first- and second-mode temporal coefficients (Figure 41, middle and bottom, respectively). From the power spectrum of the first mode, one can see that the most

energetic POD modes are evolving in four distinct frequencies. The most dominant frequency in the first mode is 6.9 Hz. The FFT of the second mode shows single dominant frequency, which is half of the smallest dominant frequency of the first mode. However, one can still see a peak at 6.9 Hz in the FFT of the second mode, which is the most dominant frequency of first mode. This can indicate that the first and second modes represent similar physics. One may recall that two peaks were observed at ~4.5 Hz and ~18 Hz in the spectral analysis of the velocity fluctuations at point 9 (Figure 34), which seem to be related with the observed frequency peaks in the spectral analysis of the POD time coefficients at ~3.4Hz, ~6.9 Hz, and ~17 Hz.

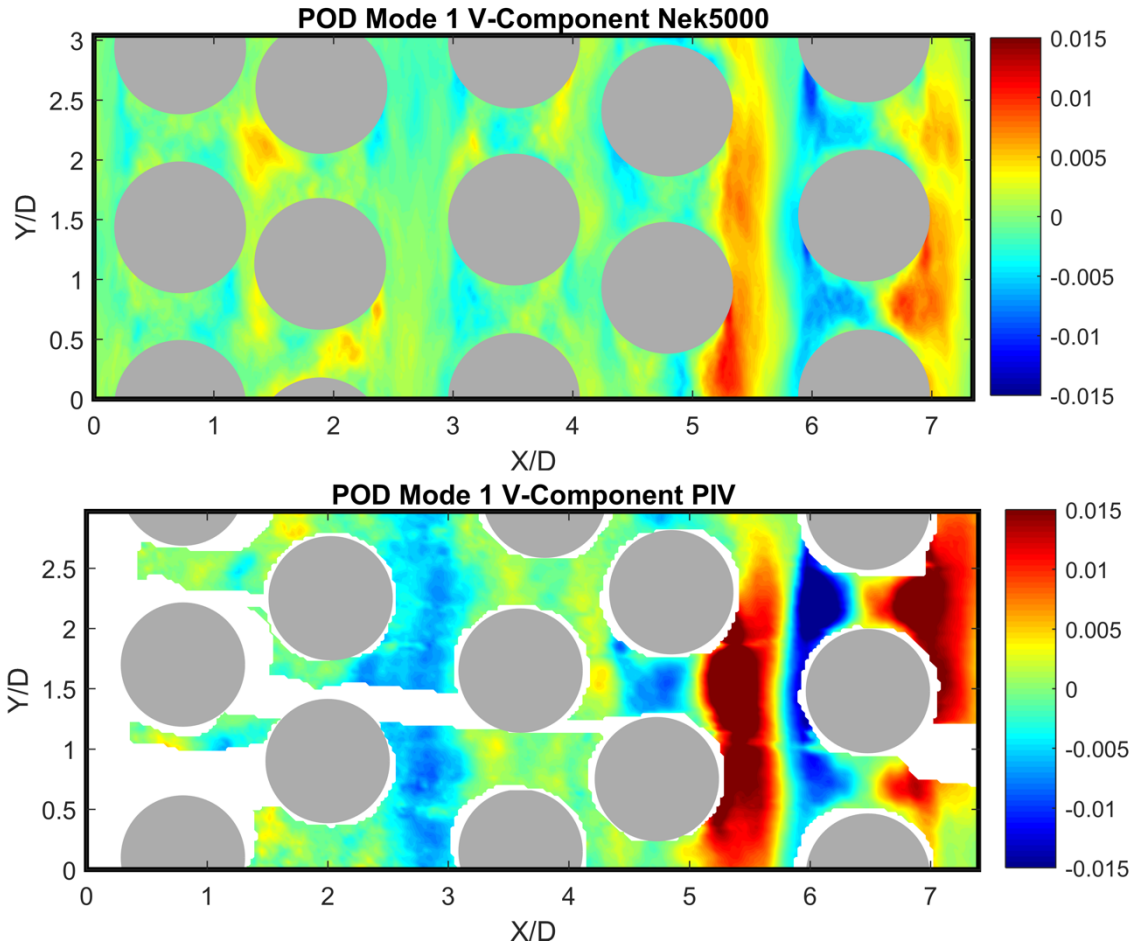

Figure 43: POD mode 1 - Streamwise velocity component: Nek5000 (top) and PIV (bottom)

POD was conducted on the PIV data with 5,400 snapshots, in order to compare flow structures captured between LES and PIV. Snapshot frequency for the PIV images was 2000 snapshots per second. Figure 42 shows the first POD mode for the streamwise component and Fig. 43 shows the first POD mode for the transverse component of the velocity fluctuations for LES (top) and PIV (bottom), respectively.

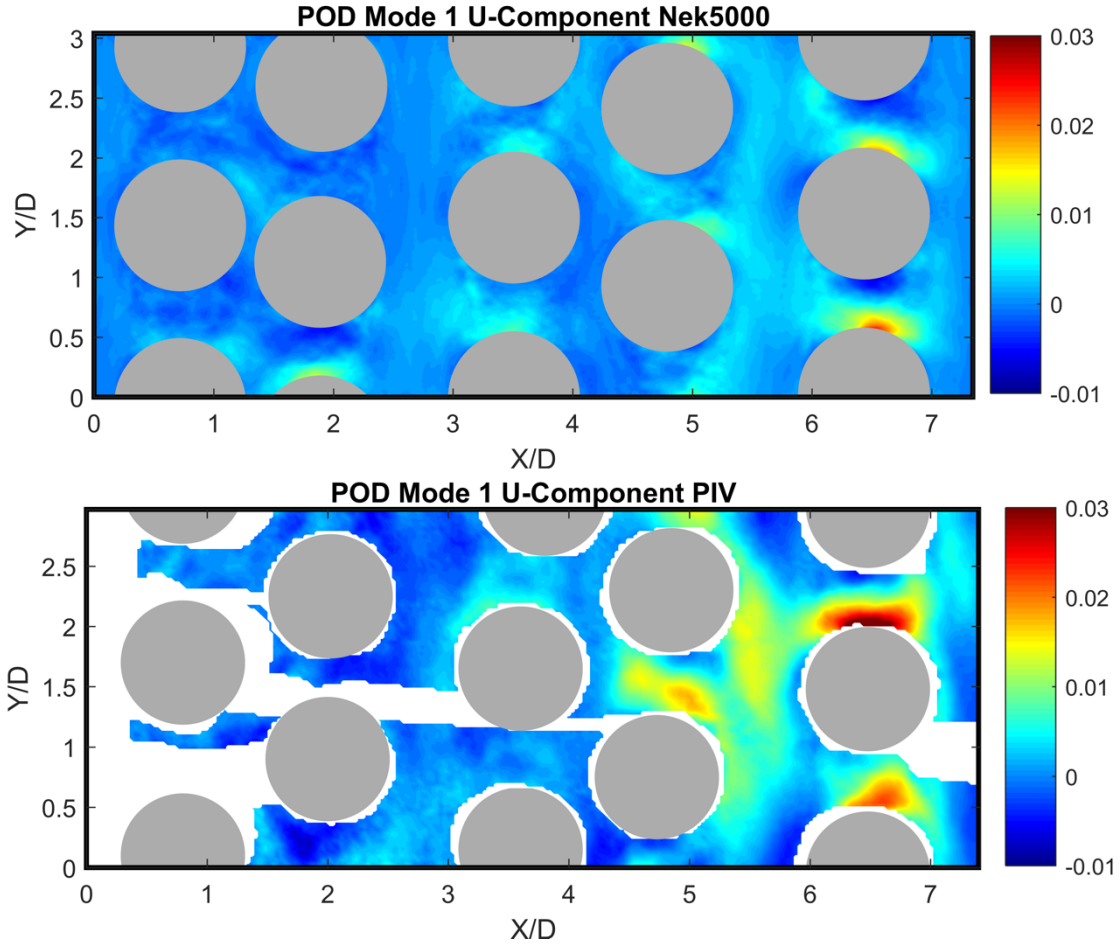

Figure 44: POD mode 1 - Spanwise velocity component: Nek5000 (top) and PIV (bottom)

In the streamwise direction, the first mode shows dominant structures along channel 4 and in the wake of the tubes. In the spanwise direction, as in the streamwise direction, the first mode shows flow structures in channel 4 and dominant counterflowing structures in the wakes of the tubes in the fifth column. The second POD mode in the streamwise direction shows flow structures similar to those of the first mode but reveals more dominant flow structures in the central region of the tube bundle. A strong resemblance exists between POD modes 1 and 2 in the streamwise direction especially in

channel 4. This relation between modes means that the two most energetic modes correspond to advection of a flow structure [45].

In the spanwise direction, second POD mode as in the first mode shows counter flow in the wake region of tubes at the central region of the tube bundle.

In the present POD analysis, first and second POD modes in the spanwise direction reveal high counter flow and mixing of flow between channels, which is consistent with findings of Yuan et al. [18] and Yildiz et al. [20]. Analysis of the flow in the simplified HCSG did not reveal such a mixing between channels [19].

Comparison of the first and second POD modes from LES with PIV show similar structures. As a general trend, the POD modes obtained from PIV images show flow structures more dominant than the POD modes obtained from the LES calculations. These might be due to more revealed flow structures in LES compared with the PIV data. Comparison of higher modes between LES and PIV showed greater discrepancies. We note that the PIV data is two dimensional. Overall, the POD analysis of the flow in HCSGs helped further our understanding of the evolution of the flow structures and mixing between channels.

4.9. Dynamic Mode Decomposition (DMD)

In the study of fluid dynamics, in order to identify spatio-temporal coherent structures from high-dimensional data, Schmid developed dynamic mode decomposition [46]. DMD was developed based on proper orthogonal decomposition, which utilizes the computational efficiency of singular value decomposition (SVD). POD analysis provides results in a hierarchy of modes based on spatial correlation and energy, where DMD provides a modal decomposition where each mode consists of spatially correlated structures with same linear behavior in time [47].

Today, DMD has become one of the main tools for the data-driven characterization of high-dimensional systems. The DMD algorithm can be seen as the connection of POD/SVD for spatial dimensionality and the Fast-Fourier Transform (FFT) for temporal frequency analysis. Each DMD mode is associated with a complex eigenvalue, where the real part of the eigenvalue represents the growth or decay rate and the complex part represents the oscillation frequency.

In the present study we use the exact DMD algorithm developed by Tu et al [48]. As in Schmid's original algorithm, this algorithm is based on the efficient singular value decomposition. The original DMD algorithm developed by Schmid required uniform sampling of the dynamics in time, where Tu et al. expanded this algorithm for the non-uniformly collected data.

First step in DMD is to collect snapshots of the state of a system as it evolves in time. Timestep between the snapshots has an important role such that it determines the

frequencies that can be resolved with DMD analysis. Collected snapshots are then arranged into column matrices X and Y as follows:

$$\mathrm{X} = \begin{bmatrix} \mathrm{x}_1^1 & \mathrm{x}_1^2 & \cdots & \mathrm{x}_1^{m-1} \\ \mathrm{x}_2^1 & \mathrm{x}_2^2 & \cdots & \mathrm{x}_2^{m-1} \\ \vdots & \vdots & \vdots & \vdots \\ \mathrm{x}_n^1 & \mathrm{x}_n^2 & \ldots & \mathrm{x}_n^{m-1} \end{bmatrix} \tag{20a}$$

$$\mathrm{Y} = \begin{bmatrix} \mathrm{x}_1^2 & \mathrm{x}_1^3 & \cdots & \mathrm{x}_1^m \\ \mathrm{x}_2^2 & \mathrm{x}_2^3 & \cdots & \mathrm{x}_2^m \\ \vdots & \vdots & \vdots & \vdots \\ \mathrm{x}_n^2 & \mathrm{x}_n^3 & \ldots & \mathrm{x}_n^m \end{bmatrix} \tag{20b}$$

where columns of the matrices are time snapshots and rows are the locations of the measurement.

For the arranged dataset in Eq. 20, define the operator A, which is the best-fit linear operator that relates the two snapshot matrices in time:

$$\mathrm{Y} \approx \mathrm{AX}. \tag{21}$$

Compute the singular value decomposition of X:

$$\mathrm{X}=\mathrm{U}\Sigma V^* \tag{21}$$

Compute the full matrix A, which can be obtained by computing the pseudo-inverse of X:

$$A=U^{*}YV\Sigma^{-1} \tag{22}$$

Compute the eigenvalues and eigenvectors of A:

$$Aw = \lambda w \tag{23}$$

where each nonzero eigenvalue of λ is a DMD eigenvalue, which are also eigenvalues of the matrix A.

The DMD modes are reconstructed using the eigenvectors w of the reduced system and the time-shifted snapshot matrix Y following:

$$\Phi=YV\Sigma^{-1} \tag{24}$$

These DMD modes are the eigenvectors of the matrix A corresponding to the eigenvalues in λ. More details of this algorithm (exact DMD) along with differences with original Schmid DMD method can be found in [47,48].

4.9.1. Multi-resolution dynamic mode decomposition (mrDMD)

The multi-resolution dynamic mode decomposition (mrDMD) approach is a recursive computation of DMD to remove low-frequency, or slowly varying features from a given collection of snapshots [49]. Figure 44 shows the illustration of the mrDMD process.

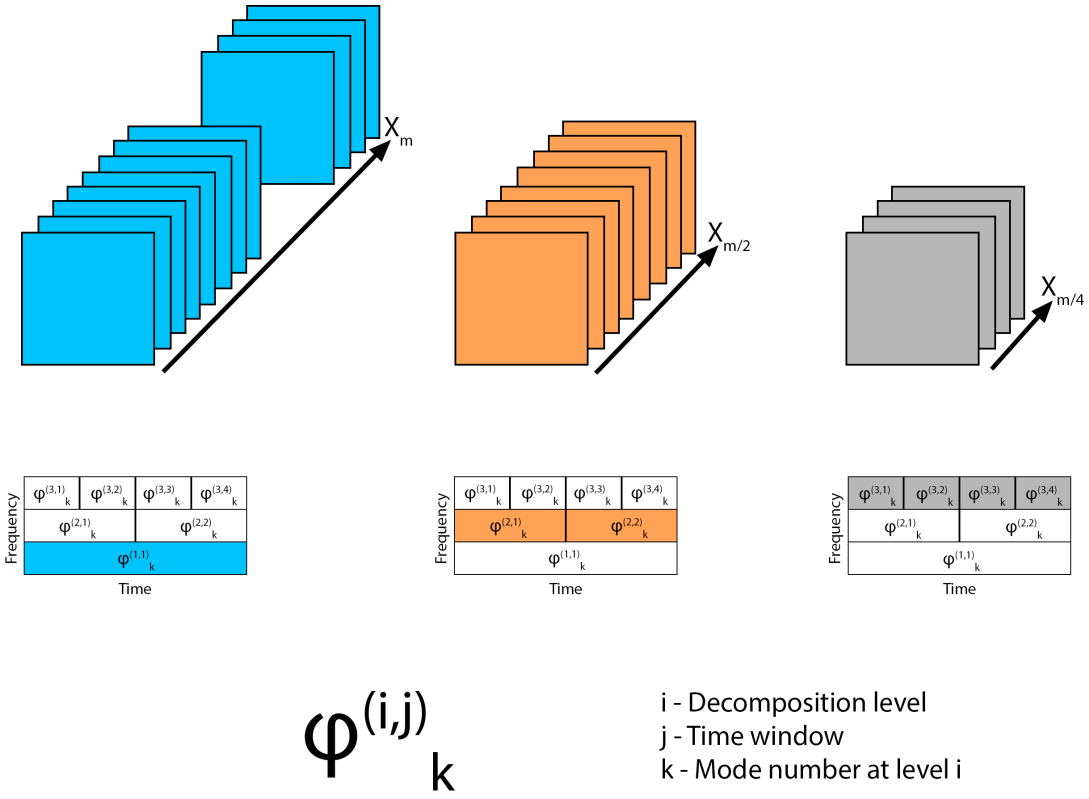

Figure 45: Illustration of mrDMD approach

In DMD approach, it is very important to choose the number of total snapshots (m) such that all high- and low-frequency content is present in the observed dynamics. In mrDMD approach, total number of snapshots is chosen such that to remove the lowest-frequency modes. The slowest modes are removed at each resolution level and the time domain is divided into two segments with equal number of snapshots and DMD is performed once again on each snapshot segments. This recursive process continues until the desired frequency dynamics captured.

In the present study, the mrDMD of the LES calculations was carried out with 1,700 snapshots. The snapshot frequency for LES was ~700 snapshots per second.

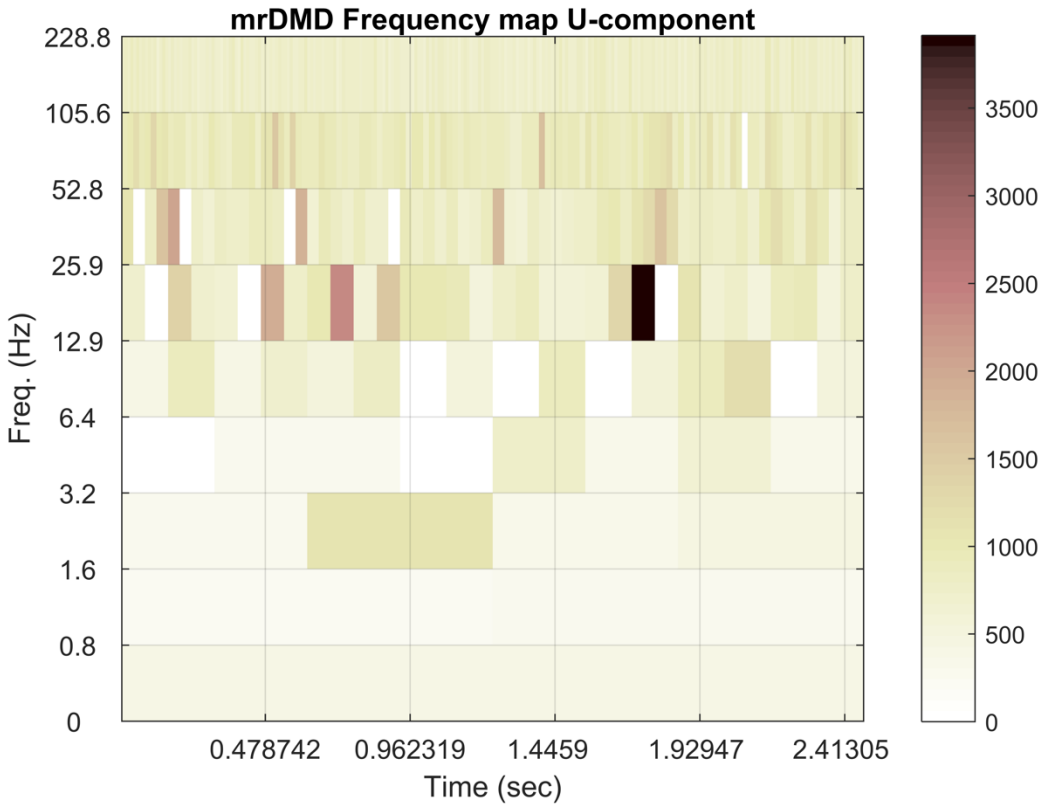

Figure 46: mrDMD Frequency map of the velocity U-component

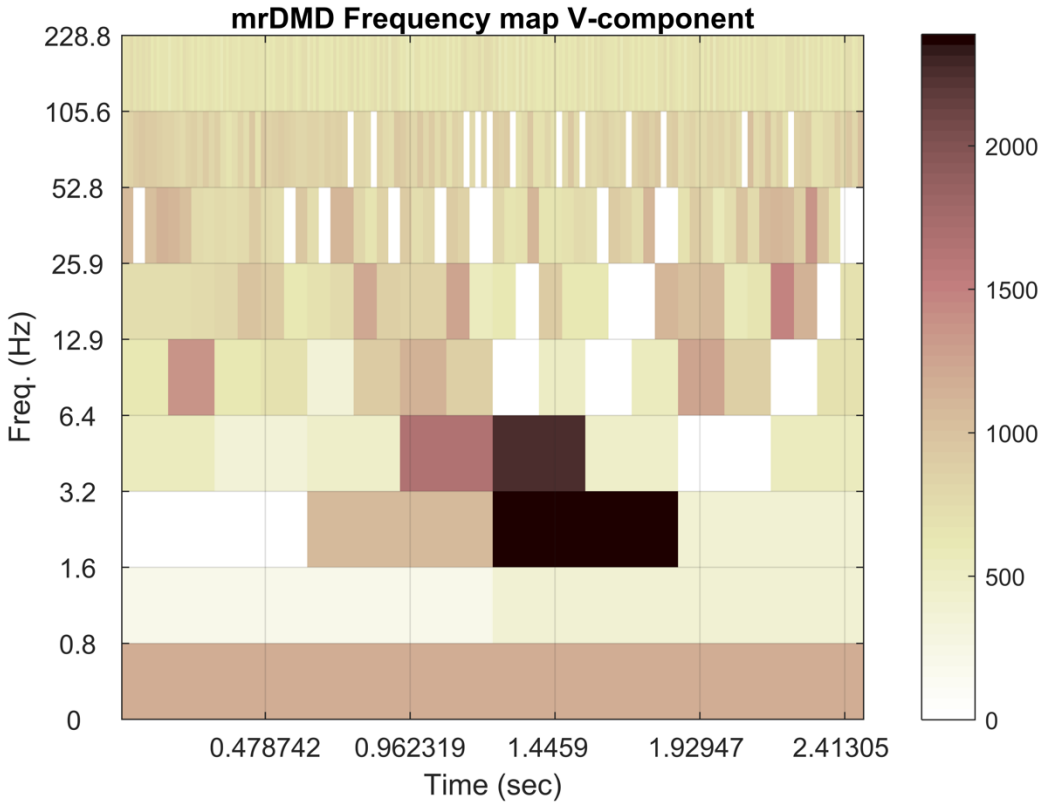

Figure 47: mrDMD Frequency map of the velocity V-component

Figure 45 shows the frequency map as a wavelet-inspired view of the multiresolution structures present in x-component (transverse) of the velocity. It can be seen that the DMD mode amplitudes in x-direction are mostly uniform. At sixth decomposition level DMD mode amplitude shows a peak. This indicates that the time course of the mode matches well with the halving windows of the mrDMD algorithm.

Figure 46 shows the frequency map as a wavelet-inspired view of the multiresolution structures present in the y-component (streamwise) of the velocity. In the streamwise direction, mrDMD modes show more distributed DMD mode amplitudes among the decomposition levels. Also, note that where the time course of the mode does

not match well with the halving windows of the algorithm, the ability of the algorithm to estimate the mode amplitudes is poor (as it can be seen in white spots in Figure 46). This behavior of the algorithm is due to its similarity with Gabor transformation in splitting the time windows.

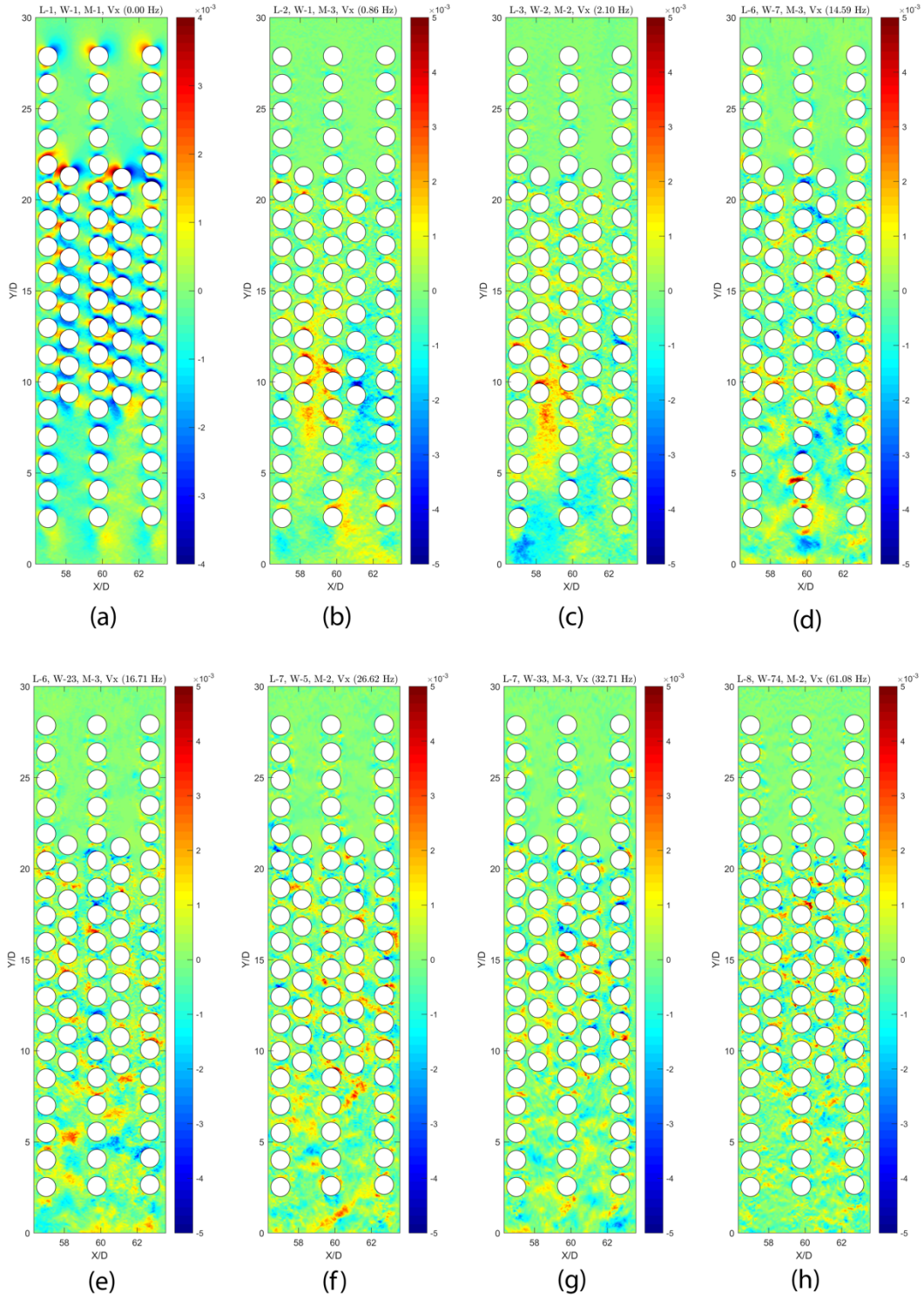

Figure 48: mrDMD modes U-Component

Figure 48 shows the DMD modes of the velocity in x-direction. In the first level of decomposition the extracted mode (Fig. 48 (a)) depicts the zero mode. It should be noted that the $\omega=0$ mode component of level 1 decomposition corresponds to the average velocity in x-direction over the entire simulation data. At level 2 and level 3 decomposition, slowest modes are depicted in Figures 48 (b) and 48 (c) with $\omega=0.86$ and $\omega=2.1$, respectively. These two modes show the flow structures closer to the end of the channel, where the highest secondary-flow intensities present. In the higher decomposition levels (Fig. 48 (d-f)), it can be seen that the flow structures are more spread throughout the channel. Also, at higher decomposition levels, slowest modes that could be extracted with mrDMD has higher frequencies (ω).

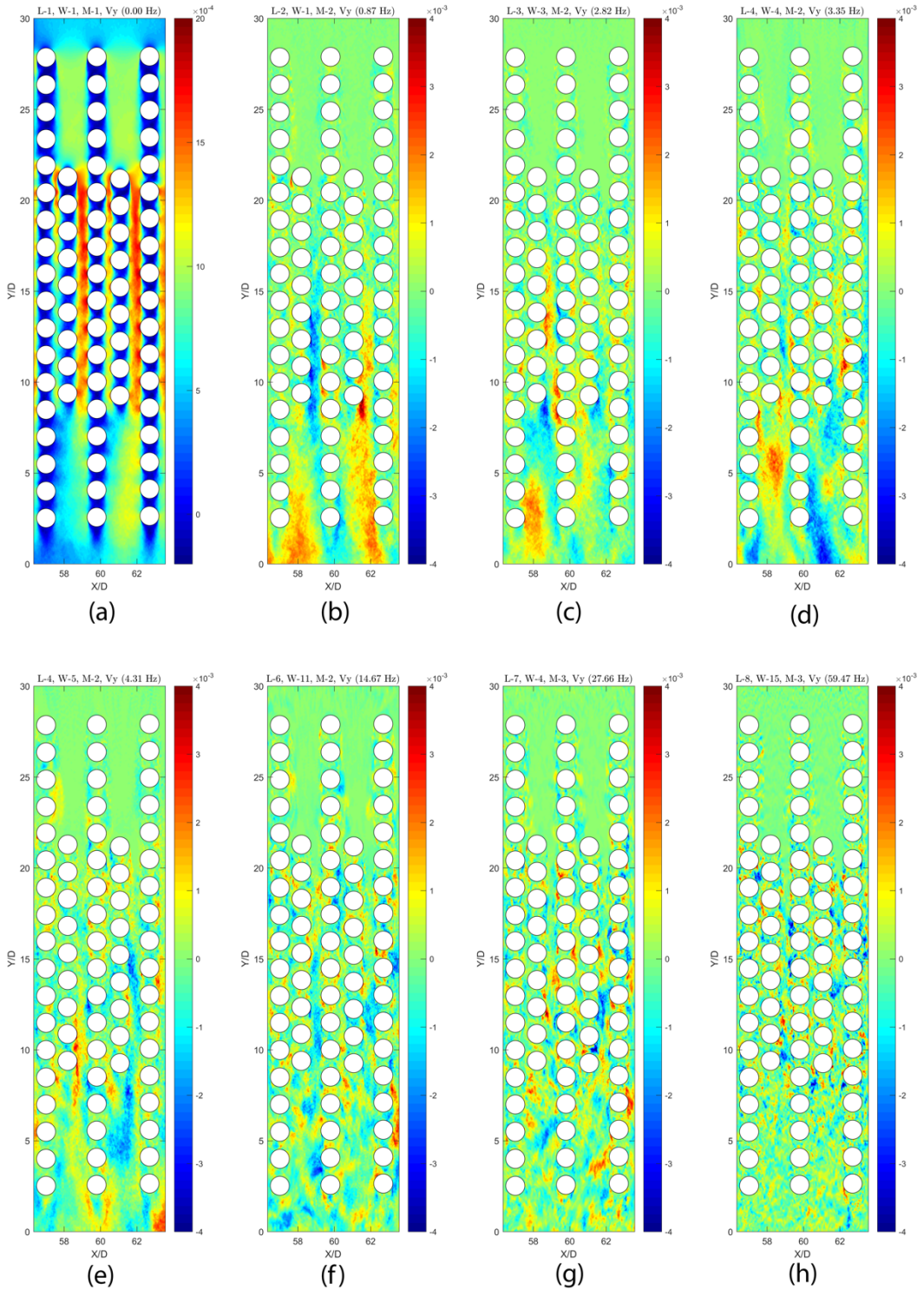

Figure 49: mrDMD modes V-Component

Figure 49 shows the DMD modes extracted of the velocity in y-direction. Figure 49 (a) shows the average velocity in y-direction, which corresponds to zero mode (ω=0) of the first decomposition level. The slowest mode at the second decomposition level (Figure 48 (b)) show the dominant flow structures beginning from the center of the channels at approximately tenth tube row. It is important to note that this behavior was also captured with the integral length scales (see Figure 33), where the integral length scales of the turbulent eddies throughout the domain started to increase and at the end of the channel it reached maximum. At decomposition levels 3 and 4 the frequencies (ω) of the slowest modes increase to 2.82, 3.35, and 4.31 as depicted in Figure 48 (c-e), respectively. Coherent structures in decomposition levels 3 and 4 starts to be observed at a higher location throughout the channel and they are smaller in size and more discrete compared to level 2 decomposition. Figure 49 (f-h) depict modes at decomposition levels 6, 7, and 8, respectively. At these decomposition levels, the slowest modes have frequencies 14.67 Hz, 27.66 Hz, and 59.47 Hz, respectively. It can be seen that as the frequency of the mode increase, coherent structures extracted in the modes become smaller and become more uniformly distributed throughout the channel. This is an expected outcome, which was also observed in the spectral analysis of the velocity signals throughout the domain.

4.10. Visualization of Coherent Structures

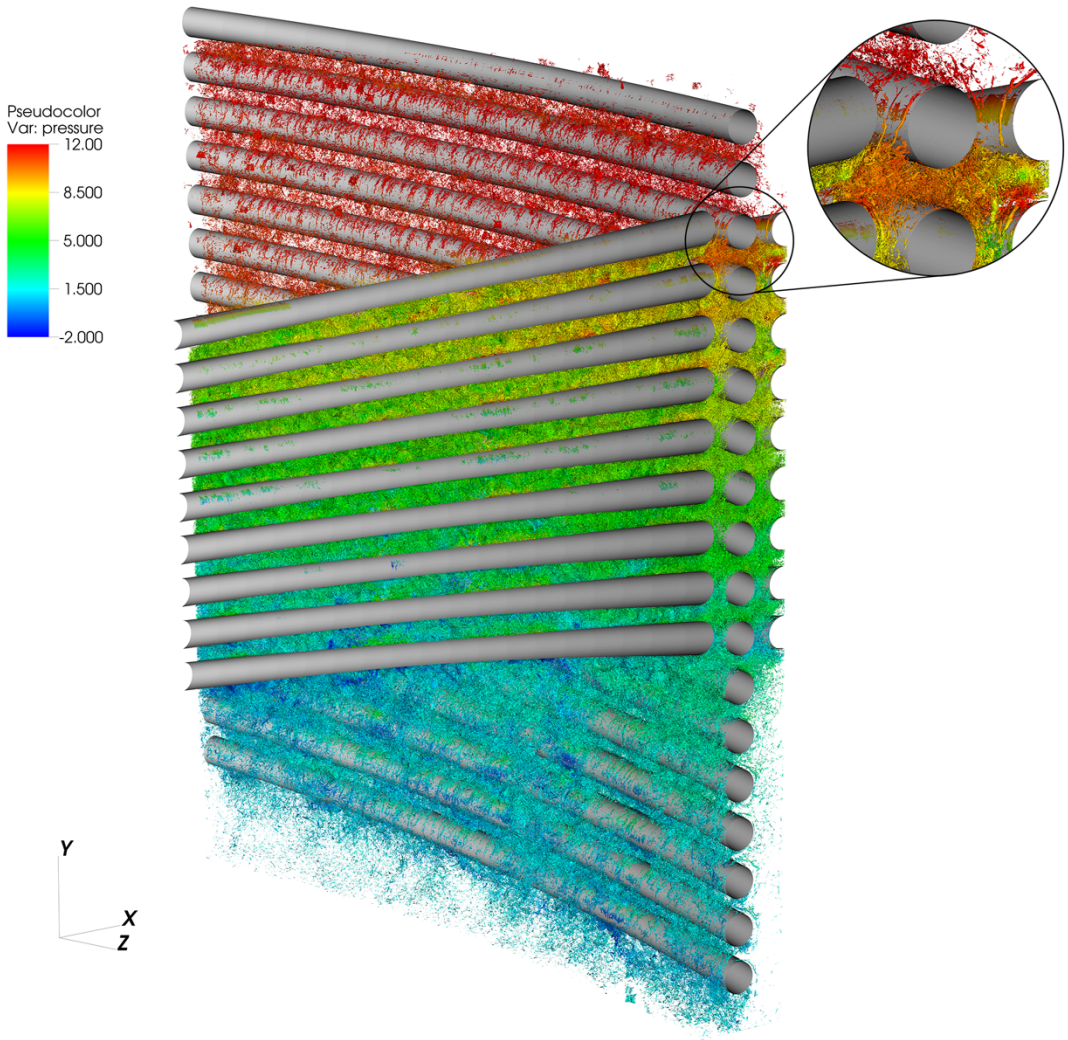

Figure 50: Instantaneous isosurfaces of Lambda-2 criterion

Vortex structures were analyzed with the λ_2 criterion proposed by Jeong and Hussain [50]. The vortex core in the λ_2 criterion is defined by the negative eigenvalue of $S_{ik}S_{kj} + \Omega_{ik}\Omega_{kj}$, where S_{ij} and Ω_{ij} are symmetric and antisymmetric parts of the velocity gradient tensor, respectively. Figure 26 shows the coherent structures identified with the

λ_2 criterion, and normalized pressure was visualized on these isosurfaces. Quasi-streamwise vortices can be observed throughout the channel.

It has been suggested that the development of the quasi-streamwise vortices start with a spanwise stretched flow structure [51], which can be seen at the wall of the tubes in the magnified image. The middle of the stretched flow structure extends with the effect of the mean flow in the channel. Two sides of the original spanwise structure extend in the streamwise direction, forming quasi-streamwise vortices. Quasi-streamwise vortices are more apparent at the beginning of the channel where big flow structures initially form. This region was magnified in the figure for better visualization of the vortices. Farther downstream, in the middle section of the channel, identifying vortex structures becomes harder.

5. CONCLUSIONS

Large eddy simulation on modern high-performance computers provides high-fidelity information about the turbulence dynamics of flow in complex geometries such as that examined in this study. Specifically, using the spectral element method code Nek5000, we analyzed a five-tube helical coil steam generator geometry with slanted adjacent tubes in opposite directions. The pressure drop and turbulence scales were analyzed to show the validity of the mesh for capturing the physics. The pressure drop showed good agreement with experimental measurements as the polynomial order in simulation increased, which indicated that more physics of the flow was captured with the increasing polynomial order. The average mesh size was less than Taylor's microscales, thus confirming that the developed mesh is suitable for the current study.

Results of first- and second-order statistics from LES were compared with available experimental data. The average streamwise velocity showed excellent agreement with experimental data. Normal stresses in the streamwise directions also showed good agreement with experimental data. Overall, first- and second-order statistics from LES showed good agreement with experimental data. In the present study, secondary flow was analyzed, and it was quantified across HCSG. Results showed that complex structure of the examined geometry creates non-negligible secondary flow intensity. Autocorrelation and two-point correlation analysis was carried out along the channel between the tubes in the streamwise direction and along the tubes in the azimuthal. The results showed the integral time and length scales of the largest turbulent structures. Spectral analysis was carried out along the channel between the tubes in order to enable study of the flow

excitation mechanism due to vortex shedding. The power spectrum density from LES was compared with the PIV data. The vortex shedding frequencies along with corresponding Strouhal numbers from LES showed excellent agreement with the frequencies and Strouhal numbers obtained from the experimental data. Spectral analysis was expanded with wavelet analysis for time-frequency information for the fluctuating component of the velocity signals. Wavelet spectrograms showed good correlation with dominant frequencies obtained from power spectra of the signals and revealed a range of frequencies for different-sized flow structures. Moreover, flow was analyzed with POD, and results were compared with the PIV data. Similar flow structures were observed in the most energetic POD modes. Overall, LES showed good agreement with the experimental data and helped further our understanding of the flow behavior in novel steam generators.

REFERENCES

[1] Kakaç, S., Liu, H., and Pramuanjaroenkij, A., 2012, *Heat Exchangers: Selection, Rating, and Thermal Design*, CRC press.

[2] Weaver, D. S., and Fitzpatrick, J. A., 1988, "A Review of Cross-Flow Induced Vibrations in Heat Exchanger Tube Arrays," J. Fluids Struct., **2**(1), pp. 73–93.

[3] Prabhanjan, D. G., Raghavan, G. S. V, and Rennie, T. J., 2002, "Comparison of Heat Transfer Rates between a Straight Tube Heat Exchanger and a Helically Coiled Heat Exchanger," Int. Commun. Heat Mass Transf., **29**(2), pp. 185–191.

[4] Gilli, P. V, 1965, "Heat Transfer and Pressure Drop for Cross Flow through Banks of Multistart Helical Tubes with Uniform Inclinations and Uniform Longitudinal Pitches," Nucl. Sci. Eng., **22**, pp. 298–314.

[5] Reyes, J. N., Groome, J., Woods, B. G., Young, E., Abel, K., Yao, Y., and Yoo, Y. J., 2007, "Testing of the Multi-Application Small Light Water Reactor (MASLWR) Passive Safety Systems," Nucl. Eng. Des., **237**(18), pp. 1999–2005.

[6] Wu, Z., Lin, D., and Zhong, D., 2002, "The Design Features of the HTR-10," Nucl. Eng. Des., **218**(1–3), pp. 25–32.

[7] Ahlfeld, C., Burke, T., Ellis, T., Hejzlar, P., Weaver, K., Whitmer, C., Gilleland, J., Cohen, M., Johnson, B., Mazurkiewicz, S., Mcwhirter, J., Odedra, A., Touran, N., Davidson, C., Walter, J., Zimmerman, G., Weaver, T., Schloss, P., Schweiger, P., and Russick, R., 2011, "Conceptual Design of a 500 MWe Traveling Wave Demonstration Reactor Plant," Proc. ICAPP 2011, pp. 816–823.

[8] Païdoussis, M. P., 1983, "A Review of Flow-Induced Vibrations in Reactors and Reactor Components," Nucl. Eng. Des., **74**(1), pp. 31–60.

[9] Moretti, P. M., "Flow-Induced Vibrations in Arrays of Cylinders," Annu. Rev. Fluid Mech., (1993), pp. 99–114.

[10] Polak, D. R., and Weaver, D. S., 1995, "Vortex Shedding in Normal Triangular Tube Arrays," J. Fluids Struct., **9**, pp. 1–17.

[11] Konstantinidis, E., Balabani, S., and Yianneskis, M., 2002, "A Study of Vortex Shedding in a Staggered Tube Array for Steady and Pulsating Cross-Flow," J. Fluids Eng., **124**(3), pp. 737–746.

[12] Delgado, M., Lee, S., Hassan, Y. A., and Anand, N. K., 2018, "Flow Visualization Study at the Interface of Alternating Pitch Tube Bundles in a Model Helical Coil Steam Generator Using Particle Image Velocimetry," Int. J. Heat Mass Transf., **122**, pp. 614–628.

[13] Li, X., Wu, X., and He, S., 2014, "Numerical Investigation of the Turbulent Cross Flow and Heat Transfer in a Wall Bounded Tube Bundle," Int. J. Therm. Sci., **75**, pp. 127–139.

[14] Wang, Y., Gu, X., Jin, Z., and Wang, K., 2016, "Characteristics of Heat Transfer for Tube Banks in Crossflow and Its Relation with That in Shell-and-Tube Heat Exchangers," Int. J. Heat Mass Transf., **93**, pp. 584–594.

[15] Joh, S., 2011, "Thermal Hydraulic Studies on Helical Coil Steam Generator by CFD," *Proceedings of ASME 2011 Pressure Vessels & Piping Division Conference*, Baltimore, Maryland.

[16] Hassan, Y. A., and Barsamian, H. R., 2004, “Tube Bundle Flows with the Large Eddy Simulation Technique in Curvilinear Coordinates,” Int. J. Heat Mass Transf., **47**(14–16), pp. 3057–3071.

[17] Liang, C., and Papadakis, G., 2007, “Large Eddy Simulation of Cross-Flow through a Staggered Tube Bundle at Subcritical Reynolds Number,” J. Fluids Struct., **23**(8), pp. 1215–1230.

[18] Yuan, H., Solberg, J., Merzari, E., Kraus, A., and Grindeanu, I., 2017, “Flow-Induced Vibration Analysis of a Helical Coil Steam Generator Experiment Using Large Eddy Simulation,” Nucl. Eng. Des., **322**(August), pp. 547–562.

[19] Lai, J. K., Merzari, E., and Hassan, Y. A., 2018, “Large Eddy Simulation of the Flow Behavior in a Simplified Helical Coil Steam Generator,” J. Fluids Eng., **141**(2), p. 021401.

[20] Yildiz, M. A., Yuan, H., Merzari, E., and Hassan, Y. A., 2019, “Numerical Simulation of Isothermal Flow Across Slant Five-Tube Bundle with Spectral Element Method Code Nek5000,” Nucl. Technol., pp. 1–11.

[21] Stephen B. Pope, 2000, *Turbulent Flows*, Cambridge University Press.

[22] Versteeg, H. K., and Malalasekera, W., 2007, *An Introduction to Computational Fluid Dynamics*.

[23] Yildiz, M. A., Merzari, E., and Hassan, Y. A., 2019, “Spectral and Modal Analysis of the Flow in a Helical Coil Steam Generator Experiment with Large Eddy Simulation,” Int. J. Heat Fluid Flow, **80**.

[24] Delgado, M., Hassan, Y. A., and Anand, N. K., 2019, “Experimental Flow

Visualization Study Using Particle Image Velocimetry in a Helical Coil Steam Generator with Changing Lateral Pitch Geometry," Int. J. Heat Mass Transf., **133**, pp. 756–768.

[25] "Nek5000 Version 17.0. Argonne National Laboratory, Illinois" [Online]. Available: http://nek5000.mcs.anl.gov.

[26] Offermans, N., Marin, O., Schanen, M., Gong, J., Fischer, P., Schlatter, P., Obabko, A., Peplinksi, A., Hutchinson, M., and Merzari, E., 2016, "On the Strong Scaling of the Spectral Element Solver Nek5000 on Petascale Systems," *EASC '16 Proceedings of the Exascale Applications and Software Conference*.

[27] Deville, M. O., Fischer, P. F., Mund, E. H., and Gartling, D., 2002, *High-Order Methods for Incompressible Fluid Flow*, Cambridge University Press.

[28] Yuan, H., Yildiz, M. A., Merzari, E., Yu, Y., Obabko, A., Botha, G., Busco, G., Hassan, Y. A., and Nguyen, D. T., 2020, "Spectral Element Applications in Complex Nuclear Reactor Geometries : Tet-to- Hex Meshing," Nucl. Eng. Des., **357**, p. 110422.

[29] Eggels, J. G. M., Unger, F., Weiss, M. H., Westerweel, J., Adrian, R. J., Friedrich, R., and Nieuwstadt, T. M., 1994, "Fully Developed Turbulent Pipe Flow: A Comparison between Direct Numerical Simulation and Experiment," J. Fluid Mech., **268**, pp. 175–210.

[30] Yildiz, M. A., Merzari, E., and Hassan, Y. A., 2018, "Large Eddy Simulation of 5-Tube Bundle Helical Coil Steam Generator Test Section," *International Conference on Nuclear Engineering, Proceedings, ICONE*.

[31] Taylor, G. I., 1938, “The Spectrum of Turbulence.”

[32] Kolmogorov, A. N., 1991, “The Local Structure of Turbulence in Incompressible Viscous Fluid for Very Large Reynolds Numbers,” Dokl. Akad. Nauk SSSR Transl. Proc. R. Soc. A Math. Phys. Eng. Sci., **434**(1890), pp. 9–13.

[33] Lee, S., Delgado, M., Lee, S. J., and Hassan, Y. A., 2018, “Experimental Investigation of the Isothermal Flow Field across Slant 5-Tube Bundles in Helically Coiled Steam Generator Geometry Using PIV,” Nucl. Eng. Des., **338**(August), pp. 261–268.

[34] Blevins, R. D., 1977, *Flow-Induced Vibrations*, Litton Educational Publishing, Inc.

[35] Welch, P. D., 1967, “The Use of Fast Fourier Transform for the Estimation of Power Spectra: A Method Based on Time Averaging over Short, Modified Periodograms,” IEEE Trans. Audio Electroacoust., **15**(2), pp. 70–73.

[36] Hetz, A. A., Dhaubhadel, M. N., and Telionis, D. P., 1991, “Vortex Shedding Over Five In-Line Cylinders,” J. Fluids Struct., **5**, pp. 243–257.

[37] Hoyt, J. W., and Sellin, R. H. J., 1997, “Flow Over Tube Banks—A Visualization Study,” J. Fluids Eng., **119**(2), pp. 480–483.

[38] Lau, K.-M., and Weng, H., 2002, “Climate Signal Detection Using Wavelet Transform: How to Make a Time Series Sing,” Bull. Am. Meteorol. Soc., **76**(12), pp. 2391–2402.

[39] Farge, M., 1992, “Wavelet Transforms and Their Applications to Turbulence,” Annu. Rev. Fluid Mech., **24**, pp. 395–457.

[40] Misiti, M., Misiti, Y., Oppenheim, G., and Poggi, J.-M., 2018, “Wavelet Toolbox ™ User ’ s Guide,” p. 700.

[41] Su, B., Yin, Y., Li, S., Guo, Z., Wang, Q., and Lin, M., 2018, “Wavelet Analysis on the Turbulent Flow Structure of a T-Junction,” Int. J. Heat Fluid Flow, **73**(September 2017), pp. 124–142.

[42] Sirovich, L., 1987, “Turbulence and the Dynamics of Coherent Structures Part I: Coherent Structures,” Q. Appl. Math., **45**(3), pp. 561–571.

[43] Berkooz, G., Holmes, P., and Lumley, J. L., 1993, “The Proper Orthogonal Decomposition in the Analysis of Turbulent Flows,” Annu. Rev. Fluid Mech., **25**(1), pp. 539–575.

[44] Meyer, K. E., Pedersen, J. M., and Özcan, O., 2007, “A Turbulent Jet in Crossflow Analysed with Proper Orthogonal Decomposition,” J. Fluid Mech., **583**, pp. 199–227.

[45] Muld, T. W., Efraimsson, G., and Henningson, D. S., 2012, “Flow Structures around a High-Speed Train Extracted Using Proper Orthogonal Decomposition and Dynamic Mode Decomposition,” Comput. Fluids, **57**, pp. 87–97.

[46] Schmid, P. J., 2010, “Dynamic Mode Decomposition of Numerical and Experimental Data,” J. Fluid Mech., **656**, pp. 5–28.

[47] Brunton, S. L., and Kutz, J. N., 2019, *Data-Driven Science and Engineering*, Cambridge University Press, Cambridge, United Kingdom.

[48] Tu, J. H., Rowley, C. W., Luchtenburg, D. M., Brunton, S. L., and Kutz, J. N., 2014, “On Dynamic Mode Decomposition: Theory and Applications,” J. Comput.

Dyn., **1**(2), pp. 391–421.

[49] Kutz, J. N., Brunton, S. L., Brunton, B. W., and Proctor, J. L., 2016, *Dynamic Mode Decomposition*, Society of Industrial and Applied Mathematics, Philadelphia.

[50] Jeong, J., and Hussain, F., 1995, "On the Identification of a Vortex," J. Fluid Mech., **285**, pp. 69–94.

[51] Zhang, N., Lu, L.-P., Duan, Z.-Z., and Yuan, X.-J., 2008, "Numerical Simulation of Quasi-Streamwise Hairpin-like Vortex Generation in Turbulent Boundary Layer," Appl. Math. Mech. (English Ed., **29**(1), pp. 15–22.